Efficient Analysis for Nonlinear Effects and Power Handling Capability in High Power HTSC Thin Film Microwave Circuits

by

Hongzhen Tang

A thesis
presented to the University of Waterloo
in fulfilment of the
thesis requirement for the degree of
Doctor of Philosophy
in
Electrical Engineering

Waterloo, Ontario, Canada, 2000

I hereby declare that I am the sole author of this thesis.

I authorize the University of Waterloo to lend this thesis to other institutions or individuals for the purpose of scholarly research.

I further authorize the University of Waterloo to reproduce this thesis by photocopying or by other means, in total or in part, at the request of other institutions or individuals for the purpose of scholarly research.

The University of Waterloo requires the signatures of all persons using or photocopying this thesis. Please sign below, and give address and date.

Abstract

In this study two nonlinear analysis methods are proposed for investigation of nonlinear effects of high temperature superconductive(HTSC) thin film planar microwave circuits. The MoM-HB combination method is based on the combination formulation of the moment method(MoM) and the harmonic balance(HB) technique. It consists of linear and nonlinear solvers. The power series method treats the voltages at higher order frequencies as the excitations at the corresponding frequencies, and the higher order current distributions are then obtained by using the moment method again. The power series method is simple and fast for finding the output power at higher order frequencies. The MoM-HB combination method is suitable for strong nonlinearity, and it can be also used to find the fundamental current redistribution, conductor loss, and the scattering parameters variation at the fundamental frequency. These two proposed methods are efficient, accurate, and suitable for distributed-type HTSC nonlinearity. They can be easily incorporated into commercial EM CAD softwares to expand their capabilities.

These two nonlinear analysis method are validated by analyzing a HTSC stripline filter and HTSC antenna dipole circuits. HTSC microstrip lines are then investigated for the nonlinear effects of HTSC material on the current density distribution over the cross section and the conductor loss as a function of the applied power. The HTSC microstrip patch filters are then studied to show that the HTSC interconnecting line could dominate the behaviors of the circuits at high power. The variation of the transmission and reflection coefficients with the applied power and the third output power are calculated.

The HTSC microstrip line structure with gilded edges is proposed for improving the power handling capability of HTSC thin film circuit based on a specified limit of harmonic generation and conductor loss. A general analysis approach suitable for any thickness of gilding layer is developed by integrating the multi-port network theory into aforementioned proposed nonlinear analysis methods. The conductor loss and harmonic generation of the gilded HTSC microstrip line are investigated.

Acknowledgements

I would like to thank my supervisor Professor Chow for his guidance and financial support. I am grateful to my co-supervisor Professor Safavi-Naeini for his guidance.

I am deeply indebted to Professors Chaudhuri, Lit, MacPhie, and Mansour, and external examiner Professor El-Ghazaly for their review and advice on this thesis.

Help from Drs. Torabian-Esfahani and Hodjat is also gratefully acknowledged for providing the code for complex image Green's function.

Finally, I especially want to thank my husband for his love, patience, and understanding, which give me confidence and strength to tide over the hard time that I met. It was one of the happiest time in my life to study with him in the same department. Thanks are extended to my parents, brothers, and sister for their continual support and encouragement.

Contents

List of Figures

List of Tables

Chapter 1

Introduction

1.1 Motivations

Since the discovery of superconductivity, extensive efforts have been made to search for application of superconductivity where substantial benefits can be obtained. However, the application of low temperature superconductors (LTSC) is limited, because superconductivity could be utilized only at near-absolute-zero temperature achieved by the use of expensive and hard to handle liquid helium (4.2 K). Hence the cooling expenses outweigh the benefits which might be obtained in most applications. With high temperature superconductors(HTSC) found in 1986, superconductivity can be realized at temperature of up to around 90 K and higher. These temperatures are easily provided by the use of liquid nitrogen (77 K), thus the application of superconductivity become more feasible. HTSC materials are complex oxides. Examples of HTSC materials include ceramic $YBa_2Cu_3O_7$, $Tl_2Ba_2CaCu_2O_8$, $Tl_{0.5}Pb_{0.5}Ca_2Sr_2Cu_3O_9$, and $HgBa_2Ca_2Cu_3O_8$. For most microwave applications, the HTSC materials must be prepared as epitaxial thin films on lattice matched

substrates, such as Lanthanum Aluminate(LaAlO$_3$) [1].

HTSC materials exhibit many unique properties that make them attractive for a wide range of microwave applications. Due to the extremely low surface resistance of superconductors at microwave frequencies [2], the immediate microwave application of superconductivity is passive components, such as resonators, filters, multiplexers, circulators, power splitters and combinators, delay lines and switches. For example, the thin film HTSC materials have 10 to 1000 times lower surface resistance than copper at microwave frequencies[1]. As a result, HTSC passive microwave components, such as resonators [3] and filters [5], have very low loss and high Q value. Great improvement has been found for these passive microwave components as compared to their normal conductor counterparts. In addition, due to the nonlinear superconducting quantum tunneling effects, now known as the Josephson effects, superconductivity application in HTSC active microwave circuits such as detectors, mixers, parametric amplifiers, and oscillators were developed [1]. The improvement in device performance is so pronounced that many superconductive microwave devices would not function if they were made using normal conductors.

HTSC microstrip transmission lines combine the advantages of waveguides and normal metallic microstrip transmission lines. Waveguides have low loss but bulky volume, and normal metallic microstrip transmission lines have small volume but high loss. With HTSC microstrip lines used, both low loss and small volume can be achieved. Also, compared with machining waveguides, it is easy and inexpensive to print HTSC microstrip lines on substrate. The low loss and compact volume of microwave circuits made of HTSC materials are especially attractive for satellite communications [6] [7].

So far most applications of HTSC microwave circuits, however, are limited in low power level and normally used only in the receiving mode. In the transmitting

mode under moderately high power, say 10 Watts, the surface resistance increases moderately, but becomes *nonlinear*. A further increase in power results in significant increase of the surface resistance. Consequently, the circuits become very lossy and are even worse than those constructed from conventional conductors. Once the current density exceeds the HTSC material critical current density, the superconductivity disappears and the circuits collapse.

In a design of transmitter with superconductive circuit, it would be desirable to push the power level as high as possible before the nonlinear effects become intolerable. The limit on the allowable harmonic level generated may be quite low (say, -70 to -100 dB) so as not to interfere with the sensitive receiver in an integrated duplex package, say, in a satellite [8].

Therefore, it is important to understand, and ultimately to control, the nonlinear effects of superconductive microwave circuits, such as harmonic generation and intermodulation distortion, in designing with superconductor materials. These nonlinear effects are resulted from the nonlinear surface impedance of HTSC materials in various HTSC microstrip and patch circuits. With the nonlinear effects understood, one should be able to adjust the circuit layout to increase the power handling capability of HTSC microwave circuits.

1.2 Objectives

One purpose of this study is to investigate the nonlinear effects of HTSC thin film microwave circuits in high power. In order to do that a method must be proposed for the efficient analysis of the nonlinearity of HTSC material. The proposed method should take into consideration the essential features of the superconductor

nonlinearity, and in the meantime, is still suitable for analysis of distributed element microwave circuits. It is hoped that its application to any particular case is mainly a matter of choosing a high power design and evaluating the appropriate expressions analytically or by numerical calculation.

The other purpose is to improve the power handling capability of HTSC microwave circuits from the point of view of circuit design, that is, to reduce the nonlinear effects by selecting different circuit designs. To this end, we must propose new circuit design and analyze the behaviors of the designed circuit.

1.3 Organization of this thesis

The organization of this thesis is as follows:

Chapter 2 first describes the HTSC phenomenological electromagnetic theory based on two-fluid model and London's equations. The penetration depth and complex conductivity of HTSC material are introduced. The surface impedance of HTSC material at low power is derived. The published measurements of the surface impedance of HTSC material at moderate and high powers are presented. Then, the sources of HTSC nonlinearity are discussed. Next, nonlinear effects and the time-domain and frequency-domain methods used for nonlinear analysis are reviewed, and their suitability and limitations are discussed. Finally, the proposed nonlinear analysis methods are briefly introduced. One of them is called the MoM-HB combination method, which will be explained in detail in Chapters 3 and 4. This method consists of linear and nonlinear solvers. The other method is called the power series method, which will be explained in detail in Chapter 5.

Chapter 3 focuses on the linear solver in the MoM-HB combination method. The

linear analysis is carried out in the frequency-domain. According to the boundary condition equation on the conducting surface, a mixed potential integral equation could be obtained. The application of the moment method to it results in a form of matrix equation. By adopting the complex image Green's function, the linear term, which is related to the field outside the conducting material, takes into consideration the field interactions and mutual coupling in the linear region outside HTSC material.

Chapter 4 focuses on the nonlinear solver in the MoM-HB combination method. The nonlinear analysis is performed by using the harmonic balance technique. The $v - i$ characteristic in the time domain is Fourier-transformed into the frequency-domain to fit into the so-called harmonic balance equation. Then an iterative procedure is employed to solve the equation for the current distribution, in which the initial guess and the number of harmonics to be considered are discussed. At last, the MoM-HB combination method is applied to a HTSC stripline filter circuit for the investigation of two-tone intermodulation. The obtained results are compared with the published measurement results to verify this nonlinear analysis method.

Chapter 5 elaborates the power series method by formulating a general microstrip circuit. This method is a simple and fast nonlinear analysis approach for the output power at higher harmonics. Then both proposed nonlinear analysis methods are applied to analyze HTSC strip antenna dipole circuits. A thorough comparison is made to the results obtained by both methods and for typical HTSC material, weakly and strongly nonlinear materials. Based on the obtained results and discussions, the type of HTSC nonlinearity is identified. The range of validity and advantage of the two nonlinear analysis methods are also discussed.

Chapter 6 investigates HTSC microstrip lines for the effects of nonlinearity of

HTSC material on the current density distribution over the cross section of the stripline and the conductor loss of HTSC material as a function of the applied power. The effective surface impedances are derived to account for the influence of the configuration of microstrip line structure. The thickness of the HTSC conductor is also taken into consideration. Besides, much finer grids are put over the regions near the edges to emphasize the rapid variation in the current densities near the edges. The current distribution obtained are compared with the published numerical results at high applied power. The HTSC conductor loss is contrasted to those obtained from linear model and of gold microstrip line.

Chapter 7 studies HTSC microstrip patch filters for the microstrip interconnecting lines constructed from HTSC and linear gold materials. The HTSC microstrip line could dominate the behaviors of the circuit, especially at high power. A single-mode square patch filter and a dual-mode corner-cut patch filter are simulated. The scattering parameters in the case of HTSC interconnecting lines and gold interconnecting lines at different input power levels are obtained. Thus, the change of Q value is discussed. The output power at the third harmonic frequency as a function of the applied power are also found.

Chapter 8 deals with the issue of improving power handling capability of the HTSC thin film circuits. For this purpose, the HTSC microstrip line structures with gilded edges are proposed. The idea is to cause the very high current densities near the edges to flow through the gold conductor instead of the HTSC at high input power. Although at low input power the very low loss advantage of the HTSC will be lost, the loss will be still much lower than that of a pure gold strip. A general analysis approach, which should be suited for any thickness of gilding layer, is developed by integrating the multi-port network theory into aforementioned two proposed nonlinear analysis methods. The output power at the third harmonic

frequency and the conductor loss of gilded HTSC microstrip line are evaluated for different thickness of the gilding layer. The conductor loss is also contrasted to the results of pure HTSC strip and pure gold strip.

Chapter 9 give a summary of the thesis. The most important topics that have been presented in this thesis are reviewed. How the objectives of the research have been achieved is explained. It also lists the contributions of this present study. Finally, the thesis is concluded by providing recommendations for future research.

Chapter 2

HTSC EM theory and nonlinearity

2.1   Introduction

In this chapter theoretical background of HTSC material related to this study and nonlinear analysis is reviewed. Since it is not necessary for this study to go deeply into the details of superconductor microscopic electromagnetic theory, the simple HTSC phenomenological theory based on the two-fluid model and the London's equations is introduced here. The theory is workable and satisfactory for microwave behaviors of superconductor at low applied power level [1].

In Section 2.2 the two-fluid model is described and London's equations are introduced. The penetration depth and complex conductivity of superconductor are then introduced. In Section 2.3 the surface impedances for normal conductors and superconductors at low power level are derived. For the surface impedance of HTSC materials at high power level, the measured results from the literature

are presented. In Section 2.4 the sources of HTSC nonlinearity are discussed. In Section 2.5 general nonlinear effects are described. In Section 2.6 we review available nonlinear analysis methods in the time-domain and frequency-domain, and address their suitability and limitations. In Section 2.7 the nonlinear modeling approaches that will be proposed in this study, i.e., the MoM-HB combination method and the power series, are briefly introduced. Finally, Section 2.8 concludes this chapter.

2.2 HTSC phenomenological electromagnetic theory

The magnetic inductance becomes zero inside a superconductor when it is cooled below T_c in a weak external magnetic field, that is, the magnetic flux is expelled from the interior of the superconductor. This is called the *Meissner effect*, discovered in 1933, one of the distinctive properties of superconductor [12]. The Meissner effect could not be explained by any conventional model of electricity in solid. In 1934, Brothers F. and H. London proposed a simple two-fluid model in order to explain the Meissner effect [9]. The London's model also predicted the penetration depth [10].

2.2.1 Two-fluid model

The two-fluid model is used to modify the conventional Ohm's law. Of the total density n of electrons, there is a fraction n_s that behaves in an abnormal way and represents superconducting electrons. These are not scattered by either impurities or phonons, thus they do not contribute to the resistivity. They are freely accelerated by an electric field. Therefore, the total electric current in a superconductor

material can be regarded as the superposition of two currents, the *superconducting* electric current, constructing from Cooper or electron pairs, and the *normal* electric current. That is,

$$\mathbf{J} = \mathbf{J}_n + \mathbf{J}_s \qquad (2.1)$$

The normal current density can be expressed, from conventional Ohm's law, as:

$$\mathbf{J}_n = \sigma_n \mathbf{E} \qquad (2.2)$$

where σ_n is the conductivity contributed by the normal carriers. The superconducting current density is given by:

$$\mathbf{J}_s = n_s q_s \mathbf{v}_s \qquad (2.3)$$

where n_s, q_s, and $\mathbf{v}_s$ are the density, electrical charge, and velocity of superconducting electrons, respectively.

At temperature below the critical temperature T_c, the equilibrium fractions of normal and superconducting electrons, n_n/n and n_s/n, vary with absolute temperature T as

$$\frac{n_n}{n} = \left(\frac{T}{T_c}\right)^4, \qquad \frac{n_s}{n} = 1 - \left(\frac{T}{T_c}\right)^4 \qquad (2.4)$$

At $T = 0$, all of the carriers are superconducting, and the fraction of superconducting carriers approaches zero as the temperature approaches T_c.

2.2.2 London's equations

The London's equations describe the relation between the superconductor current density and the electromagnetic fields. The equation of motion of the superconducting electrons can be written as:

$$m_s \frac{d\mathbf{v}_s}{dt} = q_s \mathbf{E} \qquad (2.5)$$

where m_s is the effective mass of superconducting electrons and $\mathbf{E}$ is the electrical field strength. Substituting (2.3) into (2.5) yields

$$\frac{d\mathbf{J}_s}{dt} = \frac{n_s q_s^2}{m_s}\mathbf{E} \tag{2.6}$$

This is known as the *first London equation*, which describes the relation between the superconductor current density and the electric fields.

By taking the curl of (2.6) and applying Faraday's law: $\nabla \times \mathbf{E} = -\frac{\partial \mathbf{B}}{\partial t}$, we obtain

$$\frac{\partial}{\partial t}\left(\nabla \times \mathbf{J}_s + \frac{n_s q_s^2}{m_s}\mathbf{B}\right) = 0 \tag{2.7}$$

London brothers noticed that with Ohm's law and an infinite conductivity, (2.7) leads to

$$\frac{\partial \mathbf{B}}{\partial t} = 0 \tag{2.8}$$

An infinity conductivity only implies that the magnetic field cannot change, which is contrary to the experimental evidence. Thus they integrated equation (2.7) and took the following particular solution:

$$\nabla \times \mathbf{J}_s + \frac{n_s q_s^2}{m_s}\mathbf{B} = 0 \tag{2.9}$$

This is the *second London equation*, which describes the electrodynamics of a superconductor.

In order to show how (2.9) leads to the Meissner effect, we use the Maxwell equation: $\frac{1}{\mu}\nabla \times \mathbf{B} = \frac{\partial \mathbf{D}}{\partial t} + \mathbf{J}_s$, where μ is the permeability. Inside a superconductor, the conductive current, $\mathbf{J}_s$ dominates, and at low and moderate frequencies, we can neglect the term $\frac{\partial \mathbf{D}}{\partial t}$, which represents the displacement current, so we obtain

$$\mathbf{J}_s = \frac{1}{\mu}\nabla \times \mathbf{B} \tag{2.10}$$

By applying the curl-operator to both sides of (2.10) and combining it with (2.9), we have

$$\frac{1}{\mu}\nabla \times \nabla \times \mathbf{B} + \frac{n_s q_s^2}{m_s}\mathbf{B} = 0 \tag{2.11}$$

By virtue of a vector identity: $\nabla \times \nabla \times \mathbf{B} = \nabla(\nabla \cdot \mathbf{B}) - \nabla^2\mathbf{B}$, and the Maxwell equation $\nabla \cdot \mathbf{B} = 0$, then (2.11) reduces to

$$\nabla^2\mathbf{B} = \frac{\mu n_s q_s^2}{m_s}\mathbf{B} \tag{2.12}$$

This equation enables one to calculate the local field inside the superconductor and it is another expression of the London equation.

In one dimensional case, (2.12) can be written as

$$\frac{d^2 B}{dx^2} = \frac{B}{\lambda_L^2} \tag{2.13}$$

where we define

$$\lambda_L = \sqrt{\frac{m_s}{\mu n_s q_s^2}} \tag{2.14}$$

Thus, the field inside the superconductor is given by the solution of the equation (2.13):

$$B(x) = B_0 \exp(-x/\lambda_L) \tag{2.15}$$

From (2.15), it is seen that the magnetic field decays exponentially inside the superconductor from the surface with a decay length equal to the λ_L. That is, the magnetic field is excluded inside the superconductor. (2.15) shows that, in order to have zero field within the bulk of the material, one must have a sheet of superconducting current, which flows within λ_L from the surface and which creates an opposite field inside the superconductor that cancels the externally applied magnetic field. Therefore (2.15) explains the Meissner effect well.

London theory is valid only for superconductor in weak magnetic field. It regards the superconducting material as being entirely superconducting or entirely normal.

The variation of n_s with temperature and applied magnetic field is not given, that is, it does not link n_s with the applied field or current. So the London equations are not applicable to situations in which the number of superconducting electrons n_s varies.

2.2.3   Penetration depth

The λ_L in (2.14) measures the extension of the penetration of the magnetic field inside the superconductor, so λ_L is called the *penetration depth* inside the super-conducting material. The penetration depth λ_L is also a function of temperature. Substituting (2.4) into (2.14) yields $\lambda_L(T)$ at temperature T as follows:

$$\lambda_L(T) = \frac{\lambda_L(0)}{\sqrt{1 - (T/T_c)^4}} \tag{2.16}$$

where $\lambda_L(0)$, the penetration depth at $T = 0K$, is defined by

$$\lambda_L(0) = \sqrt{\frac{m_s}{\mu n q_s^2}} \tag{2.17}$$

The penetration depth has a minimum value of $\lambda_L(0)$ and diverges as temperature approaches T_c. Compared with the classical skin depth for normal conductor (will be given in next section), $\lambda_L(T)$ has a unique property of being independent of the microwave frequencies.

In terms of the penetration depth $\lambda_L(T)$, the London's equations are expressed as follows [1]:

$$\frac{\partial \mathbf{J}_s}{\partial t} = \frac{1}{\mu_0 [\lambda_L(T)]^2} \mathbf{E} \tag{2.18}$$

$$\nabla \times \mathbf{J}_s = -\frac{1}{[\lambda_L(T)]^2} \mathbf{H} \tag{2.19}$$

2.2.4 Complex conductivity

For a sinusoidal current with angular frequency ω, (2.18) becomes

$$\mathbf{J}_s = \frac{1}{j\omega\mu[\lambda_L(T)]^2}\mathbf{E} = \sigma_{sc}\mathbf{E} \tag{2.20}$$

where

$$\sigma_{sc} = \frac{1}{j\omega\mu[\lambda_L(T)]^2} \tag{2.21}$$

is the conductivity of the superconducting carriers. Note that σ_{sc} is purely imaginary and does not contribute to the loss. Substituting (2.2) and (2.20) into (2.1) yields the relation between current and electric field in superconductor:

$$\mathbf{J} = (\sigma_n + \sigma_{sc})\mathbf{E} = \sigma\mathbf{E} \tag{2.22}$$

where

$$\sigma = \sigma_n + \sigma_{sc} = \sigma_n - j\frac{1}{\omega\mu[\lambda_L(T)]^2} \tag{2.23}$$

From (2.23) it is seen that the conductivity of superconductor is a *complex* number. The real part of σ represents the loss from the normal carriers, whereas its imaginary part represents the kinetic energy of the superconductive carriers.

2.3 Surface impedances

2.3.1 Surface impedance for normal conductors

The surface impedance is defined as the characteristic impedance seen by a plane wave incident perpendicularly upon a flat surface of the conductor. For low resistivity normal conductors, such as silver, copper, or gold with conductivity of σ, the

surface impedance can be derived from Maxwell's equation and is given by:

$$Z_s = R_s + jX_s = \sqrt{\frac{j\omega\mu}{\sigma}} = (1+j)\sqrt{\frac{\omega\mu}{2\sigma}} \qquad (2.24)$$

For normal conductors, σ is a real number, and according to (2.24), the surface resistance, R_s, and the surface reactance, X_s, are equal:

$$R_s = X_s = \sqrt{\frac{\omega\mu}{2\sigma}} = \frac{1}{\delta\sigma} \qquad (2.25)$$

where

$$\delta = \sqrt{\frac{2}{\omega\mu\sigma}} \qquad (2.26)$$

is the classical *skin depth* of the normal conductor. From (2.25), we can see that both R_s and X_s are proportional to $f^{1/2}$ for normal metal, a result that has been confirmed experimentally.

2.3.2 Low field surface impedance for superconductors

For superconductor we use the complex conductivity presented in (2.23) to obtain expressions for the surface impedance. Substituting (2.23) into (2.24) yields the surface impedance, that is

$$Z_s = R_s + jX_s = \sqrt{\frac{j\omega\mu}{\sigma_n - j\frac{1}{\omega\mu[\lambda_L(T)]^2}}} \qquad (2.27)$$

Then R_s and X_s are obtained as follows:

$$R_s = \frac{1}{2}\omega^2\mu^2[\lambda_L(T)]^3\sigma_N\frac{n_n}{n} \qquad (2.28)$$

$$X_s = \omega\mu\lambda_L(T) \qquad (2.29)$$

where $n = n_n + n_{sc}$, n_n represents the normal carrier density and n_{sc} represents the superconductive carrier density, so n is the total carrier density. Note that in the

normal state $n_n = n$. σ_N is the conductivity for the superconductor in its normal state [1]:

$$\sigma_n = \sigma_N \frac{n_n}{n} = \sigma_N \left(\frac{T}{T_c}\right)^4 \tag{2.30}$$

The two-fluid model leads to the prediction that the surface resistance R_s, the real part of Z_s, is proportional to ω^2 for a superconductor according to (2.28), which is quite different from the $\omega^{1/2}$ frequency dependence for normal metal conductor. The ω^2 frequency dependence is in good agreement with experimentally derived values for HTSC thin films. The surface reactance X_s, the imaginary part of Z_s, is inductive. The equivalent inductance L_K is known as the kinetic inductance: $L_K = \mu\lambda_L(T)$, and it reflects the kinetic energy of the superconductive carriers.

2.3.3   High field surface impedance for superconductors

The surface impedance derived above is valid only at low applied power level. Even at moderate power level, HTSC materials show nonlinear effects. The origin of HTSC nonlinearity is the RF magnetic field or RF current dependence of surface impedance of HTSC materials [14, 15, 17].

Oates et. al. [14] have carried out measurements of the surface impedance of $YBa_2Cu_3O_{7-x}$ thin films using a HTSC stripline resonator as the test sample.

They measured Z_s over a frequency range from 1.5 to 20 GHz and at temperature from 4 to 90 K and for the RF magnetic field from zero to 300 Oe. The reactance X_s can be determined from the measured resonant frequency shift data. The resistance R_s can be calculated according to $R_s = G/Q_C$, where Q_c is the conductor Q value of resonator and G is the geometry factor of the resonator.

Figure 2.1 shows the dependence of R_s on H_{rf} from [14], where H_{rf} is the maximum RF magnetic field generated by the RF current flowing in the HTSC
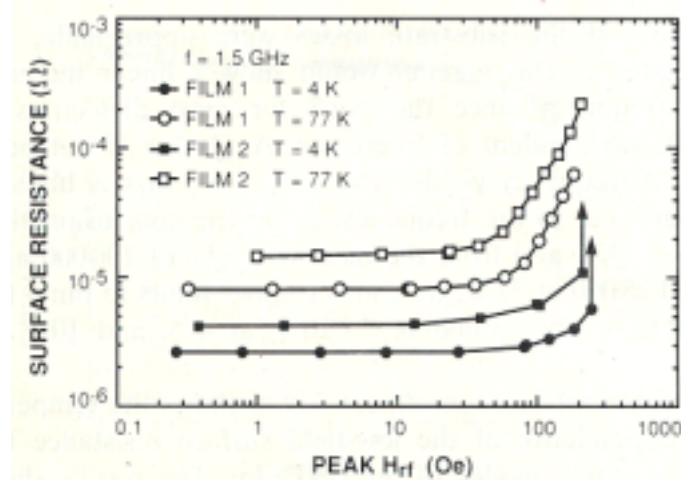
Figure 2.1: Surface resistance R_s versus peak H_{rf}, the peak field at the edges of the center strip, for two HTSC YBa$_2$Cu$_3$O$_{7-x}$ films at 4 K and 77 K. The frequency in all cases is 1.5GHz; Film 1: $T_c = 90$ K, $\lambda(0) = 0.22\mu$m; Film 2: $T_c = 86.4$ K, $\lambda(0) = 0.167\mu$m.

stripline for two YBa$_2$Cu$_3$O$_{7-x}$ thin films. Much higher values of H_{rf} can be reached at a given power level in stripline structures than in the usual cavity geometries, because the narrow transmission line concentrates the current and leads to higher current density and higher H_{rf}.

They have observed that, at 4 K below the apparent critical field and at 77 K over the entire range, the surface resistance R_s is well approximated by a quadratic dependence on H_{rf},

$$R_s = R_{s0} + R_{s2}H_{rf}^2 \tag{2.31}$$

where R_{s0} and R_{s2} are constants. R_{s0} is the surface resistance at very low fields. H_{rf} is equal to the maximum RF surface current density J_s in the HTSC films

when expressed in the same units of A/m. Thus (2.31) can be rewritten as:

$$R_s = R_{s0} + R_{s2}J_s^2 \qquad (2.32)$$

From (2.32) the nonlinear $v - i$ characteristic of HTSC materials can be derived.

2.4 Sources of HTSC nonlinearity

In 1950 Ginzburg and Landau [9] proposed a phenomenological set of equations, allowing for spatial variations in the superelectron density n_s due to the presence of a magnetic field. The construction of GL theory is independent of the microscopic mechanism and is purely based on the ideas of the second order phase transition in thermodynamics only.

Ginzburg and Landau began their argument by introducing a quantity to characterize the degree of superconductivity at various point in the material. The quantity is called the *order parameter* and denoted by $\Psi(\mathbf{r})$. The $\Psi(\mathbf{r})$ represents some effective wave-function of the superconducting electrons such that $|\Psi(\mathbf{r})|^2$ represents the local density of superconducting electrons, $n_s(\mathbf{r})$. The order parameter is defined to be zero for a normal region and unity for a fully superconductor region at zero temperature with zero magnetic field. Physically, Ψ can be considered as the probability amplitude for finding a Cooper pair at a point $\mathbf{r}$.

Based on the Ginzburg-Landau theory, the density of the superconducting carrier, n_s, is magnetic field dependent. Consequently, from (2.14), $\lambda(T)_L$ is also magnetic field dependent, and then from (2.28) and (2.29), R_s and X_s are functions of the magnetic field. The dependence is more pronounced at high values of magnetic fields.

From the physical point of view, there are two sources that contribute to the superconducting nonlinearity.

The first one is the flux line motion in the superconducting material. The flux line motion is a means of dissipating energy within a superconductor. Since the flux lines are lines of magnetic field $\mathbf{H}$, when a current $\mathbf{J}$ flows there is a Lorentz force $\mathbf{J} \times \mathbf{H}$ perpendicular to both and forces the flux lines to move. The flow of current in a superconductor is limited by several factors, such as grain boundaries, defects and impurities in the material.

The second is grain boundaries. From the point of view of quantum mechanics the supercurrent formed by Cooper pairs can tunnel through barrier between two superconductors. This is called Josephson Junction effects. Quantitative accounts of Josephson Junction behavior usually are modeled as resistance-capacitance-shunted-junction(RCSJ). In this model, a capacitor and a resistor are assumed to be in parallel circuit with an ideal Josephson Junction. Using the RCSJ model, the current can be expressed in terms of the phase difference, θ, of the wave functions characterizing the two superconductors across the junction boundary [9]. That is

$$\frac{h}{2\pi e} \left[C \frac{d\theta^2}{dt} + G \frac{d\theta}{dt} \right] + I_c \sin \theta = I(t) \tag{2.33}$$

where C is the capacitance of the junction, $G = 1/R$ is the passive conductivity, and I_c is the critical current of the junction. It is found from (2.33) that the relation between v and i is nonlinear.

In a superconductor each grain boundary is an insulator (between superconducting grains), thus macroscopically a superconductor is an interconnected network of countless Josephson Junctions (JJ). The current can take many different paths through the grain boundaries. Grain boundaries present barrier to the passage of current and behave like the weak links, because the limit on the total current is set

by the resistance across the grain boundary barriers. Even when all the junctions are identical, the dynamics of the equivalent circuit of all the junctions is nonlinear.

Macroscopically, their manifestation is that the surface impedance, Z_s, of the superconducting materials has a nonlinear dependence of the incident RF magnetic field, H_{rf}.

2.5   Nonlinear effects

Nonlinear circuits generate a number of new frequency components. A detailed examination of the generation of new frequencies can be found in [19]. Generation of new frequencies in nonlinear circuits does not tell the whole story of nonlinear effects, especially the effects of nonlinearities in microwave systems. Many types of nonlinear phenomena have been defined.

The first type is harmonic generation, the generation of integer multiples of a single excitation frequency. The second type is intermodulation, the generation of linear combinations of two or more excitation tones. The third type is saturation and desensitization, the distortion of a small signal when a large signal drives an amplifier circuit into saturation. The fourth type is cross-modulation, the transfer of modulation from one signal to another. The fifth type is amplitude/phase modulation conversion, the conversion of amplitude changes into phase changes. Superficially, on the system level, these are often considered to be separate phenomena, but they are simply different manifestations of the same nonlinearity. In this study, *harmonic generation* and *intermodulation distortion* are our major concerns.

In many systems, for example, narrow-band receivers, the generation of harmon-

ics is not a serious problem because the harmonics are far removed in frequency from the signals of interest and inevitably are rejected by filters. On the other hand, for transmitters, harmonics and other spurious outputs may interfere with other communications systems and must be reduced very carefully by filters or by other means.

Intermodulation signals generated in an amplifier or communications receiver often present a very serious problem, because they represent spurious signals that interfere with, and can be mistaken for, the desired signals. Intermodulation signals are generally much weaker than the signals that generate them; however, a situation often arises wherein two or more very strong signals, which may be outside the receiver's passband, generate an intermodulation signal that is within the receiver's passband and obscures a weak, desired signal. Even-order intermodulation signals usually occur at frequencies well above or below the signals that generate them and consequently are often of little concern. The intermodulation signals of greatest concern are usually the third order ones that occur at $2\omega_1 - \omega_2$ and $2\omega_2 - \omega_1$, because they are the strongest of all odd-order products, are close to the signals that generate them, and often cannot be rejected by filters. Intermodulation is a major concern in microwave system.

2.6   Review of methods for nonlinear analysis

In general, the analysis methods for nonlinear microwave circuits fall into two main categories—time-domain techniques and frequency-domain techniques [19].

2.6.1   Time-domain analysis techniques

Time-domain techniques [20] are theoretically valid and are practical for low frequency analog and digital design. It is a straightforward matter to use conventional circuit theories to write time-domain differential equations that describe a nonlinear circuit. The resulting differential equations are nonlinear and can be solved numerically.

Three problems often occur that can make such time-domain techniques impractical. The first is that such elements as dispersive transmission lines and transmission discontinuities are difficult, if not impossible, to analyze in the time domain. The second is that the circuit may have time constants that are large compared to the inverse of the fundamental excitation frequency. This will result in continuing the numerical integration of the equations through many excitation cycles. This long integration costs a large amount of computer time; furthermore, numerical truncation errors in the long integration may become large and reduce the accuracy of the solution. The third problem is that each nonlinear reactive element in the circuit adds a differential equation to the set of equations that describe the circuit. A large circuit can have many reactive elements, so the set of equations that must be solved may be very large.

2.6.2   Frequency-domain analysis techniques

Many frequency-domain techniques for analyzing microwave circuits have become popular in recent years. The two most important are called harmonic balance analysis [11] and Volterra series or nonlinear transfer function analysis [13].

2.6.2.1 Harmonic balance Technique

The harmonic balance analysis is applicable primarily to the nonlinear circuits that are excited by a single large-signal excitation source.

The harmonic balance technique uses multi-port circuit theory to simplify at least part of the circuit by lumping all the linear elements. Thus, the circuit under consideration is regrouped so that the circuit is equivalent to consisting of a linear sub-circuit and a number of nonlinear sub-circuits. The linear sub-circuit can be treated as a multi-port and described by its Y-parameters, S-parameters, or some other multi-port matrix. The nonlinear elements are modeled by their global $v - i$ characteristics. Thus the circuit is reduced to an $(N + 2)$-port network, with nonlinear elements connected to N of the ports and voltage source connected to the other two ports. The voltage and current at each port can be expressed in the time-domain or the frequency-domain. Because of the nonlinear element, however, the port voltage and current must contain frequency components at all harmonics of the excitation.

The idea of harmonic balance is, by applying Kirchhoff's current(voltage) law to each port, to find a set of port voltage(current) waveforms, or alternatively, the harmonic voltage(current) components, that give the same currents(voltages) in both the linear network equations and the nonlinear network equations. After finding the current(voltage) expressions for each linear port and each nonlinear element, one can obtain a harmonic balance equation, or current-error vector, $F(v)$, (voltage-error vector, $F(i)$), which represents the difference between the currents(voltages) calculated from linear and nonlinear subnetworks, at each port and at each harmonic. By using some numerical algorithms, such as optimization methods, splitting method, Newton's method, one can find the solution v (or i). If one wants to

find the parameters in the time-domain, this can be done by means of the Fourier transformation.

2.6.2.2 Volterra series

The Volterra series analysis is applicable to the opposite problem: weakly driven, and thus weakly nonlinear, circuits having multiple small signal excitations at non-commensurate frequencies. As such, it is most useful for evaluating intermodulation characteristics and other nonlinear phenomena in small-signal receiver circuits, such as amplifiers. With some modifications, the Volterra series can also be used to determine the intermodulation properties extended to certain situations involving non-commensurate signals.

In order to use the Volterra series technique to analyze a nonlinear system, we need higher order transfer functions that are able to describe the relation of the input frequencies and the creation of new frequencies. That is:

$$Y(f) = \sum_{n=1}^{\infty} \int_{-\infty}^{\infty} df_1 \int_{-\infty}^{\infty} df_2 \cdots \int_{-\infty}^{\infty} df_n H_n(f_1, f_2, \cdots, f_n) \delta(f - f_1 - f_2 - \cdots - f_n) \sum_{i=1}^{n} X(f_i)$$

(2.34)

$H_n(f_1, f_2, \cdots, f_n)$ is the nth order transfer function. Take the Fourier transformation of $Y(f)$, then in the time-domain we have

$$y(t) = \sum_{n=1}^{\infty} \int_{-\infty}^{\infty} d\tau_1 \int_{-\infty}^{\infty} d\tau_2 \cdots \int_{-\infty}^{\infty} d\tau_n h_n(\tau_1, \tau_2, \cdots, \tau_n) x(t - \tau_1) x(t - \tau_2) \cdots x(t - \tau_n)$$

(2.35)

This is the normal form of the Volterra series. The n dimensional function

$$h_n(\tau_1, \tau_2, \cdots, \tau_n) \tag{2.36}$$

is called the nonlinear impulse response of order n, or the nth Volterra kernel. Determination of the Volterra kernel is normally performed using the harmonic

probing method. This operation is complex, particularly when evaluating higher order kernels. The Volterra series technique therefore is best suited for the analysis of circuits with a fixed topology and mild nonlinearities that are adequately described by up to the third order Volterra kernels.

There is a common limitation involved in all the above-mentioned methods— the time domain analysis, the harmonic balance analysis, and the Volterra series. That is, they require a circuit model consisting of lumped components. Unlike a familiar circuit of lumped nonlinear components, however, the nonlinearity of a superconductor is distributed along the conducting material from which the circuit is constructed. Thus, it is difficult, if not impossible, to model a superconductor microwave circuit with some simple lumped elements.

2.7   Nonlinear analysis for HTSC microwave circuits

The analysis of the nonlinear behaviors in HTSC microwave circuits can be carried out either in the time-domain or in the frequency-domain.

During the past decade, a frequency-domain analysis approach, *harmonic balance technique*, has been widely used in nonlinear microwave circuits because of its simplicity and less demand of computing memory [19]. In this technique, usually, the lumped element model for the nonlinear device under investigation has to be known. For instance, [15] and [21] use the harmonic balance technique to analyze HTSC stripline and microstrip filters, in which the HTSC transmission lines are treated simply as a nonlinear lumped or semi-lumped components. These treatments are, however, not very accurate at high frequencies because of their neglecting

of fringing fields and mutual coupling.

For a rigorous nonlinear analysis, some authors resort to the time-domain solutions. They directly solve a system of time-dependent partial differential equations in the time-domain [22, 23]. In [23], a formulation based on the GL equation and a nonlinear finite-difference time-domain(FDTD) technique is applied to a single HTSC microstrip line. In this approach, however, the computation is very intensive in terms of CPU time and memory.

The usual way to analyze a microwave circuit is to use a set of S-parameters and Y-parameters. However, these parameters are fundamentally linear concepts and cannot be used to characterize a nonlinear circuit. To date, to our knowledge, there is no fast convergent integral equation method that is used to analyze distributed nonlinear microwave circuits. This research is to correct this limitation.

In this study two nonlinear modeling approaches will be proposed for the analysis of the distributed-type HTSC nonlinearity. They are the *MoM-HB combination method* based on the moment method(MoM) and the harmonic balance(HB) technique and the *power series method.*

2.7.1 The MoM-HB combination method

The MoM-HB combination method is based on the combination formulation of the moment method and the harmonic balance technique. The moment method is used for linear electromagnetic field analysis and the harmonic balance technique for nonlinear analysis. Thus, it consists of a linear solver and a nonlinear solver.

The outline of the MoM-HB combination method is as follows: In the linear solver, the integral equation obtained from the boundary condition is solved by using the moment method. An appropriate Green's function is employed, so

that the field interactions and fringing fields outside the HTSC material are taken into consideration. In the nonlinear solver, the nonlinear $v - i$ characteristic of HTSC material is modeled by using a power series in the time-domain and Fourier-transforming it into the frequency domain. The harmonic balance technique is used to match the voltages by the linear components(including the sources) and nonlinear components at each frequency to obtain the so-called harmonic balance equation. The harmonic balance equation is solved by an iterative procedure.

As compared with the differential equation FDTD-based approach [23], this method is basically an integral equation approach, which is substantially faster than a differential FDTD approach. Since the method proposed has the basic features of the moment method and the harmonic balance technique, it is efficient, accurate, and suitable for both weak and strong nonlinearities.

2.7.2   The power series method

The outline of the power series method is as follow: By following the moment method formulation, the integral equation is expressed as the following matrix form equation:

$$[Z][I] = [V] \tag{2.37}$$

in which the self terms in the impedance matrix $[Z]$ contain the contribution from the surface impedance. The current distribution $[I]$ over the conducting surface is then found for a voltage excitation $[V]$ at the fundamental frequency by solving the matrix equation. The current will generate a voltage that contains many harmonic frequency components due to the nonlinear surface impedance of each current segment over the superconducting surface. With the current over the superconducting surface known, the third and higher, and intermodulation, voltage harmonics over

the conducting surface can be found by means of the nonlinear characteristic of HTSC material. The voltage harmonic at each point is considered as an excitation on that current segment. With the segment excitations assembled, the circuit is then solved again by the same moment method at that higher order frequency for the corresponding current distribution. If the circuit is constructed from conducting strips, the uneven current distribution across the strip—peaking at the edges—can be accounted for by integration of the voltage harmonics across the strip.

The power series method is a simple solution to weak nonlinearity. It is simple for finding the output powers at higher order harmonics. Compared with the MoM-HB combination method, the power series method is much faster, in that there is no any iteration involved and each harmonic is treated separately.

2.8   Conclusions

In this chapter we have introduced the phenomenological electromagnetic theory. Inside a superconductor there are normal current and supercurrent flowing through. The relations between the supercurrent and the electric and magnetic fields are governed by the two London's equations. The Meissner effect can be explained by solving the London's equation inside material. The penetration depth is independent of the frequency. The conductivity is a complex number. The surface resistance for superconductor at low fields is proportional to the square of the frequency, whereas the surface resistance at high fields is a quadratic function of the magnetic field based on experimental observation. Primarily, HTSC nonlinearity is due to the flux line motion and grain boundaries in the superconductor. We have also reviewed time-domain and frequency-domain approaches for nonlinear analysis. The time-domain methods are usually computation intensive. Whereas the frequency-

domain methods are fast and need less computer memory, however, lumped circuit model of the circuits under consideration has to be known in order to enable the frequency-domain methods. Therefore, for superconductive nonlinearity, which is a distributed-type nonlinearity, we have proposed two nonlinear analysis approaches in this study. These two approaches will be explained in details and applied to the nonlinear analysis of HTSC microstrip circuits in this thesis.

Chapter 3

Integral equation and the moment method

3.1 Introduction

In Chapter 2 we mentioned briefly that the proposed MoM-HB combination method for nonlinear analysis was developed by combining the moment method formulation and the harmonic balance technique. The analysis is composed of two parts: linear and nonlinear solvers. The linear solver carries out the linear analysis in the frequency-domain by using the moment method and adopting the complex image Green's function[24], so that the field interactions and fringing fields can be taken into consideration. The nonlinear solver performs the nonlinear analysis by using the harmonic balance technique. The nonlinear $v - i$ characteristic of HTSC material, which is modeled by a power series in the time-domain, is Fourier-transformed into the frequency-domain to fit into the so-called harmonic balance equation. An iterative procedure is then employed to solve the harmonic balance equation for the

current distributions at different frequency components.

In this chapter and the next we will have a detailed description about the MoM-HB combination method. In this chapter we explain how to develop the linear solver by using the moment method and the complex image technique. We will describe how to develop the nonlinear solver by means of the harmonic balance technique in next chapter.

In Section 3.2 the integral equation formulation is derived for a general microstrip planar circuit problem. In Section 3.3 the moment method is used to turn the integral term into a matrix form. In Section 3.4 the Green's function is described by using the efficient *complex image technique*. In Section 3.5 the evaluation of Ψ integral is explained. Finally Section 3.6 concludes this chapter.

3.2 Integral equation formulation

The formulation of electromagnetic boundary value problems in terms of an integral equation has been established and proven to be the most rigorous framework for analyzing a wide class of problems involving conducting objects of arbitrary geometries in multi-layered media. One of the attractive features of this formulation is that the boundary conditions of the problems are intrinsically accounted for in the functional form of the integral equation.

A typical microstrip circuit structure is illustrated in Figure 3.1, where the conducting material is constructed from HTSC thin film for a HTSC microstrip circuit. When there exists an incident field, the surface current will be induced on the surface of the conducting material. The current will in turn generate a scattered electric field.
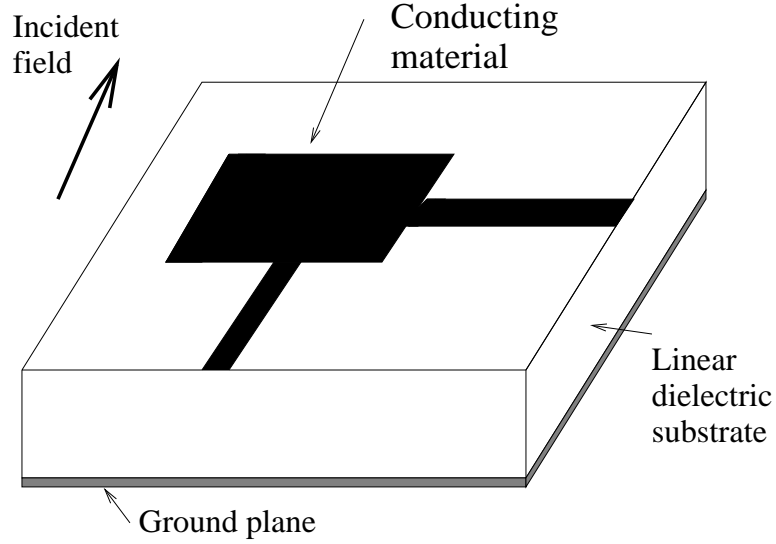
Figure 3.1: Diagram of a HTSC microstrip circuit structure

In the integral equation approach, the electromagnetic fields are represented in terms of the scattered vector and scalar potentials, which themselves can be represented in terms of the fundamental sources of electromagnetic fields, i.e., charges and currents, through a Green's function type of integral equation. The scattered electric and magnetic fields intensities **E** and **H** can be represented by the following set of equations with respect to the auxiliary magnetic vector potential **A** and the scalar electric potential Φ:

$$\mathbf{E}(\mathbf{r}) = -j\omega\mathbf{A}(\mathbf{r}) - \nabla\Phi(\mathbf{r}) \tag{3.1}$$

$$\mathbf{H}(\mathbf{r}) = \nabla \times \mathbf{A}(\mathbf{r}) \tag{3.2}$$

where

$$\mathbf{A}(\mathbf{r}) = \mu \int_s \bar{\bar{G}}_A(\mathbf{r}|\mathbf{r}') \cdot \mathbf{J}_s(\mathbf{r}')ds' \tag{3.3}$$

$$\Phi(\mathbf{r}) = \frac{1}{\epsilon} \int_s G_q(\mathbf{r}|\mathbf{r}')\rho_s(\mathbf{r}')ds' \tag{3.4}$$

where μ and ϵ are the permeability and permittivity of the field layer, respectively, $\mathbf{J}_s$ and ρ_s are the surface current and surface charge densities, respectively, $\mathbf{r}$ and $\mathbf{r}'$ are the position vectors of the field point and source point, respectively, $\bar{\bar{G}}_A$ and G_q are the vector and scalar potential Green's functions, respectively. These Green's functions account for the effect of the multi-layered medium. For the free space case, the Green's functions would each be of the form

$$\frac{e^{jkR}}{4\pi R}$$

The relation between $\mathbf{A}$ and Φ is known as the Lorentz gauge:

$$\Phi = -\frac{1}{j\omega\mu\epsilon}\nabla \cdot \mathbf{A} \tag{3.5}$$

The fact that a conductor has a finite conductivity implies that there will be some dissipation or ohmic loss in the conductor. Therefore, to solve for the scattered electric field, the relation between the scattered field $\mathbf{E}^s$ and the incident field $\mathbf{E}^i$ on an impedance surface should satisfy the following boundary condition:

$$\mathbf{n} \times \left(\mathbf{E}^i(\mathbf{r}) + \mathbf{E}^s(\mathbf{r})\right) = Z_s\mathbf{n} \times \mathbf{J}_s(\mathbf{r}) \tag{3.6}$$

where $\mathbf{J}_s$ is the surface current density induced on the conductor surface, and $Z_s = R_s + jX_s$, is the surface impedance of the conducting material, and $\mathbf{n}$ is a unit normal vector to the surface of the conducting object.

Substituting (3.1) into (3.6) yields

$$\mathbf{n} \times (j\omega\mathbf{A}(\mathbf{r}) + \nabla\Phi(\mathbf{r})) + Z_s\mathbf{n} \times \mathbf{J}_s(\mathbf{r}) = \mathbf{n} \times \mathbf{E}^i(\mathbf{r}) \tag{3.7}$$

Using the integral representations of $\mathbf{A}$ and Φ as given in (3.3) and (3.4), respectively, the above equation becomes:

$$\mathbf{n} \times \left(j\omega\mu \int_s \bar{\bar{G}}_A(\mathbf{r}|\mathbf{r}') \cdot \mathbf{J}_s(\mathbf{r}')ds' + \nabla \int_s G_q(\mathbf{r}|\mathbf{r}')\frac{\rho_s(\mathbf{r}')}{\epsilon}ds'\right) + Z_s\mathbf{n} \times \mathbf{J_s}(\mathbf{r}) = \mathbf{n} \times \mathbf{E}^i(\mathbf{r}) \tag{3.8}$$

where the relation between the charge density ρ_s and the current density $\mathbf{J}_s$ is given by the continuity equation:

$$\rho_s(\mathbf{r}') = \frac{-1}{j\omega}\nabla'_t \cdot \mathbf{J}_s(\mathbf{r}') \tag{3.9}$$

Equation (3.8) is known as the mixed potential integral equation (MPIE), which involves both the vector potential expressed in terms of the induced current, and the scalar potential expressed in terms of the induced charge. The MPIE is a convenient choice of formulation, because it requires only the *potential* forms of the Green's functions, which is of the reduced singularity at the source point.

3.3   Moment method formulation

The moment method developed by Harrington [26] is most frequently chosen to solve the integral equation (3.8) for the surface current $\mathbf{J}_s$, since the moment method is such a flexible variational method to model printed circuit structures of arbitrary shape and orientation metalization. In this section we show how this method is applied to conducting surfaces confined to horizontal layers. Practical examples for this case include microstrip circuit and printed circuit antennas. In the derivation of the moment method formulation, we assume that the thickness of the metalization is infinitely thin.

The procedure to solve the integral equation (3.8) is to express the current by a finite sum of *basis* functions, which describe the current distribution along the transverse and axial directions. The resulting equation is then multiplied by a *weighting* (*testing*) function and is integrated to obtain a system of impedance matrix equation. It is then solved for the unknown current expansion coefficients.

To apply this procedure, we use the following expansion of the current

$$\mathbf{J}_s(r') = \sum_{n=1}^{N} I_n f_n(x') g_n(y') \mathbf{l_n} \tag{3.10}$$

where I_n, $n = 1, \cdots, N$, is the unknown constant expansion coefficients of the current on the nth current segment, $g_n(y')$ is the transverse current distribution (i.e., as a function of the width of the segment), $f_n(x')$ is the longitudinal current distribution (i.e., as a function of the length of the segment), and $\mathbf{l_n}$ represents the unit vector in the longitudinal direction. The above expansion of the current requires dividing the conducting surface area into K small sub-areas, as shown in Figure 3.2, where the centers of the sub-areas are treated as the *charge nodes*, and the *current segments* are identified by the connected lines between two adjacent charge nodes. In Figure 3.2, a current segment labeled n starts with charge node n^- and ends with charge node n^+. To enable analysis of arbitrary microstrip shapes, these basis functions are normally defined over a sub-area of the metalization. The current in the longitudinal distribution f_n and the transverse distribution g_n should be considered.

The next step in the moment method is to select a weighting function of a form the same as the basis function:

$$\mathbf{W_m}(\mathbf{r}) = f_m(x) g_m(y) \mathbf{l_m}, \quad m = 1, \cdots, N \tag{3.11}$$

This particular choice is known as the Galerkin's method, in which the weighting function is proportional to the basis function. This has been found to be the best choice to minimize the error in solving for the unknown current expansion coefficients, due to the variational properties of the resulting impedance matrix elements. Thus, it enhances the accuracy of the moment method significantly.
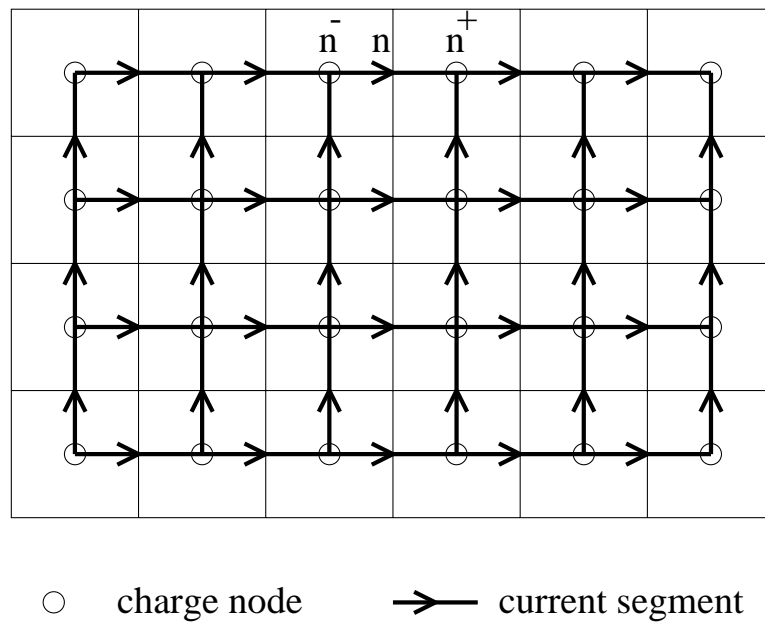
Figure 3.2: Diagram of gridding of a HTSC microstrip surface with charge nodes and current segments

Now let us define the operation for the inner product of two functions as

$$< x_1, x_2 >= \int_s x_1 \cdot x_2 ds \qquad (3.12)$$

Using this definition, the inner product of the weighting function $\mathbf{w_m}(\mathbf{r})$ with the integral equation (3.8) gives:

$$\sum_{n=1}^{N} (F_{mn} + C_{mn}) I_n + \sum_{n=1}^{N} D_{mn} I_n = \int_s (\mathbf{n} \times \mathbf{E}^i) \cdot g_m(y) f_m(x) \mathbf{l_m} ds \qquad (3.13)$$

where the surface s includes all the circuit metalization, F_{mn} and C_{mn} are the Faraday and Coloumb terms, respectively, and D_{mn} represents the conductor loss due to the surface impedance Z_s. They are found as follows:

$$F_{mn} = j\omega\mu \int_s g_m(y) f_m(x) \left(\int_{s'} \mathbf{l_m} \cdot \bar{\bar{G}}_A(r|r') \cdot \mathbf{l_n} g_n(y') f_n(x') ds' \right) ds \qquad (3.14)$$

$$C_{mn} = \frac{-1}{j\omega\epsilon} \int_s g_m(y) f_m(x) \mathbf{l_m} \cdot \left(\mathbf{l_n} \frac{\partial}{\partial l_m} \int_{s'} G_q(r|r') \frac{\partial}{\partial l_n} \left[g_n(y') f_n(x') \right] ds' \right) ds \qquad (3.15)$$

$$D_{mn} = \int_s g_m(y) f_m(x) \mathbf{l_m} \cdot \left[Z_s g_n(y') f_n(x') \mathbf{l_n} \right] ds \qquad (3.16)$$

Note that it is better to separate D_{mn} from F_{mn} and C_{mn} in (3.13), since D_{mn} is related to the conducting material.

In order to derive F_{mn}, the axial current distribution functions, f_m and f_n, in the basis and weighting functions in the Faraday term (3.14) are chosen to be *pulse* functions. Although the choice of pulse function does not satisfy the continuity equation (3.9), it has been shown in [28] that it has very little effect on the moment method solution. Moreover, the choice of pulse basis and weighting functions has been shown to significantly reduce the computation time. Hence, the expression of F_{mn} in (3.14) reduces to:

$$F_{mn} = j\omega\mu\Delta l_m \Delta l_n (\mathbf{l_m} \cdot \mathbf{l_n}) \Psi_A(m, n) \qquad (3.17)$$

where

$$\Psi_A(m,n) = \frac{1}{\Delta l_m \Delta l_n} \int_s \int_{s'} g_m(y) g_n(y') G_A^{xx}(r|r') ds' ds \qquad (3.18)$$

where Δl_m and Δl_n correspond to the length along the axial direction of the mth and nth current segments, respectively.

Whereas, in order to derive C_{mn}, the axial current distribution functions, f_m and f_n, in the basis and weighting functions in the Coloumb term (3.15) are chosen to be *triangular* functions. In view of the continuity equation (3.9), the choice of triangular basis functions for the axial current is equivalent to choosing a positive and a negative pulse for the axial charge distribution in each segment. In this case, C_{mn} in (3.15) becomes:

$$C_{mn} = \frac{1}{j\omega\epsilon} \left(\Psi_q(m^+, n^+) - \Psi_q(m^+, n^-) - \Psi_q(m^-, n^+) + \Psi_q(m^-, n^-) \right) \qquad (3.19)$$

where

$$\Psi_q(m,n) = \frac{1}{\Delta l_m \Delta l_n} \int_s \int_{s'} g_m(y) g_n(y') G_q(r|r') ds' ds \qquad (3.20)$$

For the conductor loss term D_{mn}, the axial current distribution functions, f_m and f_n, in the basis and weighting functions are chosen to be the pulse functions, then we obtain:

$$D_{mn} = \delta_{mn} \int_s g_m(y) g_n(y') Z_s ds = \delta_{mn} Z_D \qquad (3.21)$$

where δ_{mn} is the Kronecker delta, which is 1 for $m = n$, otherwise is zero.

The right hand side of (3.13) contains the excitation field $\mathbf{n} \times \mathbf{E}^i$, which is modeled as a gap generator in our analysis. That is, $\mathbf{n} \times \mathbf{E}^i$ is zero everywhere on the metalization except at the source segment e, where it is represented by

$$\mathbf{n} \times \mathbf{E}^i = \frac{V_e}{\Delta l_e} \mathbf{l_e} \qquad (3.22)$$

where V_e is the magnitude of the source, Δl_e is the length of the source segment, and $\mathbf{l_e}$ is a unit vector. By substituting the above expression into the right hand

side of (3.13) and choosing the pulse function for both $g_m(y)$ and $f_m(x)$, the right hand side of (3.13) is equal to V_e. Thus we have

$$\sum_{n=1}^{N}(F_{mn} + C_{mn})I_n + \sum_{n=1}^{N}\delta_{mn}D_{mn}I_n = V_e \tag{3.23}$$

The above equation can be written in a matrix form

$$[Z_{mn}][I_n] + \sum_{n=1}^{N}\delta_{mn}Z_D I_n = [V_m] \tag{3.24}$$

where the impedance matrix elements are composed of two terms, i.e.,

$$Z_{mn} = F_{mn} + C_{mn} \tag{3.25}$$

Substituting (3.17) and (3.19) into (3.25) yields

$$\begin{aligned}
Z_{mn} &= j\omega\mu\Delta l_m \Delta l_n (\mathbf{l_m} \cdot \mathbf{l_n})\Psi_A(m,n) \\
&\quad + \tfrac{1}{j\omega\epsilon}\left(\Psi_q(m^+, n^+) - \Psi_q(m^+, n^-) - \Psi_q(m^-, n^+) + \Psi_q(m^-, n^-)\right)
\end{aligned}$$
$$\tag{3.26}$$

In order to find the impedance matrix Z_{mn}, we must know the Green's functions, $\bar{\bar{G}}_A$ in (3.18) and G_q in (3.20) to find $\Psi_A(m,n)$ and $\Psi_q(m,n)$. In the next section, we shall show how to use the complex image Green's function to find them.

3.4 Complex image Green's function

From the previous section, we know that the problem of electromagnetic scattering and radiation by the surfaces of arbitrary shape in multi-layered media has been formulated in terms of a space-domain MPIE. The solution of this integral equation requires knowledge of the *spatial* Green's functions of the vector and scalar potentials. They are given by the inverse Fourier transformation of the corresponding *spectral* expressions.

By using the concept of plane wave transmission to model the dipole radiation in multi-layered media, the *general* expressions for the spectral Green's functions can be derived. To this end, the expressions of the vector and scalar potentials due to an infinitesimal dipole source in a homogeneous medium are first derived. The solution is then generalized to the case of a dipole radiating in multi-layered media. It is found that the dipole field in spectral domain consists of TE_z and TM_z type plane wave spectra. The interaction of these plane waves with the multi-layered media defines the *spectral transmission coefficients*. Then the general expressions of the vector and scalar potential Green's functions in terms of the TE_z and TM_z spectral transmission coefficients are derived. It is found that the scalar potential Green's function is different for charges associated with a vertical electric dipole(VED) or a horizontal electric dipole(HED). An arbitrary oriented dipole can always be decomposed into two parts: a vertical component and a horizontal component. Therefore, the radiation from an arbitrarily oriented electric dipole can always be described by the superposition of the radiation from a VED and a HED.

The success in solving electromagnetic radiation and scattering problems lies in reducing the computation time of evaluating the Sommerfeld integrals to obtain the spatial Green's functions. This is because these integrals are involved in the calculation of the impedance matrix elements generated from the moment method modeling of large complex circuits. Fortunately, this integral has been computed efficiently by using the *complex image technique*.

The complex image technique was first introduced by Fang *et al* [29] and later improved by Chow *et al* [24]. In this technique, the spectral function is sampled at a finite number of points, and a short series of complex exponential functions is constructed from these sample points. The time-consuming Sommerfeld integral can then be replaced by a short series of complex images having complex amplitudes

and locations. The complex image technique provides a rapidly-convergent full wave spatial Green's function and is, therefore, considered as the *most efficient* technique to calculate the Sommerfeld integrals. It has been used successfully to solve different multi-layered media problems, such as coplanar waveguide circuits [30], the effect of packaging on microwave integrated circuits [31], and dipole antennas [32].

The derivation of the spatial Green's function is started by providing the spectral expressions of the various components of the vector and scalar potentials due to both an x-directed HED and a z-directed VED, located above a microstrip substrate. The corresponding spatial Green's functions can be obtained in closed-form expressions from the spectral Green's functions. A closed-form expression contains contributions of the quasi-dynamic images, complex images, and surface waves. At different distances, certain contributions may be small and can be dropped without causing much error in the spatial Green's function.

The spatial Green's function due to the source and the quasi-dynamic images is as follows:

$$G_0 = \frac{e^{jk_0r_0}}{4\pi r_0} + \sum_{n=0}^{\infty}\left(K^{n+1}\frac{e^{-jk_0r_{n1}}}{4\pi r_{n1}} - K^n\frac{e^{-jk_0r_{n2}}}{4\pi r_{n2}}\right) \tag{3.27}$$

where

$$r_{n1} = \sqrt{\rho^2 + [z + z' + 2nh]^2}, \quad r_{n2} = \sqrt{\rho^2 + [z + z' + 2(n+1)h]^2} \tag{3.28}$$

The expression in (3.27) is the low-frequency approximation of the scalar potential Green's function G_q. A similar result was derived on a purely physical basis by Chow [33], where it was shown that the quasi-dynamic images are dominant in the near-field region. To avoid excessive computations of the above series in (3.27), we truncate it so that only the terms corresponding to $n = 0$ and $n = 1$ are considered. The remaining terms will be included in the complex images.

The spatial Green's function due to the surface wave poles is given as:

$$G_{sw} = \frac{1}{4\pi}(-2\pi j)Res_p e^{jk_0(z+z')}H_0^{(2)}(k_{\rho p}\rho)k_{\rho p} \tag{3.29}$$

One can see that the spatial radial dependence of the surface wave is given by the Hankel function $H_0^{(2)}$, which behaves asymptotically as $\rho^{-1/2}$.

The spatial Green's function due to the complex images is given as:

$$G_{ci} = \sum_{i=1}^{N_{image}} a_i \frac{e^{-jkr_i}}{4\pi r_i} \tag{3.30}$$

where r_i is a complex distance and given by

$$r_i = \left[\rho^2 + \left(z + z' - \frac{b_i}{k_0}\right)^2\right]^{1/2} \tag{3.31}$$

The Green's function in (3.30) is interpreted as that due to a set of N complex images that have complex amplitudes (a_i) and complex locations $(z = -z' + b_i/k)$. The complex images are related to the leaky waves and are important in the intermediate field region, which represents the transition from the near-field region, where the quasi-dynamic images dominate, to the far-field region, where the surface waves dominate.

The completed form of the spatial Green's function is that by adding the contributions due to the quasi-dynamic images, complex images, and surface waves, that is

$$G_q = G_0 + G_{ci} + G_{sw} \tag{3.32}$$

This is a closed-form expression for the full-wave spatial Green's function and valid for all source-to-field distances on the substrate surface. Other Green's function components can be obtained in closed-form spatial expressions similar to (3.32). Using the derived closed-form Green's function expressions for the spatial functions in a variational techniques, i.e., the moment method, results in substantial savings of computation time when analyzing planar microstrip structures.

3.5 The evaluation of Ψ integrals

It is desirable to evaluate Ψ integrals in (3.18) and (3.20) in closed-form expressions, as this would greatly reduce the fill-in time of the impedance matrix and make the application of the moment method efficient and rapidly convergent. In the following, we will show how to evaluate such integrals by using the definition of an effective distance $R_{i,eff}$ between two current segments m and n.

Each of the Green's functions involved in the Ψ_A and Ψ_q integrals have been determined in closed-form by using the complex image technique as given in (3.32). Therefore, a typical Ψ integral takes the form

$$\Psi(m,n) = \frac{1}{\Delta l_m \Delta l_n} \int_s \int_{s'} g_m(y) g_n(y') \left[\frac{e^{-jkR_0}}{4\pi R_0} + \sum_{i=1}^{N_{image}} a_i \frac{e^{-jkR_i}}{4\pi R_i} + \sum_{i=1}^{N_{pole}} s w_i H_0^{(2)}(k_{\rho i}\rho) \right] ds' ds$$

$$(3.33)$$

The first term in the bracketed expression corresponds to the source term of the Green's function, the second term is a summation of the images (including the quasi-dynamic images and complex images), and the third term represents the surface wave contribution of the Green's function. So N_{image} denotes the total number of images including the quasi-dynamic images and complex images, and N_{pole} the total number of surface wave poles. If the size of the surface of the nth or mth charge nodes is small compared to the wavelength, then the following expansion of the Ψ integral in (3.33) is possible, that is,

$$\Psi(m,n) = \frac{e^{-jkR_{0,eff}}}{4\pi R_{0,eff}} + \sum_{i=1}^{N_{image}} a_i \frac{e^{-jkR_{i,eff}}}{4\pi R_{i,eff}} + \sum_{i=1}^{N_{pole}} s w_i H_0^{(2)}(k_{\rho i} R_{0,eff}) \qquad (3.34)$$

where the effective distance $R_{i,eff}$ is defined as

$$\frac{1}{R_{i,eff}} = \frac{1}{\Delta l_m \Delta l_n} \int_s \int_{s'} g_m(r) g_n(r') \frac{1}{R_i} ds' ds \qquad (3.35)$$

in which the distance R_i, $i = 0, 1, 2, \cdots, N_{image}$, is given by:

$$R_i = \begin{cases} [\rho^2 + (z - z')^2]^{1/2} & i = 0 (\text{source term}) \\ [\rho^2 + (z + z' - b_i/k)^2]^{1/2} & 1 \leq i \leq N_{image} (\text{image terms}) \end{cases} \tag{3.36}$$

The validity of the approximation in (3.34) is shown in Appendix B. The computation of $R_{i,eff}$ integral can be found in [30, 31, 32].

3.6 Conclusions

In this chapter the linear solver in the proposed MoM-HB combination method was described. The mixed potential integral equation (MPIE) involving the spatial forms of the vector and scalar potential Green's function was developed for an impedance surface. Then the moment method was employed to solve the MPIE. That resulted in a matrix equation form, in which the unknowns are the current expansion coefficients. The complex image technique was applied to find the Green's function in a closed-form expression. Thus the impedance matrix characterizing the field outside the conducting material could be given in terms of Ψ integrals, which were evaluated efficiently by using the concept of the effective distance $R_{i,eff}$.

In order to deal with the term related to the surface impedance of the material in the matrix equation, we have to do nonlinear analysis. Because the surface impedance of HTSC material is a nonlinear function of the applied power. This is the topic of the next chapter, where the nonlinear solver in the MoM-HB combination method will be described.

Chapter 4

Harmonic analysis

4.1   Introduction

We just formulated the linear solver in the proposed MoM-HB combination method in the previous chapter. In this chapter we continue explaining the MoM-HB combination method by formulating the nonlinear solver.

We have known that the method consists of linear and nonlinear solvers. The linear solver is obtained by using the moment method and the complex image Green's function. On the other hand, The nonlinear solver uses the harmonic balance technique to perform the nonlinear analysis. A power series in the time-domain is used to model the nonlinear $v - i$ characteristic of HTSC material. After it is Fourier-transformed into the frequency-domain, we can obtain the harmonic balance equation. An iterative procedure is employed to solve the harmonic balance equation for the current distributions at different frequency components.

In this chapter, we first consider the surface impedance as a nonlinear function of the current, so we can perform harmonic analysis to arrive at a system of harmonic

balance equations. Then we solve the harmonic balance equations by using an iterative procedure.

4.2 Harmonic balance equation

In equation (3.8), the first term in the left hand side is the sum of two integrals. In previous chapter we have used the moment method and complex image technique to turn it to the product of an impedance matrix and a current column vector. The second term in the left hand side of (3.8) is associated with the surface impedance. For HTSC materials, the surface impedance Z_s is no longer a constant but depends on the surface current density $\mathbf{J_s}$. The term in the right hand side of (3.8) is related to the source. So, generally speaking, (3.8) is a nonlinear equation. Thus, this leads to the generation of new harmonically related frequencies. Characterization of a nonlinear material must be done by a time-domain model. In this study, only the nonlinear effect due to R_s is considered. The nonlinear effect of X_s results in only the shift of the resonant frequency and it is not treated in this study.

Basically, Equation (3.8) is an equation of the following general operator form:

$$V_i + L(J_s) = NL(J_s) \tag{4.1}$$

where V_i represents the applied source voltage corresponding to the source term in (3.8), L represents a *linear* operator corresponding to the integral terms in (3.8) in which the *total field* interaction outside and on the structure at the fundamental and harmonic frequencies is taken into account by standard linear field analysis technique, and NL represents a *nonlinear* operator corresponding to the surface impedance term which characterizes the property of a nonlinear material. Thus, equation (4.1) is the harmonic balance equation [19], in which the total voltages

generated by the linear parts (including sources) should match the total voltages generated by the nonlinear parts at each harmonic frequency.

In the previous chapter we have known that the linear operator in (4.1) can be presented as an integral form in terms of the induced surface current density $\mathbf{J_s}$ by using the Green's function. Then the moment method is employed to do the linear analysis to take the field coupling effects into account. In the standard procedure when the moment method is applied, the HTSC strip is then divided into N segments. This may be electrically considered as an N-port network, with each segment corresponding to each port. For each segment, the voltage by linear parts should match the voltage by nonlinear parts.

Figure 4.1(a) illustrates a section of the segmented planar transmission line, and an equivalent nonlinear circuit representation for one of the segments is shown in Figure 4.1(b), where the nonlinearity of the material is lumped into a nonlinear impedance, Z_{NL}, and the linear circuit consists of a linear voltage source, V_i, and a linear impedance, Z_L. Note that the effect of substrate is included in the Z_L, since in this modeling we only consider that the substrate is made of linear materials. At the connection nodes between linear and nonlinear parts, the linear voltage, V_L, should match the nonlinear voltage, V_{NL}, at each different frequency.

4.2.1 Linear part

The linear parts in equation (4.1) have been expressed in a matrix form in the previous chapter. That is, from (3.24) the linear voltage is:

$$V_L = [V_i] - [Z][I] \qquad (4.2)$$

where $[Z]$ is a *linear* impedance matrix characterizing the field interaction in the surrounding media of the conductor object, $[I]$ represents the currents flowing on
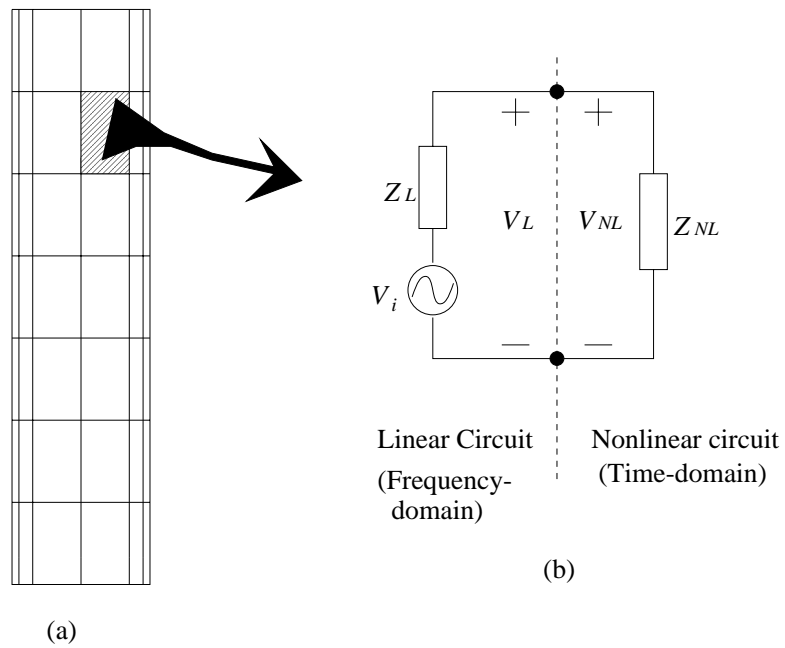
Figure 4.1: Diagram of a section of segmented transmission line and the equivalent nonlinear representation for one of segments

the surface of each segment, and $[V_i]$ represents the applied source voltages. All of above quantities must be known at each harmonic frequency.

If the total K harmonic frequencies, including the fundamental frequency component, are taken into consideration, then $[Z]$ is a $KN \times KN$ *linear* matrix and given as:

$$[Z] = \begin{bmatrix} Z_{11} & Z_{12} & Z_{13} & \cdots & Z_{1N} \\ Z_{21} & Z_{22} & Z_{23} & \cdots & Z_{2N} \\ Z_{31} & Z_{32} & Z_{33} & \cdots & Z_{3N} \\ \vdots & \vdots & \vdots & \ddots & \vdots \\ Z_{N1} & Z_{N2} & Z_{N3} & \cdots & Z_{NN} \end{bmatrix} \tag{4.3}$$

and the elements $Z_{mn}, m, n = 1, 2, \cdots, N$, are all diagonal sub-matrices:

$$Z_{mn} = \begin{bmatrix} z_{mn}(\omega_0) & 0 & 0 & \cdots & 0 \\ 0 & z_{mn}(2\omega_0) & 0 & \cdots & 0 \\ 0 & 0 & z_{mn}(3\omega_0) & \cdots & 0 \\ \vdots & \vdots & \vdots & \ddots & \vdots \\ 0 & 0 & 0 & \cdots & z_{mn}(K\omega_0) \end{bmatrix} \tag{4.4}$$

where $\omega_0 = 2\pi f_0$ is the source fundamental frequency, and $z_{mn}(k\omega_0)$ denotes the mutual impedance between the mth and nth segments and is evaluated at the kth harmonic frequency $(k = 1, 2, \cdots, K)$.

$[I]$ is a $KN \times 1$ column vector and given as:

$$[I] = \begin{bmatrix} I_1 \\ I_2 \\ I_3 \\ \vdots \\ I_N \end{bmatrix} \tag{4.5}$$

and the elements $I_m, m = 1, 2, \cdots, N$, are column vectors:

$$I_m = \begin{bmatrix} I_{m,1} \\ I_{m,2} \\ I_{m,3} \\ \vdots \\ I_{m,K} \end{bmatrix} \tag{4.6}$$

where $I_{m,k}$ denotes the current flowing through the mth segment at the kth harmonic frequency.

Similarly, $[V_i]$ is a $KN \times 1$ column vector given as:

$$[V_i] = \begin{bmatrix} V_{i,1} \\ V_{i,2} \\ V_{i,3} \\ \vdots \\ V_{i,N} \end{bmatrix} \tag{4.7}$$

and the elements $V_{i,m}, m = 1, 2, \cdots, N$, are column vectors:

$$V_{i,m} = \begin{bmatrix} V_{i,m,1} \\ V_{i,m,2} \\ V_{i,m,3} \\ \vdots \\ V_{i,m,K} \end{bmatrix} \tag{4.8}$$

where $V_{i,m,k}$ denotes the source voltage applied to the mth segment at the kth harmonic frequency.

4.2.2 Nonlinear part

For the nonlinear operator in (4.1), we must handle it in the time-domain. The nonlinear characteristic of the material can be modeled by their global $v - i$ curve in the time-domain as follows:

$$v_{NL} = a_1 i + a_3 i^3 \tag{4.9}$$

where the coefficients, a_1 and a_3, are dependent of the geometry of the circuit structure and the coefficients, R_{s0} and R_{s2}, in (2.32) for the surface impedance for HTSC thin film material.

Equation (4.9) is stated in the time-domain, whereas equation (4.2) is stated in the frequency domain. Time-to-frequency conversion is achieved using the Fourier transformation(FT). Since the excitations are sinusoidal signals and the nonlinear $v - i$ curve is a power series, we can take the Fourier series expansion to express the quantities in the time-domain. The quantities at different harmonics in the frequency-domain are simply the coefficients at the corresponding harmonics in the Fourier series.

We now expand the time-domain current, $i(t)$, into a Fourier series in terms of the K harmonic frequencies:

$$i(t) = \sum_{k=1}^{K} I_k \exp(jk\omega_0 t) \tag{4.10}$$

According to the Fourier transformation of a function with the period of T, the current in the frequency-domain, $I(\omega)$, is

$$I(\omega) = \frac{1}{T} \int_{-T/2}^{T/2} i(t) \exp(-jn\omega_0 t) dt \tag{4.11}$$

Substituting (4.10) into (4.11) yields

$$I(\omega) = \frac{1}{T} \int_{-T/2}^{T/2} \left(\sum_{k=1}^{K} I_k \exp(jk\omega_0 t) \right) \exp(-jn\omega_0 t) dt \tag{4.12}$$

By taking the summation sign out of the integral sign, we have

$$I(\omega) = \frac{1}{T} \sum_{k=1}^{K} I_k \int_{-T/2}^{T/2} \exp[j(n-k)\omega_0 t]dt \tag{4.13}$$

The integral in (4.13) is found as:

$$\frac{1}{T} \int_{-T/2}^{T/2} \exp[j(n-k)\omega_0 t]dt = \begin{cases} 1 & n = k \\ 0 & n \neq k \end{cases} \tag{4.14}$$

Substituting (4.14) into (4.13) yields

$$I(\omega) = \begin{cases} I_k & n = k \\ 0 & n \neq k \end{cases} \tag{4.15}$$

Therefore, the coefficient I_k is corresponding to the current amplitude at the kth harmonic frequency in the frequency-domain.

The similar expansion is applied for the voltage $v(t)$ in the time-domain:

$$v(t) = \sum_{k=1}^{K} V_k \exp(jk\omega_0 t) \tag{4.16}$$

where the coefficient V_k corresponds to the voltage amplitudes at the kth harmonic frequency in the frequency-domain. Theoretically, there exist an infinite number of harmonic frequencies. However, the amplitudes at higher frequency components decay very fast. Consequently, they can be ignored. On the other hand, the time-domain quantities can be found by taking the sum of amplitudes at each harmonic frequency.

A system of harmonic balance equations can be obtained by substituting equations (4.3)-(4.8) into equation (4.2) and matching the nonlinear voltage in equation (4.9) at each harmonic frequency. Thus, the equation for the kth harmonic frequency component is as follows:

$$[V_{i,k}] - [Z_k][I_k] = [V_k] \tag{4.17}$$

The discussion of convergence and the number of harmonic used will be given in the next section.

4.3 Iterative procedure

To solve the system of equations in (4.17) for the unknown current in the frequency-domain, I_k, we use an iterative procedure. For this purpose, equation (4.17) is converted into the iterative form for the unknown current I_k:

$$[I_k]^{(p+1)} = [Z_k]^{-1} \left([V_{i,k}] - [V_k]^{(p)} \right) \tag{4.18}$$

where $[*]^{-1}$ represents the inverse of the matrix. The interative procedure is illustrated in Figure 4.2: Starting from the harmonic current amplitudes, I^p, at the pth iteration, we find its time-domain representation, $i(t)$, by taking finite sum of harmonic terms. Then using the time-domain nonlinear equation (4.9), we can find the voltage, $v(t)$, in the time-domain. Then performing the harmonic expansion of the voltage, we can obtain the voltage, V, at each harmonic frequency. Then use equation (4.13) to obtain the current, I^{p+1}, at $(p+1)$th iteration in the frequency-domain.

4.3.1 Convergent criterion

The procedure is repeated until the following convergent criterion is satisfied for each harmonic:

$$Error = \frac{\sum_{m=1}^{N} |I_m^{(p)} - I_m^{(p+1)}|^2}{\sum_{m=1}^{N} |I_m^{(p)}|^2} < eps \tag{4.19}$$

where eps is a pre-designated threshold for error, say 10^{-6}.

$I^{(p)}$

Take the finite harmonic sum of
the frequency-domain currents(K terms)
to find the time-domain current

Use nonlinear v-i relation
to find voltage from current
in the time-domain

Expand the time-domain voltage
expression into a Fourier series

Equate the coefficients in the Fourier
series to the voltages in each harmonic
in the frequency-domain

Find the updated current value by matching
the linear voltage and nonlinear voltage

$I^{(p+1)}$

Compare the two consecutive current values:
If they satisfy the stop criterion, then exit !
Otherwise repeat.

stop

Figure 4.2: Diagram of the iterative procedure in the MoM-HB combination method

4.3.2 Initial guess

The initial guess is very critical for convergence in the harmonic balance technique, especially for the microstrip line circuit because of the edge behavior of the current density distribution over the cross section of a transmission line [35] [37]. If the initial guess is not proper, the iterative procedure becomes divergent. Therefore, in order to get a proper initial guess for current values, in the implementation of the nonlinear solver, the material is first assumed to be linear, and the current density distribution is found. We then take this current density distribution as the initial guess of the current value. In this way the convergence is very fast.

4.3.3 The number of harmonics to be considered

Another important issue is the number of harmonics that has to be included in the simulation in order to obtain reasonable accuracy, and in the meantime, to achieve fast computation. We have applied the same formulation to a microstrip antenna constructed from HTSC material [38]. In that paper, we have tested the frequencies up to the ninth harmonics including the even harmonics. It is found that for weak nonlinearity results are indistinguishable with those by only considering the third and fifth harmonics. In addition, due to the feature of the nonlinearity of HTSC material, that is, the voltage in equation (4.9) is determined only by the odd terms of the current, it is safe to neglect the even harmonics in the implementation. Therefore, only the third and fifth harmonics are included in the implementation.

4.4 Application to HTSC stripline filter

In this section we apply the proposed MoM-HB combination method to a HTSC stripline filter [39]. The purpose is to verify this method.

4.4.1 Two-tone intermodulation

The stripline filter explained in [14] is shown in Figure 4.3(a). In that paper D. E. Oates *et al.* conducted the two-tone intermodulation measurement to observe the output power at the third order frequency, $2f_1 - f_2$, where f_1 is chosen as 1.5 GHz, $f_2 = f_1 + \delta f$, and $\delta f = $ 1KHz. The two signals have the same input power. The length of the line is chosen to be one half wavelength long at the fundamental frequency. The substrate has a thickness of 0.5 mm with $\epsilon_r = 25$. The width of the stripline is 150 μm, so that the characteristic impedance is 50 Ω. The obtained measured results for film #2 were shown in Figure 10 in that paper. In order to do the comparison, we plot them in Figure 4.3(b) and mark them as "measured results".

In order to calculate the output power at the intermodulation frequency by using the proposed MoM-HB combination method, the coefficients in the surface impedance expression (2.32) for the nonlinearity of the HTSC material are found first. They are obtained by curve-fitting to the film #2 measured data at 77k in Figure 8 in that paper and given as follows:

$$R_{s0} = 1.4868 \times 10^{-5}\Omega, \quad R_{s2} = 4.8270 \times 10^{-9}\Omega/Oe^2 \tag{4.20}$$

Figure 4.3(b) shows the simulation results regarding the output powers at the fundamental frequency f_1 and the third order intermodulation frequency $2f_1 - f_2$ as

(a)

(b)
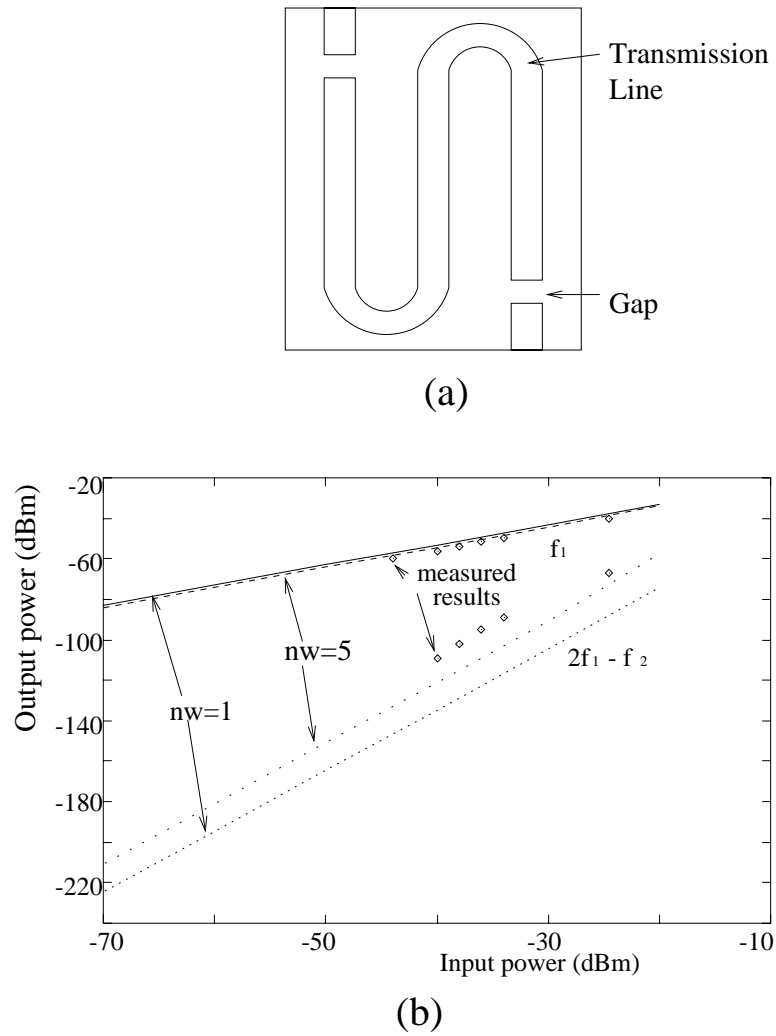
Figure 4.3: Two-tone intermodulation results of a stripline filter from the simulation and measurement. ("nw" is the number of moment method segments along the transverse direction).

a function of the input powers at the fundamental frequency f_1. The measurement results from [14] are also given in the plot for comparison.

Due to the edge behavior of the current density distribution of a stripline [41], one expects that the simulated current density distribution is more accurate with finer gridding put along the transverse direction. The surface resistance of HTSC material is related locally to the magnetic field or the current density, so it is expected that the nonlinear effect is simulated more accurately also with the finer transverse gridding. It is found from Figure 4.3(b) that the third order intermodulation output power obtained with 5 charge cells along the transverse direction of the stripline is 10 dB higher than those with only one charge cell. (In Figure 4.3(b) "nw" is the number of moment method segments along the transverse direction). Thus the results with finer transverse gridding are much closer to the measurement intermodulation results. The measured intermodulation is still larger than that for the 5 charge cell case by about 5%. The remaining discrepancy is probably due to inaccuracy of the local relation between the surface resistance and the current density near the regions around the edges of the conducting strip obtained from (2.32). The simulation accuracy may be improved by using a more accurate local surface resistance relation and more moment method segments along the transverse direction of the stripline.

4.5 Conclusions

In this chapter the nonlinear solver in the MoM-HB combination method has been explained. Due to the nonlinear surface impedance the matrix equation obtained from the moment method was treated as the so-called harmonic balance equation. By using the harmonic balance technique the harmonic analysis was carried out

to both the linear parts and the nonlinear parts. The impedance matrix characterizing the field outside the HTSC material was evaluated at each harmonic frequency. The voltages in the frequency-domain generated by the nonlinear parts were obtained from the coefficients in the Fourier series expansion of the nonlinear $v - i$ characteristic of HTSC material in the time-domain at the corresponding frequency. Then an iterative procedure was employed to solve the harmonic balance equation for the current distributions at each harmonic frequency. Then, the proposed MoM-HB combination method was applied to a stripline filter, where two-tone intermodulation was simulated and compared with the published measurement results. Therefore the method was verified.

Chapter 5

Power series method

5.1   Introduction

In this chapter we introduce the other nonlinear analysis method, called power series(PS) method. In this method the excitation voltage vectors at different harmonics or intermodulation frequencies, due to the nonlinear surface impedance, are derived from the current at the fundamental frequency excitation. With the excitation voltages at different frequency components known, the current distributions at those frequency components can then be found by using the moment method again.

The organization of this chapter is: In Section 5.2 the formulation for the power series method is described in details. Since the conducting material is not a perfect conductor, the first step is to modify the impedance matrix characterizing the conducting material, so that it can take into consideration the effect of the surface impedance. Following this, the excitation voltage vectors, due to nonlinear surface impedance, are derived at the third harmonic frequency and the third or-

60

der intermodulation frequency. Then the calculation of current distribution at the higher order frequencies is explained. The higher order excitation voltage vectors for HTSC strip are derived to take into account the edge current effect of the strip. In Section 5.3 some numerical examples are presented to compare the power series method with the MoM-HB combination methods in order to demonstrate the validity of the power series method. The two methods will be applied to both weak and strong nonlinearity materials. The harmonics higher than the fifth harmonic will also be considered. In Section 5.4 the range of validity and advantage of the power series method are addressed. In Section 5.5 the type of HTSC nonlinearity is identified. Finally, Section 5.6 concludes this chapter.

5.2 Formulation of the power series method

5.2.1 Impedance matrix absorbing the surface impedance

In Chapter 3 we discussed how to formulate a general microstrip circuit problem by using the integral equation technique. Thus, an integral equation is obtained according to the boundary condition on the conducting surface. Then we used the moment method to solve that integral equation, so that we could obtain a matrix form equation.

Here we follow the same idea used in Chapter 3 to do the formulation. We then arrive at the matrix equation (3.24). In the MoM-HB combination method, the first term, which is related the field outside the conducting material, and the second term, which is related to the field on the surface of the conducting material, in the left-hands side of equation (3.24) are manipulated individually. In the power series method, however, the two terms in the left-hand side of the equation are

combined to form an impedance matrix with the surface impedance absorbed into the self terms of the impedance matrix. As a consequence, we arrive at the following matrix equation:

$$[Z][I] = [V] \tag{5.1}$$

where $[V]$ is the source voltage vector applied to each segment, $[I]$ is the unknown current distribution over the conducting surface, and $[Z]$ is the impedance matrix characterizing the conducting material. The formulae for the elements in $[Z]$ are given below:

When $m \neq n$, the mutual impedance elements are calculated by

$$
\begin{aligned}
Z_{mn} &= j\omega\mu(\mathbf{\Delta l_m} \cdot \mathbf{\Delta l_n})\Psi_A(m,n) \\
&\quad + \tfrac{1}{j\omega\epsilon}\left(\Psi_q(m^+,n^+) - \Psi_q(m^+,n^-) - \Psi_q(m^-,n^+) + \Psi_q(m^-,n^-)\right)
\end{aligned} \tag{5.2}
$$

When $m = n$, however, the self impedance should contain the contribution from the surface impedance in that segment, that is

$$
\begin{aligned}
Z_{mn} &= j\omega\mu(\mathbf{\Delta l_m} \cdot \mathbf{\Delta l_n})\Psi_A(m,n) + Z_D\delta_{mn} \\
&\quad + \tfrac{1}{j\omega\epsilon}\left(\Psi_q(m^+,n^+) - \Psi_q(m^+,n^-) - \Psi_q(m^-,n^+) + \Psi_q(m^-,n^-)\right)
\end{aligned} \tag{5.3}
$$

It is worth mentioning at this point that the element Z_{mn} in the impedance matrix $[Z]$ in (5.2) and (5.3) is a function of frequency. Since here we study the effects of new frequencies generated by nonlinearity, it is necessary to keep the dependence of frequency in mind.

5.2.2 Excitation voltage vector at fundamental frequency

In the modeling of the moment method formulation, it is usual to apply a lumped voltage source, v_i, to the current segments at the input port. That is, the excitation

voltage vector has the follow form:

$$[V] = \begin{bmatrix} v_i \\ 0 \\ 0 \\ \vdots \\ 0 \end{bmatrix} \qquad (5.4)$$

It is seen that all elements are zero in the vector $[V]$ except for the current segment at the input port, which is equal to the source voltage.

If the applied source voltage v_i is at fundamental frequency, f, once the matrix equation (5.1) is solved, we can find the current distribution at the fundamental frequency. Since the surface impedance of each current segment over the conducting surface is nonlinear, the current will generate a voltage that contains many harmonic frequency components. If we apply two source voltages at different frequencies to the circuit, then the voltage generated will contain all intermodulation frequency components. Next two sections will address how to find the excitation voltages at those higher order frequencies.

5.2.3   Excitation voltage vectors at higher order frequencies

This section aims to find the higher order voltage excitation vector so as to enable the nonlinear analysis. This is the core of the power series method. We will do this by means of the nonlinear characteristic of the surface impedance of HTSC materials.

As mentioned before, the surface impedance, $Z_s = R_s + jX_s$, of HTSC materials is a function of the local radio frequency (RF) surface magnetic field, H_{rf}. The

dependence of R_s on H_{rf} can be expressed as the quadratic form (2.31). It is copied here:

$$R_s = R_{s0} + R_{s2}H_{rf}^2 \tag{5.5}$$

where R_{s0} and R_{s2} are constants that do not depend upon H_{rf}. In HTSC stripline films case, H_{rf} is the maximum field near the edges of the strip films, R_{s0} is the surface resistance at very low field. It is the H_{rf}^2 term that is primarily responsible for the generation of third harmonic and two different frequency signal intermodulation.

If H_{rf} is represented in the same unit (A/m) as the surface current density, J_s, on the strip, then we have

$$H_{rf} = J_s = \frac{I}{w} \tag{5.6}$$

where w is the width of the stripline and I represents the total current flowing in the stripline. In (5.6) we already make an assumption that the current distribution along the transverse direction of the HTSC strip is uniform. We will discuss the non-uniform current distribution later in this section. Thus (5.5) can be rewritten as:

$$R_s = R_{s0} + R_{s2}J_s^2 \tag{5.7}$$

According to (5.7) we can derive the higher order excitation voltage vectors.

Since the AC impedance of a stripline of a width w is

$$R_{ac} = \frac{R_s}{w}(\Omega/m) \tag{5.8}$$

The tangential electric field on a current segment is

$$E_{tan} = R_s J_s = R_{ac}I \tag{5.9}$$

Therefore, the voltage across each current segment is

$$v = E_{tan}\Delta l = \frac{R_{s0}\Delta l}{w}i + \frac{R_{s2}\Delta l}{w^3}i^3 \tag{5.10}$$

where Δl is the length of that current segment and i is the current flowing through that segment.

5.2.3.1 Excitation voltage vector at the third harmonic frequency

Assume that the sinusoidal current signal is

$$i = i_0 \sin \omega t \tag{5.11}$$

Substituting it into (5.10) and taking the third term into account:

$$\frac{R_{s2} \Delta l}{w^3} i_0^3 \sin^3(\omega t) \tag{5.12}$$

Then using the trigonometric identity, $\sin(3\omega t) = 3\sin(\omega t) - 4\sin^3(\omega t)$ and substituting it into (5.12), we obtain the third harmonic term as follows:

$$-\frac{1}{4} \frac{R_{s2} \Delta l}{w^3} i_0^3 \sin(3\omega t) \tag{5.13}$$

Thus the amplitude is

$$v_3 = \frac{1}{4} \frac{R_{s2} \Delta l}{w^3} i_0^3 \tag{5.14}$$

Note that (5.14) is valid for all segments over the conducting surface.

Once we solve the current flowing through each segment due to the fundamental frequency excitation, the third harmonic excitation voltage vector can be determined by just substituting those segment currents into (5.14).

5.2.3.2 Excitation voltage vector at the third order intermodulation frequency

Consider that the current consists of two sine wave signals:

$$i = i_1 \sin(\omega_1 t) + i_2 \sin(\omega_2 t) \tag{5.15}$$

where ω_1 and ω_2 are the angular frequencies of the two signals. Inserting it into (5.10) and taking the third order term into consideration:

$$\frac{R_{s2}\Delta l}{w^3}[i_1\sin(\omega_1 t) + i_2\sin(\omega_2 t)]^3 \tag{5.16}$$

then we obtain the term with frequency $(2\omega_1 - \omega_2)$ as follows:

$$\frac{3}{4}\frac{R_{s2}\Delta l}{w^3}i_1^2 i_2\sin(2\omega_1 - \omega_2) \tag{5.17}$$

Thus the amplitude is

$$v_{2,-1} = \frac{3}{4}\frac{R_{s2}\Delta l}{w^3}i_1^2 i_2 \tag{5.18}$$

Finally, the excitation voltage vector for two-tone intermodulation can be found by substituting the current distribution solved from (5.1) into (5.18).

One point that is worth emphasizing is that the excitation *voltage* vectors in (5.14) and (5.18) at the higher order frequencies are different from the one in (5.4) at the fundamental frequency. The latter has non-zero elements only for the current segments in the input port, whereas the formers have non-zero elements for all current segments. This is because the higher order excitations stem from the nonlinear surface resistance which is distributed over the *whole* conducting material, i.e., along all current segments.

5.2.4 Current distribution at higher order frequencies

With the current distribution over the conducting surface known, the third and intermodulation voltages over the conducting surface can be calculated from (5.14) and (5.18). The v_3 and $v_{2,-1}$ are then applied to each current segment to excite the circuit, respectively.

With the segment excitations assembled, the circuit is then solved again by the moment method to determine the currents due to these frequency voltages. As mentioned previously that the impedance matrix $[Z]$ is a function of frequency, therefore during the process of reusing the moment method, the impedance matrix must be evaluated again according to the corresponding frequency. Once the current distributions are obtained, the electric fields and powers radiated by these frequency terms can be determined.

The current at the harmonic frequencies higher than the third one, say the fifth and seventh harmonics, also exists and would result in the higher order voltage excitations. But, they are so small that they are not considered here. We will justify this later from obtained numerical results.

5.2.5 Consideration for non-uniform current in HTSC strip

So far we have assumed that the current along the transverse direction of the strip is uniform. As we mentioned so often in this thesis, however, the current distribution over the cross section of the strip are highly non-uniform, i.e., there are two peaks in the current distribution in the region near the edges of the conducting strip. This unique feature of the current distribution will generate stronger nonlinearity than that in the case of the uniform current distribution.

The edge behaviors of the current distribution across a strip is illustrated in Figure 5.1. It is observed that the current density increases at a rate very similar to a perfect conducting case from the middle to a certain distance, λ_L, from the edges, and then keeps a finite value within the scope of λ_L from the edges, instead of being singular at the corners for a perfect conducting case, where λ_L is equal to the *penetration depth* of the superconductor [37].
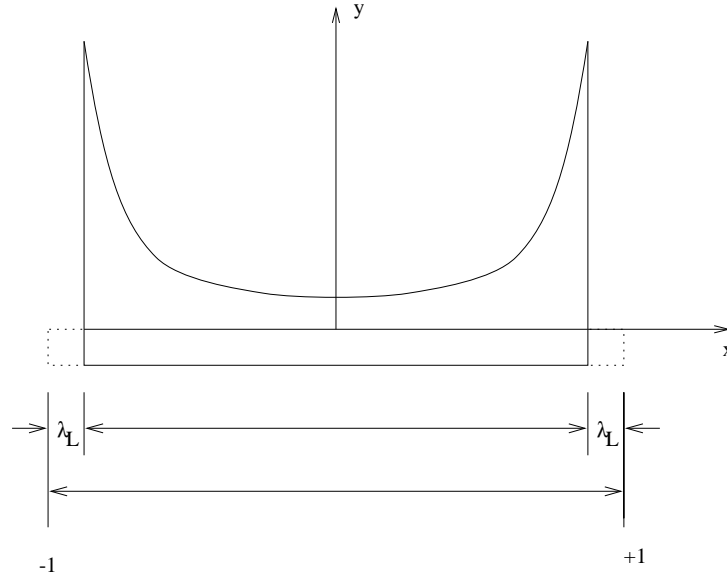
Figure 5.1: Diagram of the current distribution across the strip

According to the assumption made in [12], the transverse variation of the current distribution within the strip can be expressed as:

$$J_s(x) = \frac{J_0}{\sqrt{1 - x^2}} \tag{5.19}$$

where J_0 is a constant and x is from $-(1 - \lambda_L)$ to $(1 - \lambda_L)$. The tangential E field on the strip is given by

$$E_{tan} = R_s J_s(x) \tag{5.20}$$

Substituting R_s in (5.20) by (5.7) yields

$$E_{tan} = R_{s0} J_s(x) + R_{s2} J_s^3(x) \tag{5.21}$$

in which the third order term $R_{s2} J_s^3(x)$ will generate nonlinearity. Next we will derive the higher order excitation voltage vectors from (5.21).

5.2.5.1 Excitation voltage vector at harmonic frequency

If there is just one sine wave signal as the input signal, then from (5.21) the tangential E field for the third harmonic is

$$E_{3,tan} = R_{s2} J_s^3(x) \tag{5.22}$$

The average tangential E field for the third harmonic, $E_{3,ave}$, can be obtained by multiplying J_s in the both sides of (5.22) and integrating them from $-(1 - \lambda_L)$ to $(1 - \lambda_L)$. That is

$$E_{3,ave} I_t = \int_{-1+\lambda_L}^{1-\lambda_L} E_{3,tan} J_s(x) dx \tag{5.23}$$

where I_t is the total current within the strip and given by

$$I_t = \int_{-1+\lambda_L}^{1-\lambda_L} J_s(x) dx \tag{5.24}$$

Therefore, the voltage across each segment on the strip at the third harmonic is

$$v_3 = E_{3,ave} \Delta l = \frac{\Delta l}{I_t} \int_{-1+\lambda_L}^{1-\lambda_L} R_{s2} J_s^4(x) dx \tag{5.25}$$

By applying (5.25) to each segment on the strip, we obtain the excitation voltage vector at the third harmonic frequency.

5.2.5.2 Excitation voltage vector at intermodulation frequency

If there are two sine input signals with different frequencies, ω_1 and ω_2, their current distributions in the strip are $J_1(x)$ and $J_2(x)$, respectively, then by substituting $[J_1(x) + J_2(x)]$ into (5.22) we get

$$E_{tan} = R_{s0}[J_1(x) + J_2(x)] + R_{s2}[J_1(x) + J_2(x)]^3 \tag{5.26}$$

Then, the tangential E field with the third frequency term $(2\omega_1 - \omega_2)$ is

$$E_{(2,-1),tan} = 3R_{s2}J_1^2(x)J_2(x) \tag{5.27}$$

Following the same procedure as that in the single-tone case, we can get the average tangential E field, $E_{(2,-1),ave}$, for the third order intermodulation frequency term $(2\omega_1 - \omega_2)$:

$$E_{(2,-1),ave}I_{t1}I_{t2} = 3R_{s2}\int_{-1+\lambda_L}^{1-\lambda_L}J_1^3(x)dx\int_{-1+\lambda_L}^{1-\lambda_L}J_2^2(x)dx \tag{5.28}$$

where I_{t1} and I_{t2} are, respectively, the total currents within the strip at those two frequencies:

$$I_{t1} = \int_{-1+\lambda_L}^{1-\lambda_L}J_1(x)dx \tag{5.29}$$

$$I_{t2} = \int_{-1+\lambda_L}^{1-\lambda_L}J_2(x)dx \tag{5.30}$$

Therefore, the voltage across each current segment on the strip at that frequency is

$$v_{2,-1} = E_{(2,-1),ave}\Delta l = \frac{\Delta l}{I_{t1}I_{t2}}\alpha\int_{-1+\lambda_L}^{1-\lambda_L}J_1^3(x)dx\int_{-1+\lambda_L}^{1-\lambda_L}J_2^2(x)dx \tag{5.31}$$

5.3 Numerical examples

In this section both the MoM-HB combination method and the power series method are applied to investigate a center-fed strip dipole antenna circuit. The circuit is constructed from nonlinear resistance materials with air dielectric and no ground plane. The antenna has a length of half-wavelength at the fundamental excitation frequency. The source resistance, R_g, at the dipole feed is 72 Ω. The radiation resistance of the dipole antenna is 72 Ω at the fundamental frequency [42, 38]. The

dipole antenna is divided into $N = 31$ segments along its longitudinal direction, and the source is located at the center of the antenna, as shown in Figure 5.2. In order to emphasis the very large current density near the edges, the three segments are put along the transverse direction of the antenna in the MoM-HB combination method, while the average current by integrating the non-uniform current distribution along the transverse direction is used in the power series method.
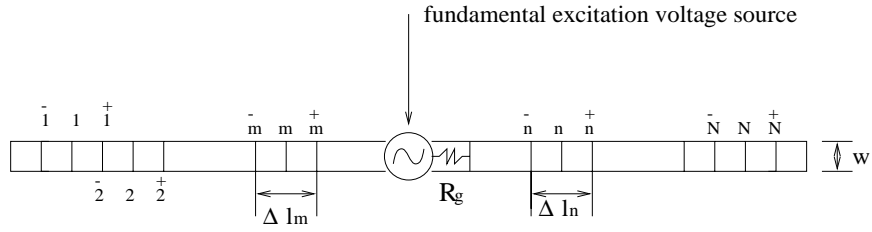
Figure 5.2: Diagram of the center-fed strip dipole antenna circuit with segmentation and excitation

5.3.1   Nonlinear $v - i$ characteristics of HTSC thin films

According to (5.5) the $v - i$ characteristic of a HTSC thin film strip can be derived in the form of a power series as follows:

$$v = a_1 i + a_3 i^3 \tag{5.32}$$

where the coefficients, a_1 and a_3, are expressed in terms of the width, w, and length, Δl, of the strip. From (5.10) they are given as:

$$a_1 = \frac{R_{s0} \Delta l}{w}, \qquad a_3 = \frac{R_{s2} \Delta l}{w^3} \tag{5.33}$$

When $w = 100\mu$m and $l = 2.94$mm, the coefficients for the $YBa_2Cu_3O_{7-x}$ thin films #1 and #2 in [14] are, respectively:

$$\text{Film } \#1: \quad a_1 = 0.00021, \quad a_3 = 0.00067 \tag{5.34}$$

$$\text{Film } \#2: \quad a_1 = 0.00032, \quad a_3 = 0.0022 \tag{5.35}$$

5.3.2 Weak nonlinearity materials

The first example is that the strip dipole antenna is constructed from the HTSC thin film #2 in (3.35) at $T = 77$K and $f = 1.5$GHz. Its width $w = 100\mu$m and thickness $t = 0.8\mu$m. Its $v - i$ characteristic is as follows:

$$v = 0.00032i + 0.0022i^3 \tag{5.36}$$

The results computed by the power series method and the MoM-HB combination method are tabulated in Table 5.1, where each *relative error* between the results obtained by the two methods is defined as follows:

$$Relative\ error = \frac{Result\ by\ PS\ method - Result\ by\ HB\ method}{Result\ by\ PS\ method} \tag{5.37}$$

The relative error defined here is to show the difference between the MoM-HB combination method and the power series method.

When the fundamental input powers to the 72 Ω dipole antenna are 20, 30, 60, 75, and 80 dBm, we use the two methods to compute the current distributions along the dipole antenna at the fundamental and third harmonic frequencies and the radiation power at the third harmonic frequency. The *maximum fundamental current* is the maximum value in the current distribution at the fundamental frequency. The *maximum third harmonic current* is the maximum value in the current distribution at the third harmonic frequency.

In Table 5.1 the fundamental input power, the third harmonic radiation powers, the maximum fundamental currents, and the maximum third harmonic currents obtained by the two methods are given, and comparison is made by calculating the relative errors for these values from the two methods and the *power difference in dB* between the third harmonic radiation and fundamental input are also shown there. Note that the relative error for the third harmonic radiation power is evaluated from values in Watt, not from values in dBm. In reality, it is impossible to have such high input power levels as 60, 75, and 80 dBm in a superconducting microwave circuit, such choice here is only for testing the methods.

5.3.3 Strong nonlinearity materials I

The second example is the same antenna structure except that the $v - i$ characteristic is fictitious and assumed to be highly nonlinear, i.e.,

$$v = 0.00032i + 100i^3 \tag{5.38}$$

Table 5.2 provides the same parameters as those in Table 5.1, but the input powers are 20, 30, and 35 dBm.

It is observed that, for the same input powers in Tables 5.1 and 5.2, i.e., 20 and 30 dBm, the resulted values are different. In Table 5.1, for these two input power levels, the relative error is 0.04% for the third harmonic radiation power and 0.02% for the maximum third harmonic current. Whereas, in Table 5.2, for the input powers of 20 dBm and 30 dBm, the relative error for the third harmonic radiation power is 0.22% and 2.15% respectively, and the relative error for the maximum third harmonic current is 0.13% and 1.41%, respectively. This means that different $v - i$ characteristics result in different nonlinear effects, although the

Table 5.1: Comparison of results by the two methods for the $v - i$ curve: $v = 0.00032i + 0.0022i^3$. The parameters for the strip dipole antenna are: $w = 100\mu$m, $l = 0.094$m. The fundamental excitation frequency $f = 1.5$GHz. (Note: PS— Power series method, HB—MoM-HB combination method)

| Fundamental input | 20 | 30 | 60 | 75 | 80 |
power (dBm)	(0.1 W)	(1 W)	(1000 W)	(316228 W)	(100000 w)
Third harmonic radiation power by PS (dBm)	-135.444	-105.444	-15.444	29.556	44.556
Third harmonic radiation power by HB (dBm)	-135.445	-105.445	-15.447	29.492	44.301
Relative error (%)	0.04	0.04	0.08	1.46	5.71
Maximum fundamental current by PS (A)	0.032911	0.104073	3.2911	18.507	32.911
Maximum fundamental current by HB (A)	0.032909	0.104066	3.2909	18.506	32.909
Relative error (%)	0.006	0.006	0.006	0.006	0.006
Maximum third harmonic current by PS(A)	4.986×10^{-10}	1.577×10^{-8}	4.986×10^{-4}	8.866×10^{-2}	0.4986
Maximum third harmonic current by HB(A)	4.985×10^{-10}	1.576×10^{-8}	4.984×10^{-4}	8.778×10^{-2}	0.4790
Relative error (%)	0.02	0.02	0.05	1.01	3.78
Power difference between the third harmonic radiation and fundamental input(dB)	-155.44	-135.44	-75.44	-45.44	-35.44

Table 5.2: Comparison of results by the two methods for the $v - i$ curve: $v = 0.00032i + 100i^3$. The parameters for the strip dipole antenna are: $w = 100\mu$m, $l = 0.094$m. The fundamental excitation frequency $f = 1.5$GHz. (Note: PS—Power series method, HB—MoM-HB combination method)

Fundamental input power (dBm)	20 (0.1 W)	30 (1 W)	35 (3.16 W)
Third harmonic radiation power by PS (dBm)	-42.44	-12.44	2.56
Third harmonic radiation power by HB (dBm)	-42.45	-12.53	2.15
Relative error (%)	0.22	2.15	8.95
Maximum fundamental current by PS (A)	0.032911	0.104073	0.18507
Maximum fundamental current by HB (A)	0.032909	0.104066	0.18506
Relative error (%)	0.006	0.006	0.006
Maximum third harmonic current by PS(A)	2.228×10^{-5}	7.046×10^{-4}	3.962×10^{-3}
Maximum third harmonic current by HB(A)	2.225×10^{-5}	6.941×10^{-4}	3.717×10^{-3}
Relative error (%)	0.13	1.41	5.97
Power difference between the third harmonic radiation and fundamental input(dB)	-62.44	-42.44	-32.44

input powers are the same. The values for the third harmonic radiation powers, the maximum third harmonic currents and their relative errors in Table 5.1 are less than those in Table 5.2. This is because that (5.36) is weakly nonlinear, while (5.38) is strongly nonlinear. Due of the same coefficient a_1 in (5.36) and (5.38), the maximum fundamental currents in Tables 5.1 and 5.2 are the same.

From the data in Tables 5.1 and 5.2, one can further observe that the relative errors increase as the nonlinear harmonic power increases. If the power difference in dB between the third harmonic radiation and fundamental input is concerned, as shown in the last row in Tables 5.1 and 5.2, one finds that when the power difference is approximately smaller than -45 dB, as shown in Table 5.1 for input powers of 20, 30, 60 and 75 dBm and in Table 5.2 for input power of 20 dBm, the two methods get very close results, for instance, the relative error for the third harmonic radiation power is less than 1.5%, and the relative error for the third harmonic current is less than 1.1%.

In addition, in Table 5.1 for input power of 80 dBm, the power difference is -35.44 dB and the relative errors are not larger than 5.71%; In Table 5.2 for input power of 35 dBm, the power difference is -32.44 dB and the relative errors are not larger than 8.95%. This means that, for power difference smaller than -30 dB, the relative error of the two methods is approximately less than 10%, which is still acceptable for practical applications.

Based on the data in Tables 5.1 and 5.2 and some more computations, we may arbitrarily define here that it is *weakly* nonlinear when the *power difference in dB* between the third harmonic radiation and fundamental input is smaller than -45; otherwise, *strongly* nonlinear.

5.3.4   Strong nonlinearity material II

The third example is for a very strong nonlinear material, whose $v - i$ characteristic of the material is as follows:

$$v = 0.1i + 100i^3 \tag{5.39}$$

Figure 5.3 plots the fundamental current distributions along the dipole obtained by the two methods. Figure 5.4 plots the third harmonic current distributions along the dipole obtained by the two methods. The input power is 30 dBm. In this case, the third harmonic radiation power is computed by the power series method and equal to -13.05 dBm, so the power difference is -43.05 dB, which falls into the above-defined strongly nonlinear range.
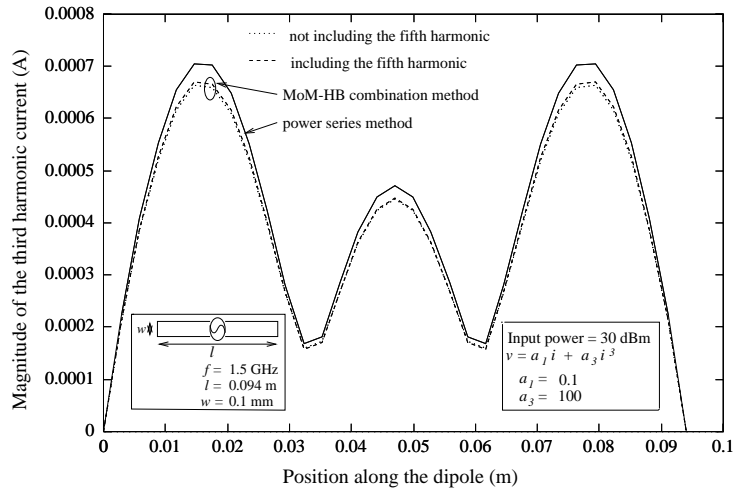
Figure 5.3: Third harmonic current distribution along the nonlinear half-wavelength strip dipole antenna by the two methods when input power is 30 dBm (1 Watt).

From Figures 5.3 and 5.4, one sees that there exists a deviation between the two methods due to the strong nonlinearity. According to (5.32), the larger the
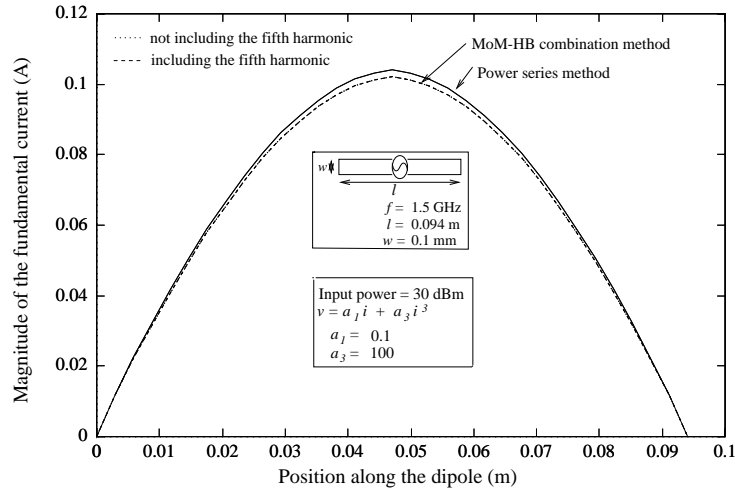
Figure 5.4: Fundamental current distribution along the nonlinear half-wavelength strip dipole antenna by the two methods when input power is 30 dBm (1 Watt).

current values are, the more strong the nonlinear effect. Consequently, the deviation becomes more apparent at those points where the current values are larger.

It is observed in Figures 5.3 and 5.4 that the current distribution obtained by the MoM-HB combination method is lower than that by the power series method. This is expected, since all harmonics are considered simultaneously in the MoM-HB combination method, and a fraction of power is shifted to the higher order harmonic frequencies.

In the MoM-HB combination method, it is expected that the more harmonics are included, the more accurate the results are, so the third harmonic current distribution including the effect of the fifth harmonic is also plotted in Figure 5.4. One finds that the curve is a little bit close to the curve obtained by the power series method.

The relative error for each segment current in the dipole antenna is evaluated

and plotted in Figure 5.5, in the case of including the fifth harmonic and not including the fifth harmonic. It is found that the maximum relative error is not larger than 6.3% for the third harmonic current.

As compared the relative error for the case of including the fifth harmonic with the relative error for the case of not including the fifth harmonic, the values in the former case is less than the values in the latter case, expect for those points with the smaller current values.
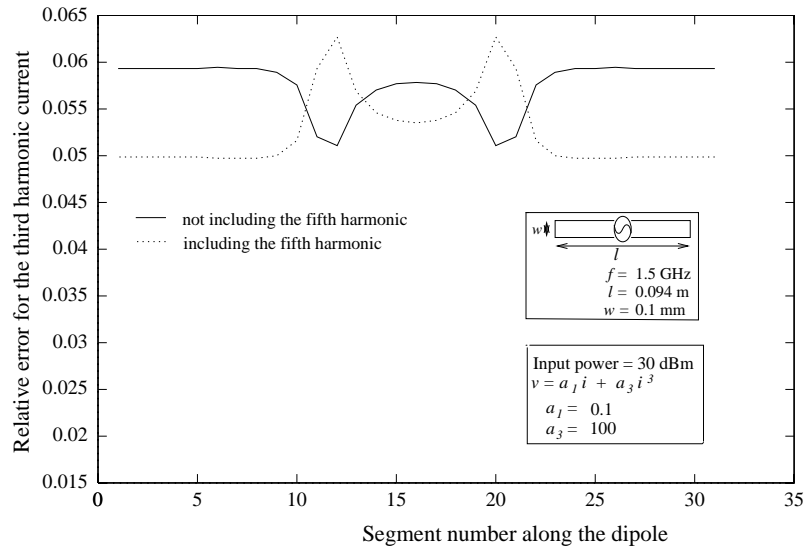
Figure 5.5: Relative error between the power series method and the MoM-HB combination method for the third harmonic currents when input power is 30 dBm

In the MoM-HB combination method the convergence is very fast. When $eps < 10^{-6}$, starting even with an arbitrary initial guess, 4 to 6 iterations are required to converge, with $K = 5$ (It means that the fundamental, third and fifth harmonic frequency are included). The contribution of higher order harmonics up to $K = 9$ (including even order harmonics) are studied. For weak nonlinearity the obtained

results are indistinguishable from the those obtained with $K = 5$.

5.4 Range of validity and advantage of the power series method

The MoM-HB combination method is based on the harmonic balance technique. It is known that the harmonic balance technique is suitable for both weak and strong nonlinearities [19]. According to the above comparison between the two methods, the power series method works very well for the weak nonlinearity, i.e. the power difference in dB is smaller than -45; and it still works for not very strong nonlinearity, i.e. the power difference in dB is smaller than -30. Therefore, the range of validity of the proposed power series method is for the weak nonlinearity, i.e., power difference in dB between the harmonic radiation(output) and fundamental input is smaller than -45, and for the slightly strong nonlinearity with power difference smaller than -30 dB.

If we say that the range of validity of the proposed power series method is that the power difference is smaller than -30 dB, then in the above range the power series method has obtained the results close to those by the harmonic balance method, and very close especially for the weak nonlinearity. Therefore, the power series method is validated.

According to the numerical results presented for the harmonic generation, the power series method is in a good agreement with the MoM-HB combination method, especially for weak nonlinearity. Thus, it is justified that the power series method can be used to analyze the two-tone intermodulation as well.

Based on above results and discussions, the nonlinearity in the superconducting

circuits is usually weak. In addition, the nature of the magnitude distribution of harmonic components is that higher harmonic component has smaller magnitude. Therefore the power series method can be used to analyze the nonlinear effects in the superconducting microwave circuits.

Moreover, the computation speed of the power series method is much *faster* than that of the MoM-HB combination method. Since all harmonics have to be handled simultaneously in the MoM-HB combination method, the size of the impedance matrix $[Z]$ grows very large as compared to the power series method. This results in relatively slow computation. The reason is that a harmonic balance equation is usually solved through an iterative procedure and in every iteration one have to evaluate the inverse of $[Z]$, as shown in Figure 4.2 in Chapter 4. However, in the power series method, because one does not need to solve the nonlinear integral equation directly and in every step only the desired harmonic component needs to be considered, the size of the impedance matrix keeps unchanged. No iteration is needed in the power series method as well. Therefore the proposed power series method offers faster computation.

5.5 Identify the 'type' of HTSC nonlinearity

In practical situation, say satellite communications, the input power level in the receiving mode for superconductive microwave circuits is less than 30 dBm, and not larger than 60 dBm even in the transmitting mode. In a duplex system the power level of transmitting is at most 60 dB above that of receiving. Based on the numerical results in Section 5.3 and the coefficients, a_1 and a_3, in (5.34) and (5.35), the power difference in dB between the third harmonic radiation(output) and fundamental input is usually much smaller than -45 in the practical operating

range. Therefore, we can say that the nonlinear dependence of the surface resistance on the applied RF magnetic field is *weak*.

5.6 Conclusions

In this chapter we have explained another proposed method—power series method. In this method the self terms in the impedance matrix, which has been developed in the linear solver in the MoM-HB combination method, contained the contribution from the surface impedance of the conducting material. The resultant matrix was solved for the current distribution at the fundamental frequency. The voltages across current segments over the conducting surface were found at higher order harmonic frequencies from the fundamental current distribution. The higher order harmonic voltages were treated as the excitation at the corresponding frequency. The current distributions at higher order frequencies were evaluated by applying the moment method again. For the non-uniform current distribution along the transverse direction, the average current was obtained by taking the integral of the current distribution over the width.

The two proposed methods were used to investigate the nonlinear half-wavelength strip dipole antenna circuit. A thorough comparisons of the results obtained from the two method were made to show the agreement between them. We did the comparisons for a typical HTSC material and two strongly nonlinear materials. Based on the results obtained, it was concluded that the HTSC material is weakly nonlinear. The two methods were in excellent agreement for weak nonlinearities, and the agreement for slightly strong nonlinearities was still good.

The power series method was simple for finding the output power at higher order frequencies. According to the results obtained, the power series was suitable

for weak nonlinearities. Also the power series method was faster than the MoM-
HB combination method, since the matrix equation was solved separately at each
frequency and no iteration was involved. We tested the convergence and contribu-
tions from higher order harmonic frequencies (including even order harmonics) in
the MoM-HB combination method. The method converged very fast. It was safe
to exclude the even order harmonics and to neglect the odd order harmonics higher
than the fifth harmonic for analysis of HTSC nonlinearity.

Chapter 6

HTSC microstrip lines

6.1 Introduction

In this chapter we study the effects of HTSC nonlinearity on a microstrip line, where the conducting material is made of HTSC material. The analysis performed in this chapter has two purposes: First, further validating the two proposed nonlinear modeling methods for the analysis of nonlinear behaviors of HTSC thin film circuits. Second, studying the nonlinear behaviors of HTSC microstrip line, such as current distribution and conductor loss, when the applied power becomes high.

A microstrip line is by far the most commonly used form for HTSC transmission lines, principally due to the case with which it lends itself to the photolithographic fabrication technology predominant in the present time. It is a very basic building element in microwave integrated circuits(MICs). It has been extensively used for constructing HTSC components, such as resonators and filters, and providing interconnection in HTSC circuits. A one-dimensional transmission line is a section of transmission line with some coupling mechanism connected to the input and out-

84

put. At microwave frequency, usually, the loss of a transmission line is dominated by the conductor loss. That is why the use of HTSC materials can make a big difference.

Unlike the normal metals, however, the HTSC materials show nonlinear effects even at moderate power levels. Nonlinear effects result in increasing the surface resistance, R_s, value and the RF loss significantly, which reduces the Q value.

The organization of this chapter is as follows: In Section 6.2 the effective surface impedances of HTSC thin films are derived in order to take into consideration the influence of the stacked elements, such as the dielectric substrate and the ground plane, supporting the superconducting films. In Section 6.3 the consideration in the segmentation of the microstrip line is explained when the moment method is applied. In Section 6.4 some numerical results for current distribution and conductor loss are presented and comparison with published results and related discussions are also provided. Section 6.5 concludes this chapter.

6.2   Effective surface impedances

The effective surface impedance of conductors is a crucial parameter for implementing planar microwave devices. In some structures, large differences between the effective surface impedances and the intrinsic values are caused by utilizing films with thicknesses comparable or smaller than the electromagnetic wave penetration depth. A systematic theoretical investigation about the discrepancy between the two values (effective and intrinsic) of the film surface impedance has been conducted in [43] for HTSC materials $YBa_2Cu_3O_7$(YBCO) epitaxially grown on various crystalline substrates (MgO or $LaAlO_3$ or $SrTiO_3$). The calculations are based on the two-fluid model of superconductors and the standard transmission line theory. The

reported theoretical results demonstrate that the effective surface impedance of YBCO films with a thickness smaller than 500 nm can be very different from the intrinsic film impedance according to the configuration. The predicted device characteristics or the intrinsic surface impedance deduced from experimental data may be quite erroneous by only taking the superconducting film thickness into account. The influence of the stacked elements supporting the superconducting films must be considered according to the arrangement.

By introducing superconducting films in passive microwave devices, reductions of insertion losses are expected from the low intrinsic surface resistance of superconductors. However, the devices must be appropriately designed to benefit by this potential advantage. That is crucial in devices made of very thin superconducting films to exploit the kinetic inductance effect. Moreover, the determination of the intrinsic surface impedance of thin films requires a correction of experimental data depending on the measurement arrangement.

In this section the effective surface impedance of HTSC films is derived based on the two-fluid model and the conventional transmission line theory to include the effects of thicknesses of the HTSC film, the substrate, and the ground plane in order to achieve the generalization of the analysis.

As shown in Figure 6.1, a HTSC thin film with a thickness t is supported by a dielectric substrate with finite thickness of h, and the substrate backside is in contact with bulk metal or bulk superconductor known as the ground plane. An electromagnetic plane wave is supposed to impinge on planar stacks of super or normal conducting materials and dielectric substrates with an incidence direction perpendicular to the vacuum-stack interface, and the lateral dimensions being sufficient to avoid the diffraction effect. Therefore, the electromagnetic wave propagating in substrate is the sum of the wave along the incident wave direction and the reflected
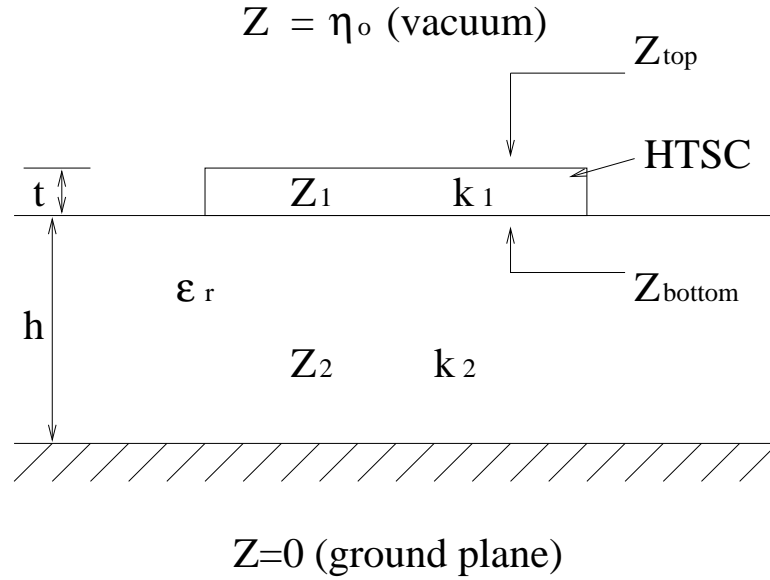
Figure 6.1: Diagram of Z_{top} and Z_{bottom} in a HTSC microstrip line

wave due to the ground plane.

The wave impedance of the lossless dielectric substrate is:

$$Z_2 = \frac{\eta_0}{\sqrt{\epsilon_r}} \tag{6.1}$$

where ϵ_r is the real relative permittivity of the substrate and η_0 is the vacuum impedance (377Ω). The propagation constant in the substrate is:

$$k_2 = \omega\sqrt{\mu_0\epsilon_0\epsilon_r} \tag{6.2}$$

The propagation constant in the superconducting material, k_1, is a function of complex conductivity σ in (2.23), which is copied here:

$$\sigma = \sigma_n + \sigma_{sc} \quad \text{with} \quad \sigma_n = \frac{1}{\rho_n} \quad \text{and} \quad \sigma_{sc} = \frac{-j}{\mu_0\omega[\lambda_L^2(T)]} \tag{6.3}$$

where ρ_n is the normal resistivity at the operating temperature, and $\lambda_L(T)$ is the magnetic field penetration depth at temperature T. Then k_1 can be determined as:

$$k_1 = k_1' + jk_1'' = [j\mu_0\omega(\sigma_n + \sigma_{sc})]^{1/2} = \frac{1}{2}\omega\mu_0\lambda_L(T)\frac{1}{\rho_n} - j\frac{1}{\lambda_L(T)} \qquad (6.4)$$

The complex wave impedance of the HTSC thin film is denoted by Z_1. The intrinsic surface impedance Z_s of the superconducting film is:

$$Z_{s,ins} = R_{s,ins} + jX_{s,ins} = \frac{Z_1}{\tanh(jk_1t)} \qquad (6.5)$$

which is the effective impedance when the dielectric substrate with a thickness of a quarter-wavelength is laid on a bulk material with a very low impedance (metals or superconductors). Thus, from (6.5)

$$Z_1 = Z_{s,ins}\tanh(jk_1t). \qquad (6.6)$$

where t is the thickness of HTSC thin film. At microwave frequency, when t is several times larger than $\lambda_L(T)$, $\tanh(jk_1t) \approx 1$. Thus $Z_1 = Z_{s,ins}$.

According to the transmission line theory, the input impedance of a transmission line is

$$Z_{in} = Z_0\frac{Z_L + Z_0\tanh(jkl)}{Z_0 + Z_L\tanh(jkl)}, \qquad (6.7)$$

where Z_0 is the characteristic impedance of the transmission line, Z_L is the load, k is the propagation constant, and l is the length of the transmission line. Based on (6.7) the effective surface impedance at the top and bottom surfaces of the HTSC film in Figure 6.1 can then be derived.

6.2.1   Effective surface impedance at the top surface

In order to find the effective surface impedance seen into the top surface of the HTSC thin film, Z_{top}, according to the transmission line theory, the substrate and

the ground plane are considered as the load of the HTSC film. The wave impedance of the bulk metal can be considered as null. Using (6.7) we can find the load impedance:

$$Z_L = Z_2 \tanh(jk_2h) = jZ_2 \tan(k_2h) \tag{6.8}$$

In this case we have:

$$Z_0 = Z_1 \tag{6.9}$$

and

$$k = k_1 \tag{6.10}$$

By substituting (6.8)-(6.10) into (6.7), we obtain the effective surface impedance seen into the top surface of the HTSC film:

$$Z_{top} = Z_1 \frac{Z_2 \tanh(jk_2h) + Z_1 \tanh(jk_1t)}{Z_1 + Z_2 \tanh(jk_2h) \tanh(jk_1t)} \tag{6.11}$$

Let us check (6.11) by considering the extreme case that $t \gg \lambda_L(T)$. At microwave frequency, when t is several times larger than $\lambda_L(T)$, $\tanh(jk_1t) \approx 1$. Therefore, from (6.11) $Z_{top} = Z_1 = Z_{s,ins}$, which is the surface impedance of infinitely thick superconductor as it should be.

6.2.2 Effective surface impedance at the bottom surface

Similar to the previous case, in order to find the effective surface impedance seen into the bottom surface of the HTSC thin film, Z_{bottom}, the vacuum in the half space above the HTSC film is considered as a load. Since the half space is infinite in the direction away from the HTSC film, the load is considered as a matched load, that is,

$$Z_L = \eta_0 = 377\Omega \tag{6.12}$$

We also know that:

$$Z_0 = Z_1 \tag{6.13}$$

and

$$k = k_1 \tag{6.14}$$

By substituting (6.12)-(6.14) into (6.7), we obtain the effective surface impedance seen into the bottom surface of the HTSC film:

$$Z_{bottom} = Z_1 \frac{\eta_0 + Z_1 \tanh(jk_1 t)}{Z_1 + \eta_0 \tanh(jk_1 t)}. \tag{6.15}$$

Again, consider the extreme case that $t \gg \lambda_L(T)$. At microwave frequency, when t is several times larger than $\lambda_L(T)$, $\tanh(jk_1 t) \approx 1$. Therefore, from (6.15) $Z_{bottom} = Z_1 = Z_{s,ins}$, as it should be.

6.3 Segmentation consideration

6.3.1 Edge behaviors of current distribution

It is well known that the current distribution over the cross section of a strip has edge behaviors [44] [41] [35]. We have plotted the edge behaviors of the current distribution across a strip in Figure 5.1 in Chapter 5.

The current distribution on the surface and inside the HTSC strip has been studied in [44]. By using the method developed in that paper, we calculate the distribution of the axial current density component, $J_z(x, y)$, over the cross section of thick and thin superconductor films, and the results are plotted in Figures 6.2 and 6.3. The total current flowing through the microstrip in both cases is 1mA. The superconductor material is $YBa_2Cu_3O_{7-x}$, whose penetration depth $\lambda_L(T) = 0.3\mu m$
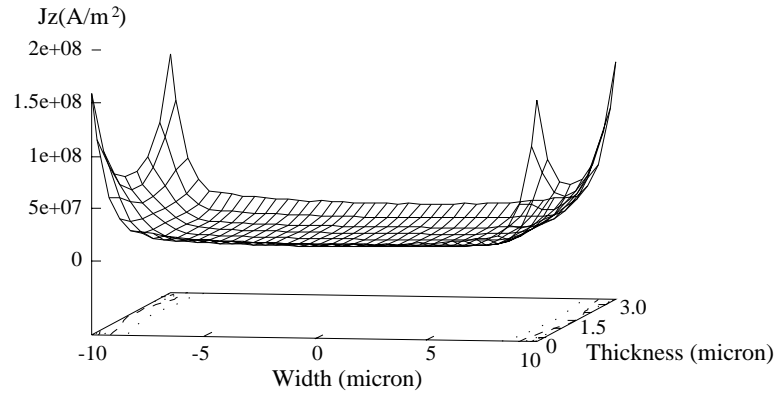
Figure 6.2: The J_z distribution of a thick superconducting film: $w = 20\mu$m, $t = 3\mu$m, $h = 200\mu$m, $f = 1.5$GHz, $\lambda_L = 0.3\mu$m.
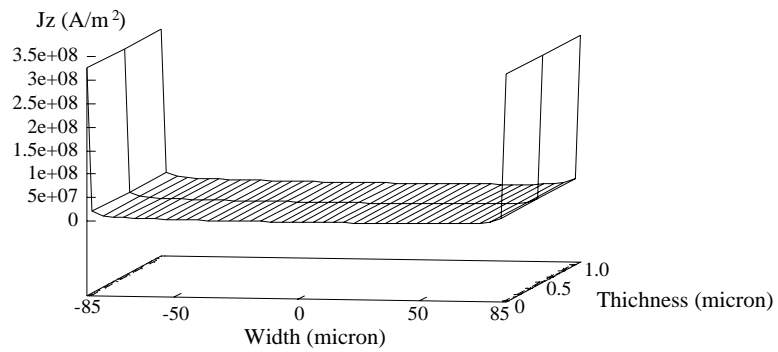
Figure 6.3: The J_z distribution of a thin superconducting film: $w = 170\mu$m, $t = 1\mu$m, $h = 200\mu$m, $f = 1.5$GHz, $\lambda_L = 0.3\mu$m.

at $T = 77$K. It is observed from Figures 6.2 and 6.3 that the current is highly non-uniform—peaks at the edges. It is also observed that the current distribution is non-uniform not only along the line width direction but also along the line thickness direction.

6.3.2 Thickness effect of the strip

As described in section 6.2, when the thickness of the strip is comparable with respect to, or several times of, the penetration depth for superconductor or the skin depth for normal conductor, the effect of the strip thickness, the substrate, and the ground plane can not be neglected. Therefore, to simulate a HTSC microstrip line accurately and generalize the analysis, the thickness of superconductive strip conductor is taken into consideration.

As a consequence, as shown in Figure 6.4, the four surfaces of the HTSC strip (i.e., top, bottom, left and right surfaces) are all segmented, and much finer grids are put over the regions near the edges to emphasize the rapid variation in the current densities near the edges. These high edge current densities could drive HTSC material into strong nonlinear behavior and may eventually exceed its critical current density easily, whereas the current densities over the other parts of the surface remain at a low level.

6.4 Numerical results

In this section the two proposed methods—the MoM-HB combination method and the power series method—are used to analyze HTSC microstrip line. The current
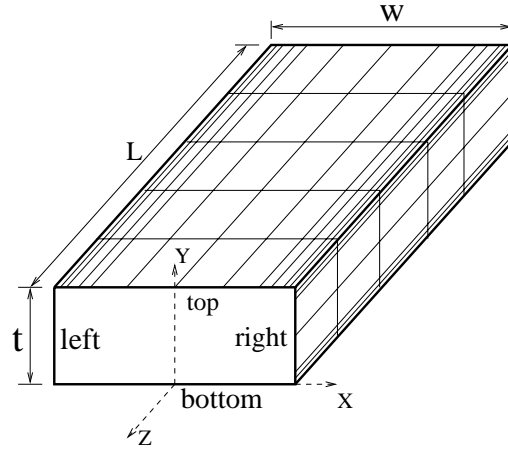
Figure 6.4: Diagram of a HTSC thin film with non-uniform gridding near the edges

distribution over the cross section of the HTSC stripline for different input power levels and the HTSC conductor loss as a function of input power are evaluated [39].

The coefficients of the power series for the nonlinearity of HTSC material are the same as those in (4.20) and copied here:

$$R_{s0} = 1.4868 \times 10^{-5}\,\Omega, \qquad R_{s2} = 4.8270 \times 10^{-9}\,\Omega/Oe^2 \qquad (6.16)$$

6.4.1 Current density distribution

First example

The first example is a microstrip line structure that has been simulated in [23]. The strip has a width of $w = 7.5\mu$m, a thickness of $t = 1\mu$m and a length of $L = 6$ mm. When $T = 77$ K, the penetration depth is 0.323 μm. The substrate thickness $h = 10\mu$m with the relative dielectric constant of 13. The operating frequency is 10 GHz. We have calculated the current distributions on the top and bottom surfaces

of the conducting strip for the applied power of -10 dBm and 5 dBm.

When the applied power is -10 dBm, the current distribution is plotted in Figure 6.5. It is found that there are high current density peaks at the edges. This is because the applied power is small. However, when the applied power is increased to 5 dBm, the peaks of the current density distribution shift away from the edges towards the central part of the HTSC strip, as shown in Figure 6.6.
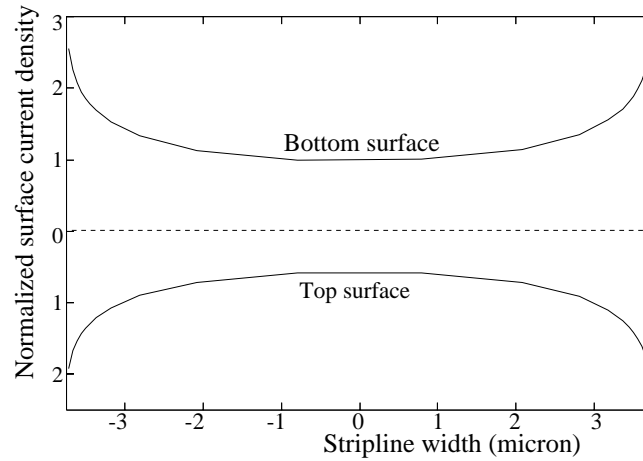
Figure 6.5: Surface current density distributions normalized to the center of the bottom surface on the bottom and top surfaces of a finite-thickness HTSC microstrip line at -10 dBm applied power

That is, for the superconductor with high applied power, the current density is relatively flat in the center part of the strip. When it approaches the edges of the strip, it increases very rapidly. But, after the current density reaches a maximum value, it drops sharply at the edges. From a close examination it is found the attenuation in the low power range is mainly determined by R_{s0}, whereas the attenuation in the high power range is mainly determined by R_{s2}.
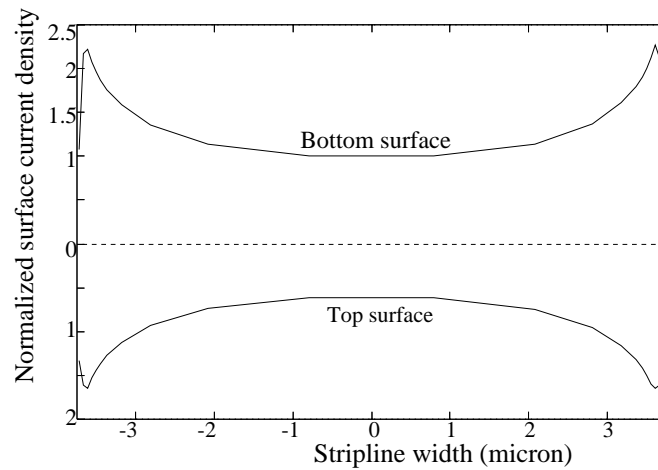
Figure 6.6: Surface current density distributions normalized to the center of the bottom surface on the bottom and top surfaces of a finite-thickness HTSC microstrip line at 5 dBm applied power
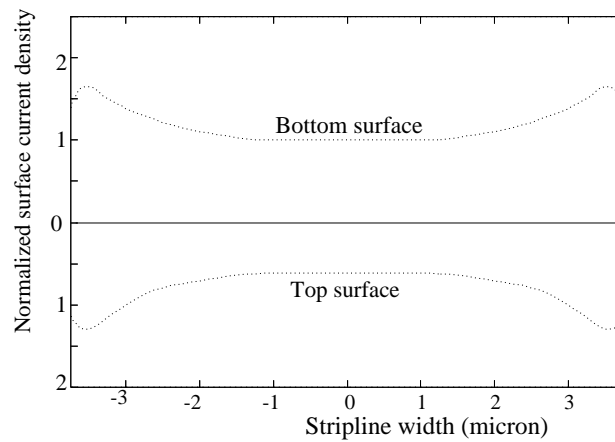
Figure 6.7: Surface current density distributions normalized to the center of the bottom surface on the bottom and top surfaces of a finite-thickness HTSC microstrip line from [23]

It is well known that there are always the current singularity at edges for perfect conductor no matter how high the applied power is, because the material is linear [37]. However, this is no longer true in the case of HTSC materials. Through a careful examination to the surface impedance of HTSC material, it is evident that the resistance will become very large near the edges due to very large edge current densities. That in turn causes the decrease in the edge current densities. That is, the redistribution of the current density occurs with the high applied power.

Shown in Figure 6.7 are the numerical results for the current distribution from [23] for the same microstrip line obtained by a 2-D model and FDTD approach in conjunction with GL theory. Compared the results in Figure 6.6 with those in Figure 6.7, it is observed that the general trend for the current distribution over the stripline width as predicted by the two approaches is very close, especially in the central part of the stripline.

However, what we should emphasize here is the difference between these two approaches. Our method is basically the integral equation approach. Therefore, it is substantially faster than the differential equation FDTD-based approach.

Second example

The second example is a typical 50 Ω HTSC microstrip line. The line has a width of $w = 0.17$ mm, a thickness of $t = 0.6$ μm, and a length of $L = 6$ mm. When $T = 77$ K, the penetration depth is 0.323 μm. The substrate thickness $h = 0.508$ mm with $\epsilon_r = 24$. The current distributions at different power levels are calculated. The top and bottom surface current density distributions normalized to the center of the bottom surface is shown in Figure 6.8, and the actual values of current density are given in Figure 6.9. These figures shows very clearly how the
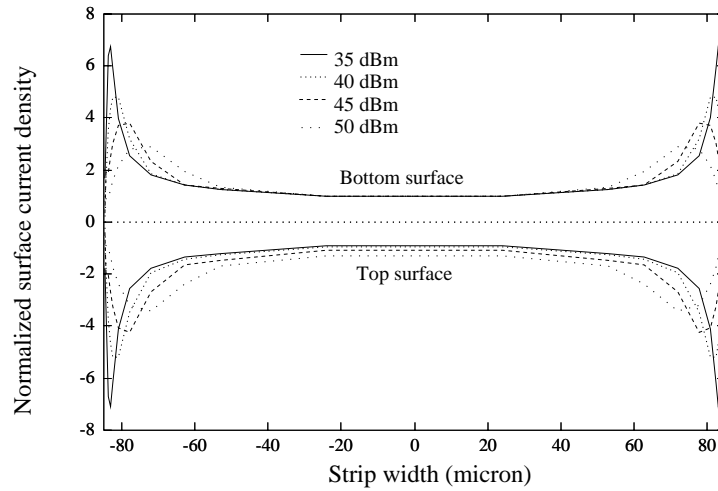
Figure 6.8: Surface current density distributions normalized to the center of the bottom surface on the bottom and top surfaces of a finite-thickness HTSC microstrip line with $Z_0 = 50\Omega$
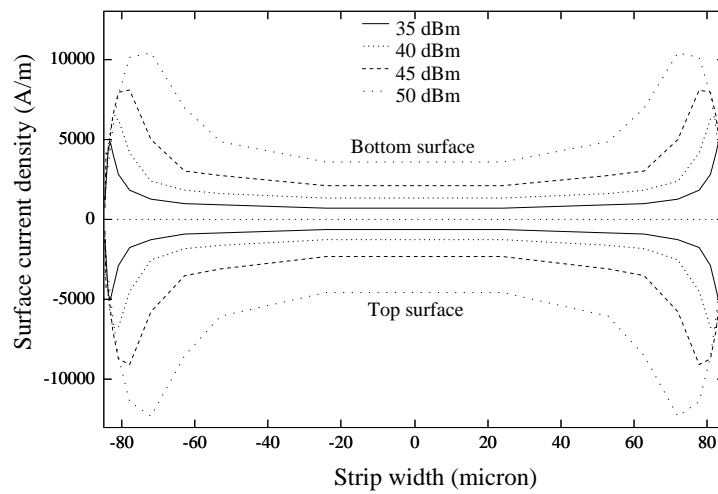
Figure 6.9: Surface current density distributions on the bottom and top surfaces of a finite-thickness HTSC microstrip line with $Z_0 = 50\Omega$

peaks shift away from the edges as the input power increases.

It should be pointed out that the current density redistribution, i.e., the shift of the current density peaks away from the edges, may not be observed in practical experiments. This is due to the thermal runaway. When the loss of HTSC material is high at high power, a lot of heat will be generated. The heat in turn results in the higher loss. Then the loss generates more heat. For HTSC microwave circuits that is operating at high power, the heat generated inside the circuits may be high enough to drive the HTSC material out of the superconductive state before the superconductivity disappears due to the current density larger than HTSC critical current density.

6.4.2   HTSC conductor loss

Once the current at different harmonic frequency is obtained from the above analysis on each segment over a HTSC microstrip line, the effective series resistance [per unit length] as a function of input power, P, is determined from the surface resistance, and expressed as follows:

$$R_{eff}(P) = \frac{\int R_s(|J_z|)|J_z|^2 dx}{|\int J_z dx|^2} \quad (\Omega/m) \tag{6.17}$$

where J_z is the total longitudinal current and the integral is carried out along the contour of the cross section of the stripline. Then the conductor loss for HTSC microstrip line can be evaluated by the following formula:

$$\alpha(P) = \frac{R_{eff}(P)}{2Z_0} \quad (NP/m) \tag{6.18}$$

where Z_0 is the characteristic impedance of the microstrip line. Note here that R_{eff} is a function of the input power, so is α.

For the strip in the first example in the previous subsection, the conductor loss as a function of input powers at the operating frequency of 10 GHz is shown in Figure 6.10, and the results based on the linear model and for a normal conductor, copper, are also presented in the figure for comparison. It is observed that, below the power level of -35 dBm, the attenuation constant not only is very small but stays constant as well. This is why HTSC is very attractive for many low loss applications. However, when the input power increases, the attenuation starts going up very rapidly.

¿From Figure 6.10 the attenuation based on the linear model keeps constant over the entire input power range, so it fails to predict the conductor loss of the HTSC beyond -35 dBm power level. The conductor loss for the normal conductor, copper, is three orders of magnitude higher than that for HTSC material, and also remains constant no matter how high is the applied power [37].

Figure 6.11 gives the conductor loss as a function of input power for the strip in the second example in the previous subsection. Since the strip width in this example is larger than the strip width in the first example, the conductor loss in this example starts going up after the input power exceeds -10 dBm. This gives another evidence that a wider strip are capable of handling more power than a narrower strip. When the input power reaches around 25 dBm, the HTSC conductor loss are comparable with the gold conductor loss.

By a close examination to the surface impedance of HTSC material, it is also found the attenuation at the low power region is mainly determined by the linear coefficient R_{s0}, whereas the attenuation at the high power region is mainly determined by the nonlinear coefficient R_{s2}.

According to the results obtained above for the conductor loss of HTSC mi-
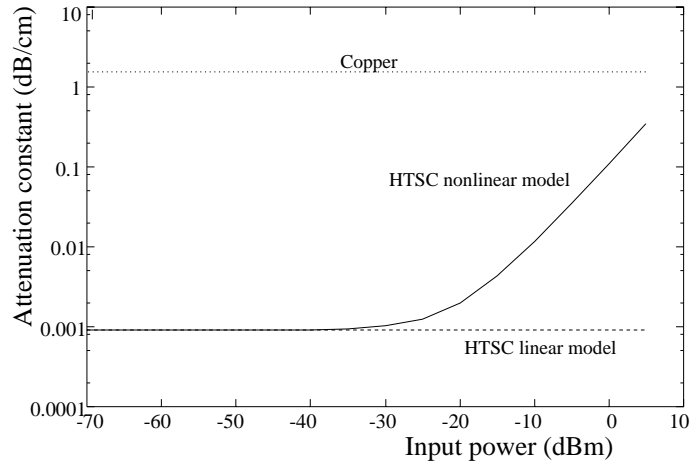
Figure 6.10: Attenuation constant vs. input power of a microstrip line in [18] at $f = 10$ GHz, whose dimension is: $w = 7.5\mu$m, $t = 1\mu$m, $\lambda_L = 0.323\mu$m at $T = 77$K, $h = 10\mu$m, and $\epsilon_r = 13$.
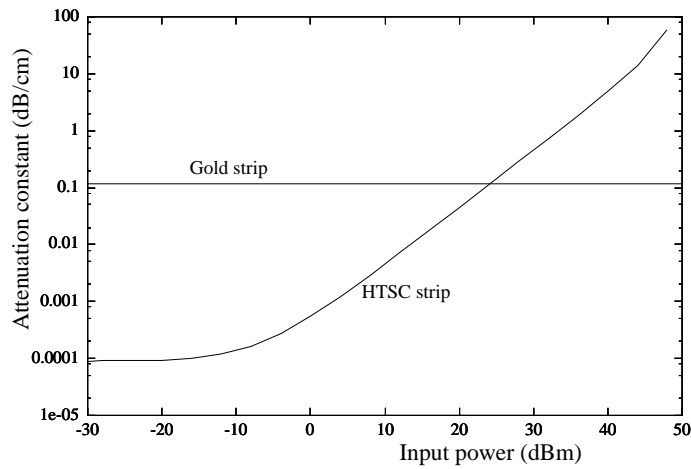
Figure 6.11: Attenuation constant vs. input power of a microstrip line with $Z_0 = 50\Omega$ at $f = 4$ GHz, whose dimension is: $w = 0.17$mm, $t = 0.6\mu$m, $\lambda_L = 0.323\mu$m at $T = 77$K, $h = 0.508$mm, and $\epsilon_r = 24$.

crostrip lines, it is observed that the common behavior is that the HTSC conductor loss increases quickly and becomes much larger than the gold conductor loss, after the input power exceeds a certain value. Therefore, we can conclude that at high power an interconnecting HTSC microstrip line behaves as an attenuator.

6.5   Conclusions

In this chapter microstrip lines constructed from HTSC materials have been investigated for the nonlinear effects of HTSC materials on the current density distribution over the cross section of the stripline and the conductor loss of HTSC material as a function of the applied power. We have considered the thickness of the HTSC conductor in order to simulate a HTSC microstrip line accurately. Moreover, the effective surface impedances have been considered. We have also put much finer grids over the regions near the edges to emphasize the rapid variation in the current densities near the edges.

The current distributions have been calculated at different input power levels. When the applied power is small, there are high current density peaks at the edges. However, when the applied power increases, the peaks of the current density distribution shift away from the edges towards the central part of the HTSC strip. That is, due to the nonlinearity of HTSC material, higher input power causes the current to re-distribution. Comparisons with the published numerical results for the current distribution for a similar microstrip line obtained by a 2-D model and FDTD approach in conjunction with GL theory have been made, and it is observed that the general trend for the current distributions over the stripline width as predicted by the two approaches is very close, especially in the central part of the stripline. The conductor loss as a function of input powers has been also obtained

and compared with the results from the linear model and for normal conductors, copper and gold. It is observed that, below a certain power level, the attenuation constant not only is very small but stays constant as well. However, the attenuation starts to increase very rapidly with the input power. The linear model fails to predict the HTSC conductor loss beyond that power level. It is concluded that an interconnecting HTSC microstrip lines behaves like an attenuator at high power.

Chapter 7

HTSC microstrip patch filters

7.1   Introduction

In this chapter two 2-D HTSC microstrip patch filters are investigated. One is a square patch filter, which is a single-mode filter. The other is a corner-cut patch filter, which is a dual-mode filter [5]. The two proposed methods, i.e., the MoM-HB combination method and the power series method, are used to analyze the effects of the nonlinearity of HTSC material on the circuit behaviors, such as harmonic generation, insertion loss, and reflection coefficient. One purpose is to show the validity of the linear solver for 2-D patch filter. The other purpose is to demonstrate that the total loss of the HTSC patch filter circuit could be dominated by the loss in the HTSC microstrip interconnecting line, especially when the filter is operating at high power.

The organization of this chapter is as follows: In Section 7.2 the loss in microstrip patch filter circuits is discussed to gain an understanding of the relation among those quantities, such as the loaded Q value, the dimensions of the patch and

the interconnecting line, and the average current densities on the patch and line. In Section 7.3 the linear solver is used to find the scattering parameters and the current distribution over the patch in the patch filters. In Section 7.4 the nonlinear effects of HTSC material on the scattering parameters are studied at high power in the case that the interconnecting line is made of HTSC material. In Section 7.5 the analysis of the same nonlinear effects is carried out, but in the case that the interconnecting line is made of gold. In section 7.6 the output powers at the third harmonic are evaluated for both HTSC and gold interconnecting lines. Finally, Section 7.7 concludes this chapter.

7.2 Loss in microstrip patch filter circuits

A microstrip patch resonator is a building block for 2-D microstrip filters and usually used to achieve high Q value. If the patch is constructed from HTSC material, extremely high Q value can be achieved. This is because of the surface resistance orders of magnitude lower than that of conventional conductors at microwave frequency. That allows significant improvement in the filter performance. However, for a HTSC microstrip patch filter the total loss could be dominated by the loss in the HTSC microstrip lines connecting the patch resonator to the input and output terminals. Therefore, the filter must be carefully designed in order to take advantage of the benefit of HTSC material.

For a microstrip patch filter at resonance the total current flowing through the patch is equal to the total current flowing through the interconnecting microstrip line multiplied by the loaded Q value of the circuit at resonance. That is,

$$I_{patch} = Q_{loaded} \times I_{strip} \tag{7.1}$$

where the total current is the product of the average current density and the width. Then the ratio of the average current density over the patch $J_{ave,patch}$ to the average current density over the microstrip line $J_{ave,strip}$ is:

$$\frac{J_{ave,patch}}{J_{ave,strip}} = Q_{loaded} \times \frac{W_{strip}}{W_{patch}}, \tag{7.2}$$

where W_{strip} and W_{patch} are the width of the patch and the microstrip line, respectively. So, $\frac{J_{ave,patch}}{J_{ave,strip}}$ depends on the geometry and the loaded Q of the resonator.

It is well known that, if the average current density is high, the loss (including ohmic and harmonic losses) of the circuit is high, i.e., the transmission coefficient S_{21} becomes low. According to (7.2), if

$$Q_{loaded} < \frac{W_{patch}}{W_{strip}}, \tag{7.3}$$

then

$$\frac{J_{ave,patch}}{J_{ave,strip}} < 1, \tag{7.4}$$

in this case, the loss in the microstrip line is higher than the loss in the patch.

The current density over a microstrip line is highly non-uniform, particularly, the current densities over the regions around its two edges are extremely high as compared with the rest region of the line. HTSC microstrip lines have been investigated in Chapter 6. We have learnt that, due to the nonlinear surface impedance of HTSC material, the conductor loss of HTSC microstrip increases significantly as the applied power increases. Thus, an interconnecting HTSC microstrip line may be considered to be an attenuator. However, the loss in a non-HTSC microstrip line, such as gold, does not change with the applied power. A HTSC microstrip patch filter circuit needs a couple of transmission lines to connect itself to the source and the load or external circuits. Therefore, the circuit behaviors will change due to the transmission lines made of different materials.

7.3   Linear solver

The linear solver in the MoM-HB combination method is used to do linear analysis first in this section to show that it is valid for 2-D patch filter. The scattering parameters, S_{11} and S_{21}, and current distribution over the conducting surface are calculated.

A HTSC single-mode square patch filter is shown in Figure 7.1. The dimension of the patch resonator is 5×5 mm^2. The substrate is 0.508 mm in thickness with the relative dielectric constant $\epsilon_r = 24$. The interconnecting microstrip line is 0.17 mm in width and $\lambda/10$ in length, so that the characteristic impedance of the interconnecting line is about 50 Ω. The source resistance is also 50 Ω.
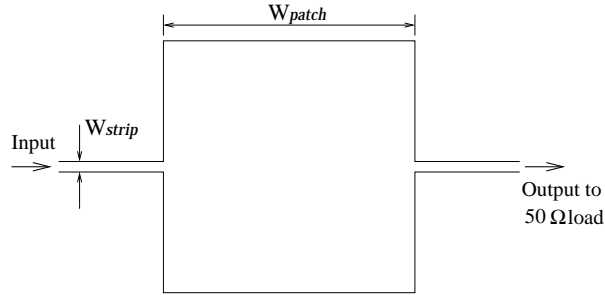
Figure 7.1: Diagram of a square microstrip patch filter: $W_{patch} = 5$mm, $\epsilon_r = 24$, $h = 0.508$mm, and $W_{strip} = 0.17$mm.

A HTSC square microstrip patch resonator with a cut corner is shown in Figure 7.2. The dimension of the patch resonator is equal to half a wavelength at resonance. The length of the interconnecting microstrip line is $\lambda/10$. The substrate, the width of the interconnecting line, and source resistance are the same as that in Figure 7.1. This patch is a dual-mode resonator, because the corner cut causes two orthogonal modes to couple to each other.
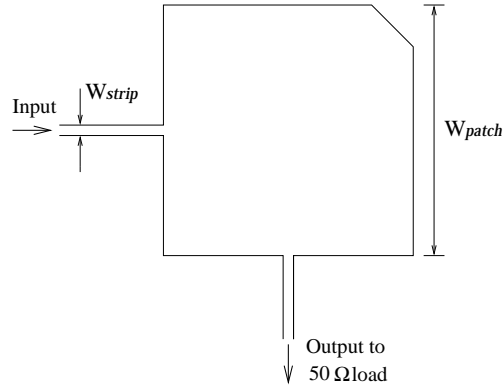
Figure 7.2: Diagram of a microstrip patch filter with a cut corner: W_{patch} is half a wavelength at resonance, $\epsilon_r = 24$, $h = 0.508$mm, and $W_{strip} = 0.17$mm.

For the square resonator, there are two degenerated modes, TM_{01} and TM_{10}, sharing the same resonant frequency. If the square configuration is perfect without the cur corner, these two modes are orthogonal. In other word, there is no coupling between these two modes. The corner cut introduces the coupling. The coupling coefficient can be adjusted by changing the size and the shape of the cut. The cut corner will also change the resonant frequency from the original one without the cut. However, if the cut has a 90-deg edge with respect to the diagonal of the square that is symmetrical to both modes, the resonant frequency of these two modes remains the same. But, of course, it is different from the one without the cut.

7.3.1   Scattering parameters

The magnitude and phase of the scattering parameters as a function of frequency for the square patch filter are shown in Figures 7.3 and 7.4, respectively. The results
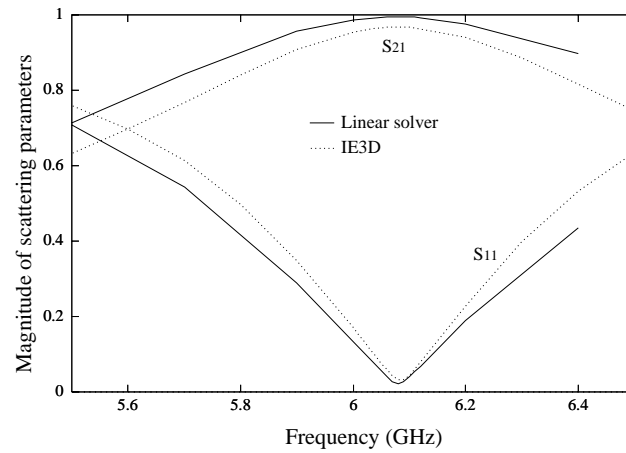
Figure 7.3: Magnitude of scattering parameters from the linear solver and a commercial EM software IE3D for the square microstrip patch filter in Figure 7.1: $W_{patch} = 5\text{mm}$, $\epsilon_r = 24$, $h = 0.508\text{mm}$, and $W_{strip} = 0.17\text{mm}$.
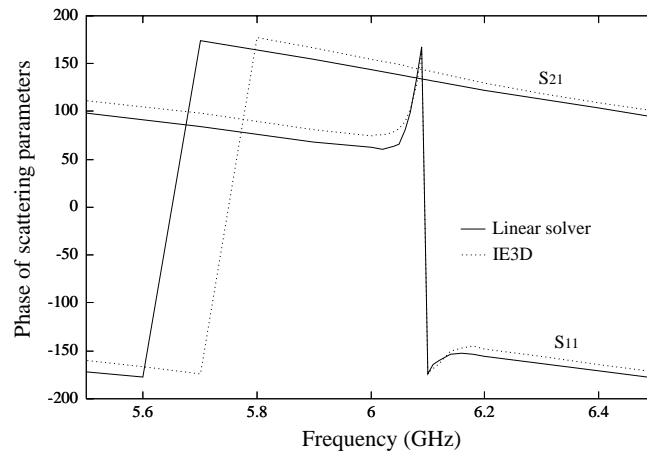
Figure 7.4: Phase of scattering parameters from the linear solver and a commercial EM software IE3D for the square microstrip patch filter in Figure 7.1: $W_{patch} = 5\text{mm}$, $\epsilon_r = 24$, $h = 0.508\text{mm}$, and $W_{strip} = 0.17\text{mm}$.
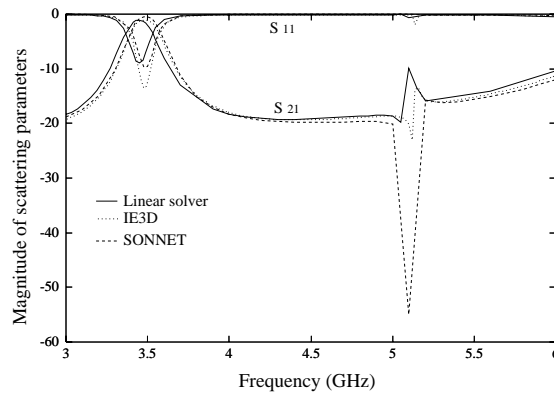
Figure 7.5: Magnitude of scattering parameters from the linear solver and commercial EM softwares IE3D and SONNET for the corner-cut microstrip patch filter in Figure 7.2: W_{patch} is half a wavelength at resonance, $\epsilon_r = 24$, $h = 0.508$mm, and $W_{strip} = 0.17$mm.
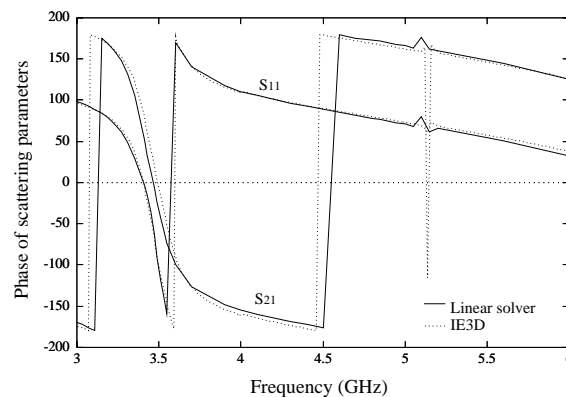
Figure 7.6: Phase of scattering parameters from the linear solver and a commercial EM software IE3D for the corner-cut microstrip patch filter in Figure 7.2: W_{patch} is half a wavelength at resonance, $\epsilon_r = 24$, $h = 0.508$mm, and $W_{strip} = 0.17$mm.

obtained by a commercial EM software IE3D are also given for comparison. The agreement between them is quite good. IE3D needs 23 ×22 charge cells over the patch area to obtain the results, whereas, the linear solver needs just 8×11 charge cells. This is because the linear solver can handle non-uniform gridding. Much more segments are put in the region where the current density changes very rapidly, such as edge areas, while just a few segments are put in the region where the current density changes very slowly.

Figures 7.5 and 7.6 present the magnitude and phase of the scattering parameters as a function of frequency for the corner-cut patch filter. The results obtained from IE3D and SONNET are also presented together for comparison. It is also found that the linear solver is in good agreement with IE3D and SONNET.

The loaded Q value could be determined from the frequency response of the transmission coefficient. It is found that the loaded Q value is 6.1 for the square patch filter from Figure 7.3 and 19.2 for the corner-cut patch filter from Figure 7.5.

7.3.2   Current distribution over the patch

The HTSC film material exits from the superconducting phase because the current density of the HTSC material is very high and exceeds the critical current density. In order to make the current density of a microstrip component low, a topology of the device may be designed such that the current spreads uniformly over the device and/or the device has a large surface area. That makes the device to be inherently capable of handling higher power. Thus a 2-D microstrip patch has a lower current density than a 1-D microstrip line does, and a 2-D microstrip patch circuit could handle higher power than a 1-D microstrip transmission line circuit. In addition, the 2-D microstrip patch filter has higher unloaded Q value
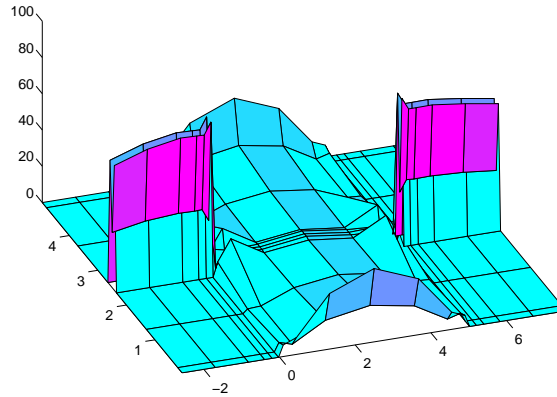
Figure 7.7: Surface current density in the longitudinal direction in the square patch filter circuit in Figure 7.1: $W_{patch} = 5$mm, $\epsilon_r = 24$, $h = 0.508$mm, and $W_{strip} = 0.17$mm.
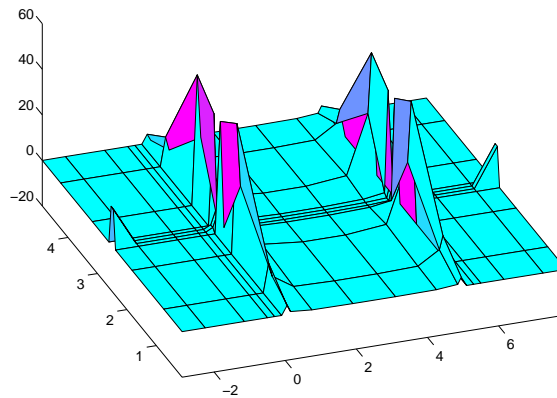
Figure 7.8: Surface current density in the transverse direction in the square patch filter circuit in Figure 7.1: $W_{patch} = 5$mm, $\epsilon_r = 24$, $h = 0.508$mm, and $W_{strip} = 0.17$mm.

than the 1-D microstrip line filter.

For the patch filter in Figure 7.1 the 3-D views of the current density distributions over the patch and microstrip lines in the longitudinal and transverse directions are shown in Figures 7.7 and 7.8, respectively. The length of the microstrip line is $\lambda/10$. The operating frequency is 6.1 GHz, the input power is 4 dBm, and the input voltage is 1 V. In the application of the moment method we have used three current segments along the transverse direction of the interconnecting microstrip line, so that the edge behavior of the current distribution of the strip could be reflected more accurately.

It is apparent from Figures 7.7 and 7.8 that the current density in the longitudinal direction is much larger than the current density in the transverse direction, especially for the interconnecting microstrip lines. This is what we expected. It is observed from Figure 7.7 that the current density over the microstrip lines is much higher than the current density over the patch resonator. As we mentioned before, this is because the current spreads over the larger patch area. While, since the microstrip line is much narrower than the patch, the current density over it is much higher.

7.4 Scattering parameters for the HTSC interconnecting line

In this section $|S_{21}|$ and $|S_{11}|$ at different power level are computed for these two microstrip patch filters when the input and output interconnecting lines are constructed from HTSC material.

For the square patch filter, the loaded Q value is 6.08, and $W_{strip} = 0.17$ mm
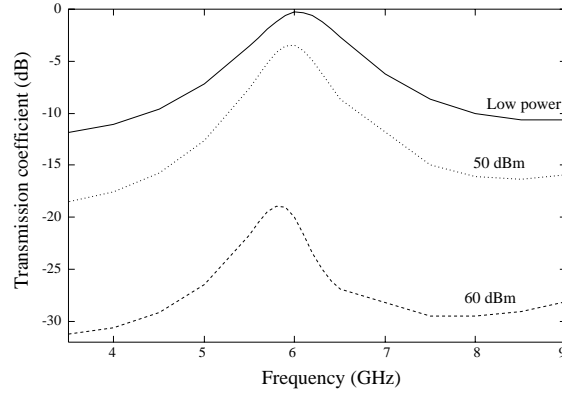
Figure 7.9: The transmission coefficient $|S_{21}|$ at different power levels for HTSC input and output lines in the square patch filter in Figure 7.1: $W_{patch} = 5$mm, $\epsilon_r = 24$, $h = 0.508$mm, $W_{strip} = 0.17$mm, and the length of the interconnecting microstrip line is $\lambda/10$.
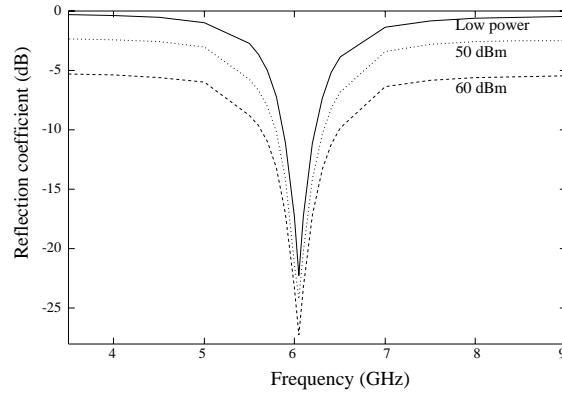
Figure 7.10: The reflection coefficient $|S_{11}|$ at different power levels for HTSC input and output lines in the square patch filter in Figure 7.1: $W_{patch} = 5$mm, $\epsilon_r = 24$, $h = 0.508$mm, $W_{strip} = 0.17$mm, and the length of the interconnecting microstrip line is $\lambda/10$.
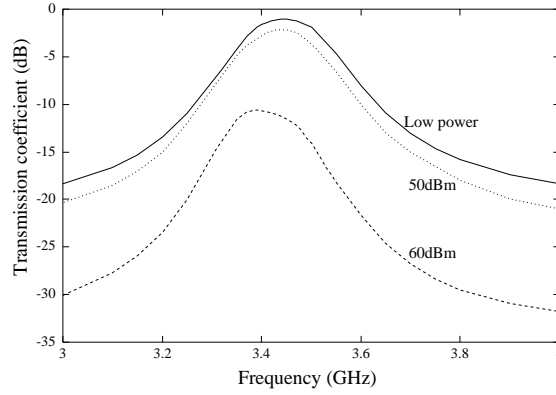
Figure 7.11: The transmission coefficient $|S_{21}|$ at different power levels for HTSC input and output lines in the corner-cut patch filter in Figure 7.2: W_{patch} is half a wavelength at resonance, $\epsilon_r = 24$, $h = 0.508$mm, $W_{strip} = 0.17$mm, and the length of the interconnecting microstrip line is $\lambda/10$.
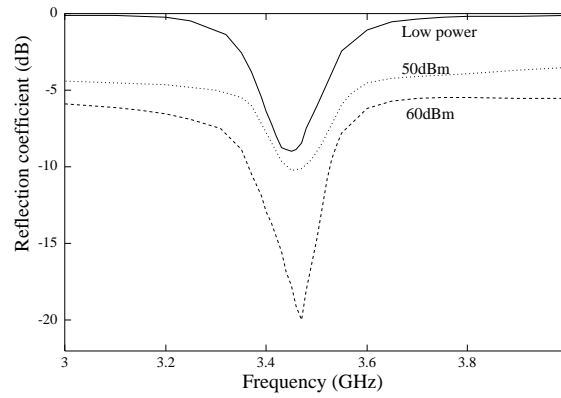

Figure 7.12: The reflection coefficient $|S_{11}|$ at different power levels for HTSC input and output lines in the corner-cut patch filter in Figure 7.2: W_{patch} is half a wavelength at resonance, $\epsilon_r = 24$, $h = 0.508$mm, $W_{strip} = 0.17$mm, and the length of the interconnecting microstrip line is $\lambda/10$.

and W_{patch} = 5 mm. Thus, W_{patch}/W_{strip} = 29.6, which is larger than Q_{loaded}. According to the discussion in Section 7.2 we can then expect that the loss in the microstrip interconnecting line would dominate the behaviors of the filter [45].

Figure 7.9 shows the calculated $|S_{21}|$ at different power levels: very low power, 50 dBm, and 60 dBm. It is observed that the entire curve simply shifts down at high power, thus the change of Q is not apparent. That is what we expected. The current density in the interconnecting microstrip line is much larger than the current density in the patch, especially, the current density near the edges of the microstrip line is very very large. This results in that the loss in the microstrip line is much larger than the loss in the patch. Consequently, the loss in the microstrip line is dominant, i.e., the insertion loss of the filter is determined totally by the loss in the microstrip line. Thus, at high power the entire filter circuit is equivalent to a patch resonator and two attenuators which connect the patch resonant to the input and output ports. That is the reason that the change of Q can not be observed. The very lossy HTSC input and output interconnecting lines act as attenuators. This is consistent with our previous conclusion in Chapter 6 that the HTSC interconnecting line behaves like an attenuator at high power [39].

The calculated $|S_{11}|$ at those power levels is shown in Figure 7.10. The point that is worth to mention is that the entire curve also shifts down with high power. This means that the unitary property of S-parameter does not hold any more. Apparently, a fraction of power is dissipated inside the circuit due to high conductor loss.

For the corner-cut patch filter it is also found that $W_{patch}/W_{strip} > Q_{loaded}$. Therefore, we expect the results similar to those of the square patch filter. So, for the corner-cut patch filter, the transmission coefficient $|S_{21}|$ and the reflection coefficient $|S_{11}|$ at different power levels: very low power, 50 dBm, and 60 dBm,

are calculated, and they are shown in Figures 7.11 and 7.12, respectively.

7.5   Scattering parameters for the gold interconnecting line

Due to the resultant high conductor loss at high power, the Q value of the resonator should reduce. In order to observe the change of Q of the resonator, we use the gold microstrip line as the input and output interconnecting lines of the filter. Because the loss of gold conductor is not changed with the applied power.

For the square patch filter the calculated transmission coefficient $|S_{21}|$ and the reflection coefficient $|S_{11}|$ at different power levels: very low power, 50 dBm, and 60 dBm, respectively, are plotted in Figures 7.13 and 7.14. It is observed that the Q of the resonator reduces to 2.5 for an input power of 60 dBm. When the power level is high, the insertion loss becomes very large. Eventually, the circuit will collapse. In the meantime, the reflection coefficient reduces as well. This indicates that a fraction of power is consumed in the nonlinear ohmic loss.

Similar results for the corner-cut patch filter are shown in Figures 7.15 and 7.16. From Figure 7.15 the Q of the resonator reduces to 10.8 for an input power of 60 dBm.

It is also observed that the insertion loss for HTSC interconnecting lines is larger than that for the gold lines at high power around the resonant frequency. For the square patch filter, by comparing Figure 7.13 with Figure 7.9, the maximum insertion loss is 24 dB for the HTSC interconnecting lines and 5 dB for the gold interconnecting lines at the input power of 60 dBm. For the corner-cut patch filter, by comparing Figure 7.15 with Figure 7.11, the maximum insertion loss is 10.6 dB
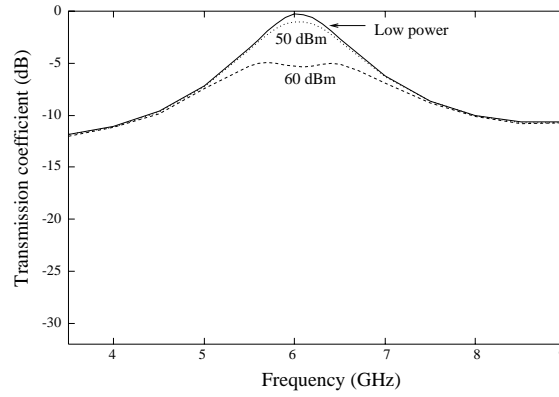
Figure 7.13: The transmission coefficient $|S_{21}|$ at different power levels for gold input and output lines in the square patch filter in Figure 7.1: $W_{patch} = 5$mm, $\epsilon_r = 24$, $h = 0.508$mm, $W_{strip} = 0.17$mm, and the length of the interconnecting microstrip line is $\lambda/10$.
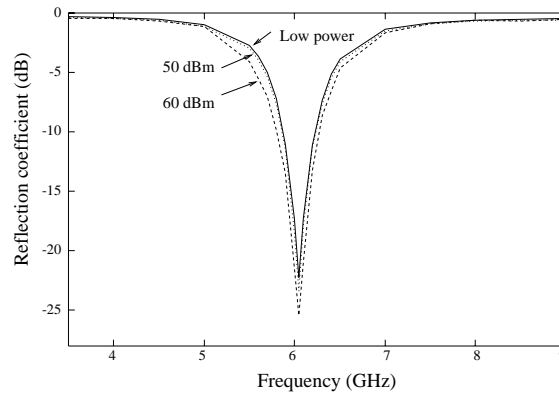

Figure 7.14: The reflection coefficient $|S_{11}|$ at different power levels for gold input and output lines in the square patch filter in Figure 7.1: $W_{patch} = 5$mm, $\epsilon_r = 24$, $h = 0.508$mm, and $W_{strip} = 0.17$mm, and the length of the interconnecting microstrip line is $\lambda/10$.
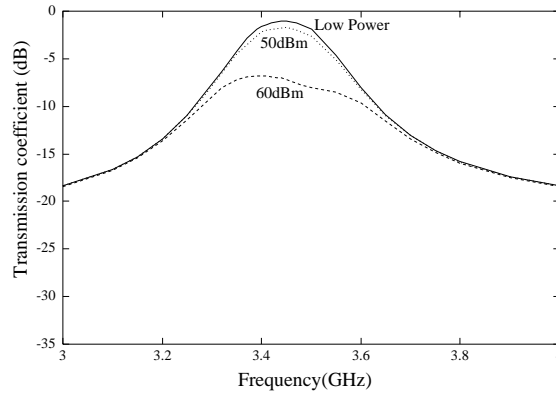
Figure 7.15: The transmission coefficient $|S_{21}|$ at different power levels for gold input and output lines in the corner-cut patch circuit in Figure 7.2: W_{patch} is half a wavelength at resonance, $\epsilon_r = 24$, $h = 0.508$mm, $W_{strip} = 0.17$mm, and the length of the interconnecting microstrip line is $\lambda/10$.
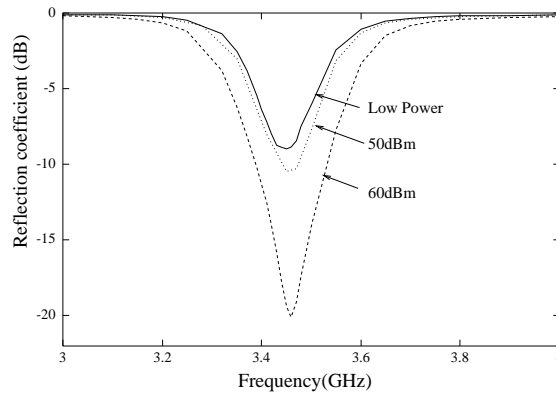

Figure 7.16: The reflection coefficient $|S_{11}|$ at different power levels for gold input and output lines in the corner-cut patch circuit in Figure 7.2: W_{patch} is half a wavelength at resonance, $\epsilon_r = 24$, $h = 0.508$mm, $W_{strip} = 0.17$mm, and the length of the interconnecting microstrip line is $\lambda/10$.

for the HTSC interconnecting lines and 6.8 dB for the gold interconnecting lines at the input power of 60 dBm. This is another evidence that the loss in the HTSC interconnecting lines dominates the behaviors of the filter at high power.

7.6 Third harmonic output power

Figure 7.17 shows the powers delivered to the load impedance (50 Ω) at the third harmonic frequency as a function of input power for the square patch filter, when the operating frequency is 6.1 GHz. The third harmonic output powers delivered to the load impedance (50 Ω) as a function of the input power at the resonant frequency for the corner-cut patch filter are shown in Fig. 7.18. In both figures the line of slope 3 is also drawn to show that the third harmonic output power is below that line as the input power is larger than 50 dBm in Figure 7.17 and 45 dBm in Figure 7.18, respectively. This is because higher order harmonics come to play and the conductor loss becomes very large at high power level.

It is also found that the third harmonic output power for the gold microstrip lines is larger than that for the HTSC microstrip lines. The reason that HTSC lines has lower harmonic output power is due to much higher conductor loss at high input power, as compared with the gold lines. That means that there is trade-off in using gold line and HTSC line. Using gold line results in lower insertion loss but higher harmonic generation.

7.7 Conclusions

The single-mode and double-mode HTSC microstrip patch filters have been simulated to show the variation of the transmission and reflection coefficients with the
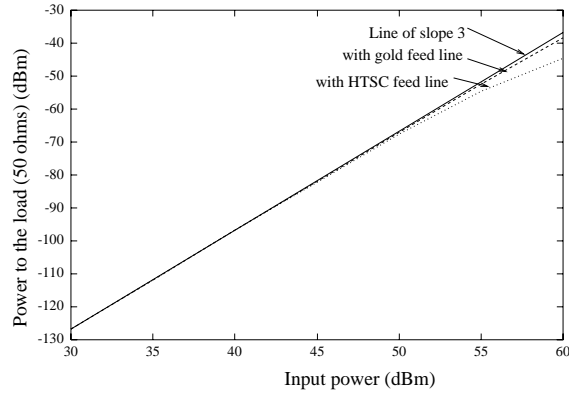
Figure 7.17: The third harmonic power delivered to the load (50 ohms) in the square microstrip patch filter in Figure 7.1: $W_{patch} = 5$mm, $\epsilon_r = 24$, $h = 0.508$mm, $W_{strip} = 0.17$mm, and the length of the interconnecting microstrip line is $\lambda/10$.
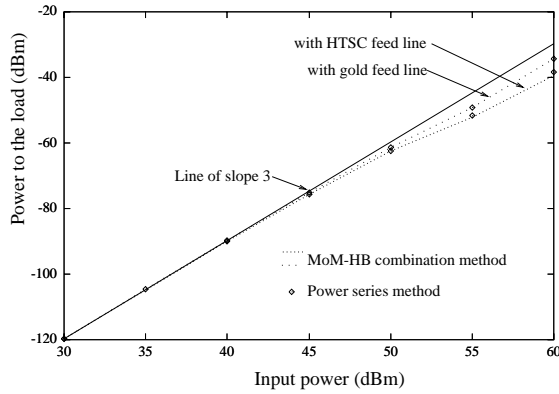
Figure 7.18: The third harmonic power delivered to the load (50 ohms) in the corner-cut microstrip patch filter in Figure 7.2: W_{patch} is half a wavelength at resonance, $\epsilon_r = 24$, $h = 0.508$mm, $W_{strip} = 0.17$mm, and the length of the interconnecting microstrip line is $\lambda/10$.

applied power and the output power at the third harmonic frequency. The transmission and reflection coefficients for a HTSC microstrip interconnecting line at different power levels have been evaluated for the HTSC interconnecting lines and the non-HTSC (gold) interconnecting lines. In the case of the HTSC interconnecting lines the curve simply shifts down at high power, because the conductor loss in HTSC line is dominant. Thus the change of Q is not apparent. This is also consistent with our conclusion drawn in Chapter 6, that the HTSC interconnecting line behaves like an attenuator at high power. In the case of the gold interconnecting lines, due to the high conductor loss in the patch resonator at high power, the Q value is reduced significantly for a high input power. Since gold is a linear material, the loss does not change with the input power. When the power level is high, the insertion loss becomes very large and the reflection coefficient reduces as well. Also, the insertion loss for the HTSC line is larger than that for the gold line at high power. The third harmonic output powers delivered to the load as a function of the input power at the resonant frequency are obtained for HTSC and non-HTSC (gold) microstrip interconnecting lines. The harmonic power for the HTSC line is lower than that for the gold line, this is because the more power is consumed in the form of conductor loss in the case of HTSC line.

Chapter 8

Gilded HTSC microstrip lines

8.1 Introduction

The issue of improving the power handling capability of HTSC microstrip circuits will be dealt with in this chapter. In this study the power handling capability of a HTSC microstrip line is defined as the maximum power the line can conduct for a given amount of harmonic (including intermodulation) generation. In this chapter a novel circuit layout design is proposed to gild the HTSC microstrip line to reduce the very high current density at the edges of HTSC microstrip line. A general analysis approach, which is suitable for any thickness of gilding layer, is obtained by integrating the multi-port network theory into the two proposed methods—the MoM-HB combination method and the power series method. The approach is then employed for analysis of gilded HTSC microstrip lines.

In Section 8.2 the proposed circuit layouts are discussed regarding how to improve the power handling capability of HTSC thin film circuits. In Section 8.3 the general modeling approach is addressed. The formulation is derived by integrating

122

the multi-port network theory into the MoM-HB combination formulation. To facilitate the derivation, two surfaces are specified. The harmonic balance technique is then applied to the surface including only the HTSC material. The formula of the conductor loss, which contains the contributions from both the HTSC material and gold, is also derived. In Section 8.4 numerical examples are given to show the validity of the general approach, and the results for gilded HTSC microstrip line are compared with the results for pure gold line and HTSC line. Finally, Section 8.4 concludes this chapter.

8.2 Proposed circuit layouts

The origin of HTSC nonlinearity is the RF magnetic field or RF current dependence of surface impedance of the HTSC material. From the analysis of the nonlinear effects of HTSC microstrip circuits in the previous chapters, we have learnt that the current density is much higher at the region near the edges of the microstrip line, which causes strong nonlinear effects. To improve the power handling capability, better HTSC films, in terms of lower nonlinearity, will help [46]. Operation at lower frequencies will decrease the nonlinearity of HTSC devices. Better circuit design also helps. From the point of view of the circuit design, we may use wider microstrip line to spread the current over a large area so as to reduce the current density. For instance, a wider HTSC transmission line carrying the same current but less current density will ease the nonlinear effects and handle high power [49].

Because the nonlinear effects in the HTSC material dominates at the highest current density, in general, the power handling capability is limited by the maximum current density in the HTSC circuit. Many researchers have tried to design high power HTSC thin film circuits by using different circuit layouts to reduce the current

density distribution [50] [51]. For example, [50] reported that a microstrip filter design employing split-resonators and inserted I/O line coupling structure for high power HTSC thin film filters. The use of split-resonators together with the inserted I/O coupling helps to redistribute the current more evenly over the resonators. The inserted line coupling structure also eliminates the sharp corners and narrow gaps associated with conventional I/O coupling structures.

In this chapter we propose gilded HTSC microstrip lines for improving the power handling capability. One gilded HTSC microstrip line is to lay two narrow gold strips on the edges of the top surface of the HTSC strip, i.e., the HTSC strip is gilded with gold, as shown in Figure 8.1. Another way of gilding would be to gild the HTSC strip from bottom to top by its two sides, i.e., the HTSC strip with two gold strips butting on its two sides, as shown in Figure 8.2, because there are also high current densities at the edges of the bottom surface. Thus both the top and bottom edges are covered.

From the point of view of reduction of harmonic generation, it is expected that the latter design is better than the former one. While, from the point of view of loss reduction, it is expected that the former design is better than the latter one. Due to the edge effect of the current distribution of the microstrip line, that is, much much higher current density in the regions near the edges, for the latter design the most of current flows through the gold material gilded against the two sides of the microstrip line. Consequently, there is not much improvement of loss reduction at the low and medium power level, as compared with pure gold microstrip line. Besides, according to today's fabrication process of HTSC microwave circuits, it is almost impossible to fabricate the latter design. While the former design can be fabricated very easily. Therefore, only the former design is analyzed in this chapter.

The idea of gilding is to let the very high current densities near the edges
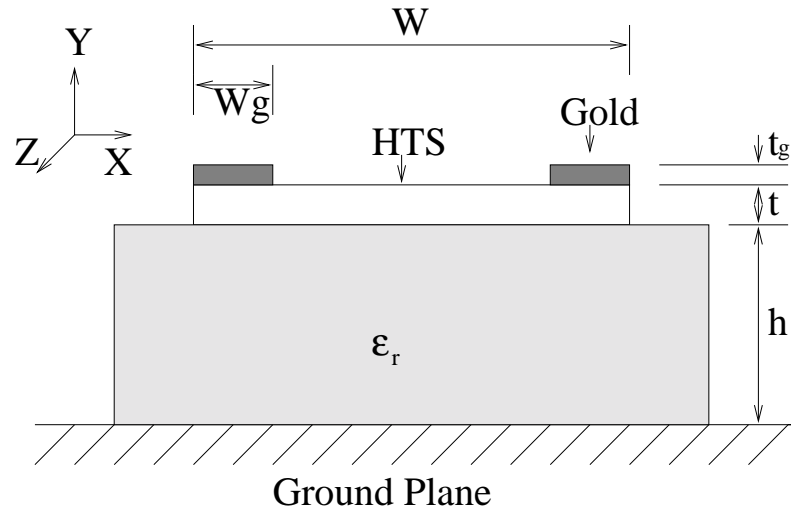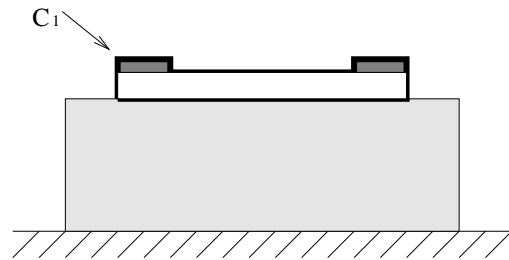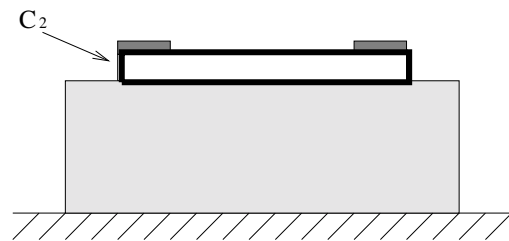
Figure 8.1: Diagram of a microstrip line structure with two narrow gold strips on the edges of the top surface of the HTSC strip and the specified surface C_1 and C_2
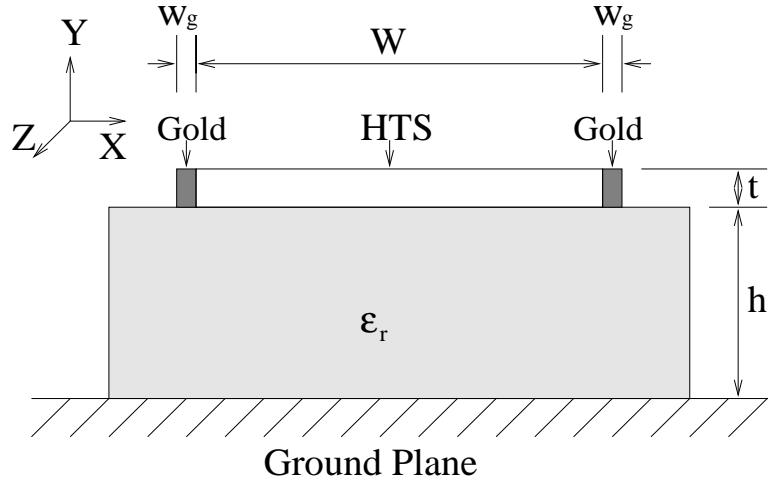
Figure 8.2: Diagram of a microstrip line structure with two gold strips butting on the two sides of the HTSC strip

flow through the gold instead of the HTSC. Being non-superconductive, the gold edges do not generate harmonics and show any nonlinear increase in loss, thus the nonlinear effects are alleviated. Nevertheless, an extra ohmic loss is introduced due to the lossy gold. It is required that the loss be kept low, say at a limit of an order of magnitude less than that of the normal gold microstrip line. As a result, the maximum power handling capability should be defined as whenever either the harmonic limit or the loss limit is reached first.

In order to analyze these gilded HTSC microstrip line, the harmonic balance technique has to be applied on the boundary containing only the HTSC part of the microstrip line. Since the thickness of the gilded strip may be smaller than the skin depth of gold, in order to account for such a thickness, the effective surface impedance of gold is found by using the *multi-port network theory*, which is used to convert the quantities on the surface containing only HTSC strip into the surface

containing the entire gilded HTSC strip.

8.3 Formulation based on the MoM-HB combination method

Figure 8.1(a) shows the cross section of a microstrip line structure with a gilded-edged HTSC strip, where two narrow gold strips are put on the edges of the top surface of the HTSC strip. To perform the nonlinear analysis for this structure two surfaces are specified. The first surface, denoted by C_1, is the boundary of the *entire structure* (including HTSC strip and the two gold strips), as shown in Figure 8.1(b). The second surface, denoted by C_2, contains *only the HTSC strip*, as shown in Figure 8.1(c).

8.3.1 Matrix equation on C_1

We formulate this problem by starting with the boundary condition on the surface C_1. Similar to what we have done in Chapter 3, by using an appropriate Green's function and the moment method formulation we arrive at the following matrix form equation:

$$[Z][I_1] + [V_s] = [V_i] \tag{8.1}$$

where $[Z]$ is an impedance matrix characterizing the field interaction outside the surface C_1, $[I_1]$ is a column vector representing the currents flowing on surface C_1, $[V_i]$ is a column vector representing the applied source voltage, and $[V_s]$ represents the voltage due to the current flowing through a surface impedance. Over the surface of the HTSC material $[V_s]$ is a nonlinear function of $[I_1]$, while over the surface of the gold $[V_s]$ is a linear function of $[I_1]$.

The harmonic balance technique must be performed on the surface C_2 instead of the surface C_1, because we don't know the surface impedance on the interface between gold conductor and HTSC material. Therefore, the quantities on C_1 must be transferred to the surface C_2. To this end, in the matrix formulation outlined in (8.1) we treat the surfaces C_1 and C_2 as *multi-port networks*. The voltages and currents at C_1 and C_2 multi-ports are denoted by $([V_1], [I_1])$ for C_1 and $([V_2], [I_2])$ for C_2. It is noticed that the ports on the vertical surfaces of the gold material have to be dealt with separately. The reason is that the quantities on the that surface don't have to be converted into surface C_2.

To facilitate the derivation, the surface C_1 is grouped into two portions: one is the vertical surfaces of gold material, denoted by C_{1gv}, the other is the rest surface of C_1, denoted by C_{1h}. Let $([V_{1gv}], [I_{1gv}])$ represent the voltages and currents at the ports on the surface C_{1gv}, and $([V_{1h}], [I_{1h}])$ represent the voltages and currents on the surface C_{1h}.

In order to obtain the current distribution on the surface C_1, we first express the voltages and currents on the surface C_{1gv}, $([V_{1gv}], [I_{1gv}])$, in terms of the voltages and currents on the surface C_{1h}, $([V_{1h}], [I_{1h}])$. We then use the multi-port network theory to transfer those voltages and currents onto the surface C_2. Consequently, we can use the harmonic balance technique to find the currents on the surface C_2.

According to the port voltages and port currents on C_{1gv} and C_{1h}, we partition the matrix form equation (8.1) into the following form:

$$
\begin{bmatrix} [Z_{hh}] & [Z_{hv}] \\ [Z_{vh}] & [Z_{vv}] \end{bmatrix} \begin{bmatrix} [I_{1h}] \\ [I_{1gv}] \end{bmatrix} - \begin{bmatrix} [V_{ih}] \\ [V_{igv}] \end{bmatrix} = - \begin{bmatrix} [V_{1h}] \\ [V_{1gv}] \end{bmatrix} \tag{8.2}
$$

where $[Z_{hh}]$ is the impedance matrix characterizing the current segments on C_{1h}, $[Z_{vv}]$ is the impedance matrix characterizing the current segments on C_{1gv}, and

$[Z_{hv}]$ and $[Z_{vh}]$ are the impedance matrices due to the mutual coupling between the current segments on C_{1h} and on C_{1gv}. $[V_{1h}]$ and $[V_{1gv}]$ are the source voltages applied to the surfaces C_{1h} and C_{1gv}, respectively. From (8.2) we have:

$$[Z_{hh}][I_{1h}] + [Z_{hv}][I_{1gv}] - [V_{ih}] = -[V_{1h}] \tag{8.3}$$

$$[Z_{hv}][I_{1h}] + [Z_{vv}][I_{1gv}] - [V_{igv}] = -[V_{1gv}] \tag{8.4}$$

In (8.4), it is known that

$$[V_{1gv}] = [Z_{sg}][I_{1gv}] \tag{8.5}$$

where $[Z_{sg}]$ is a diagonal matrix and represents the surface impedances of each current segment on the surface C_{1gv}. Substituting (8.5) into (8.4) yields:

$$[Z_{hv}][I_{1h}] + ([Z_{vv}] + [Z_{sg}])[I_{1gv}] - [V_{igv}] = 0 \tag{8.6}$$

By denoting

$$[Z_{vsg}] = [Z_{vv}] + [Z_{sg}] \tag{8.7}$$

(8.6) becomes

$$[Z_{hv}][I_{1h}] + [Z_{vsg}][I_{1gv}] - [V_{igv}] = 0 \tag{8.8}$$

From (8.8), we obtain

$$[I_{1gv}] = [Z_{vsg}]^{-1} ([V_{igv}] - [Z_{hv}][I_{1h}]) \tag{8.9}$$

where $[*]^{-1}$ denotes the inverse matrix. By substituting (8.9) into (8.3), we can eliminate I_{1gv}, so that we obtain the following equation:

$$\left([Z_{hh}] - [Z_{hv}][Z_{vsg}]^{-1}[Z_{vh}]\right)[I_{1h}] + [Z_{hv}][Z_{vsg}]^{-1}[V_{igv}] - [V_{ih}] = -[V_{1h}] \tag{8.10}$$

(8.10) is the relation between voltages and currents on the surface C_1 excluding the vertical surface portions of gold material. Based on (8.10) we will derive the relation between voltages and currents on the surface C_2 in terms of the source voltages.

8.3.2 Derivation of ABCD matrix

This section is to find the $ABCD$ parameters, which are used to transfer the quantities on the surface C_1 onto the surface C_2, or vice versa. That is, find the relation between $(([V_{1h}], [I_{1h}]))$ and $(([V_2], [I_2]))$.

According to the linear multi-port network theory, $([V_{1h}], [I_{1h}])$ and $([V_2], [I_2])$ at those ports corresponding to the gold boundaries are related by the following $ABCD$ parameters:

$$\begin{bmatrix} [V_2] \\ [I_2] \end{bmatrix} = \begin{bmatrix} [A_g] & [B_g] \\ [C_g] & [D_g] \end{bmatrix} \begin{bmatrix} [V_{1h}] \\ [I_{1h}] \end{bmatrix} \tag{8.11}$$

where $[A_g]$, $[B_g]$, $[C_g]$ and $[D_g]$ are diagonal matrices and their diagonal elements are respectively equal to:

$$\cosh(\gamma t_g), \quad Z_{0g}\sinh(\gamma t_g), \quad \frac{\sinh(\gamma t_g)}{Z_{0g}}, \quad \cosh(\gamma t_g) \tag{8.12}$$

where t_g is the thickness of the gilded gold strips, σ is the conductivity of gold, γ and Z_{0g} are the propagation constant and the characteristic impedance of gold material, respectively. They are given by:

$$\gamma = \sqrt{j\omega\mu\sigma}, \qquad Z_{0g} = (1+j)\sqrt{\omega\mu/2\sigma} \tag{8.13}$$

It is obvious that $([V_{1h}], [I_{1h}])$ and $([V_2], [I_2])$ are identical in the other portions that are common to C_1 and C_2 and corresponding to HTSC surface:

$$[V_2] = [V_{1h}] \tag{8.14}$$

$$[I_2] = [I_{1h}] \tag{8.15}$$

Therefore, we can obtain the relation between $([V_{1h}], [I_{1h}])$ and $([V_2], [I_2])$ by using the following $ABCD$ parameters:

$$\begin{bmatrix} [V_2] \\ [I_2] \end{bmatrix} = \begin{bmatrix} [A] & [B] \\ [C] & [D] \end{bmatrix} \begin{bmatrix} [V_{1h}] \\ [I_{1h}] \end{bmatrix} \tag{8.16}$$

where $[A]$, $[B]$, $[C]$ and $[D]$ are diagonal matrices and given as follows:

$$[A] = \begin{bmatrix} [\mathbf{I}] & [0] \\ [0] & [A_g] \end{bmatrix} \tag{8.17}$$

$$[B] = \begin{bmatrix} [0] & [0] \\ [0] & [B_g] \end{bmatrix} \tag{8.18}$$

$$[C] = \begin{bmatrix} [0] & [0] \\ [0] & [C_g] \end{bmatrix} \tag{8.19}$$

$$[D] = \begin{bmatrix} [\mathbf{I}] & [0] \\ [0] & [D_g] \end{bmatrix} \tag{8.20}$$

where $[\mathbf{I}]$ denotes the unity matrix, and $[0]$ denotes the zero matrix, i.e., all elements in $[0]$ are zeros. By using (8.16) we can transfer $([V_{1h}], [I_{1h}])$ onto C_2, or vice versa, transfer transfer $([V_2], [I_2])$ onto C_1.

8.3.3   Matrix equation on C_2

Now we want to express $([V_2], [I_2])$ in terms of the source voltages $([V_{ih}], [V_{igv}])$. By substituting $[V_{1h}]$ in (8.10) into (8.16) to eliminate $[V_{1h}]$, yields

$$[V_2] = [B][I_{1h}] - [A][Z_{hsvg}][I_{1h}] - [A][Z_{hv}][Z_{svg}]^{-1}[V_{igv}] + [A][V_{ih}] \tag{8.21}$$

$$[I_2] = [D][I_{1h}] - [C][Z_{hsvg}][I_{1h}] - [C][Z_{hv}][Z_{svg}]^{-1}[V_{igv}] + [C][V_{ih}] \tag{8.22}$$

where we denote

$$[Z_{hsvg}] = [Z_{hh}] - [Z_{hv}][Z_{svg}]^{-1}[Z_{vh}] \tag{8.23}$$

From (8.22) we obtain $[I_{1h}]$:

$$[I_{1h}] = ([D] - [C][Z_{hsvg}])^{-1} \left([I_2] + [C][Z_{hv}][Z_{svg}]^{-1}[V_{igv}] - [C][V_{ih}] \right) \tag{8.24}$$

By substituting (8.24) into (8.21) to eliminate $[I_{1h}]$, we finally obtain the equation for $[V_2]$ and $[I_2]$ in terms of $[V_{ih}]$ and $[V_{igv}]$:

$$[V_2] = [E][I_2] - [F][V_{ih}] + [G][V_{igv}] \tag{8.25}$$

where $[E]$, $[F]$, and $[G]$ are given as follows:

$$[E] = ([B] - [A][Z_{hsvg}]) \ ([D] - [C][Z_{hsvg}])^{-1} \tag{8.26}$$

$$[F] = [E][C] - [A] \tag{8.27}$$

$$[G] = [F][Z_{hv}][Z_{svg}]^{-1} \tag{8.28}$$

(8.25) is the relation between voltages and currents on the surface C_2. At this point we are ready to apply the harmonic balance technique for nonlinear analysis.

8.3.4 Harmonic balance equation

Due to the nonlinearity of HTSC material the relation between $[V_2]$ and $[I_2]$ in (8.25) is nonlinear. Therefore, (8.25) is a harmonic balance equation. Similar to what we have done in the MoM-HB combination method, the quantities $[V_2]$ and $[I_2]$ can be solved by using the iterative procedure developed in the MoM-HB combination method.

The currents on the surface C_1 can be obtained from the currents on C_2 by using above $ABCD$ parameters again. That is, $[I_{1h}]$ can be found by substituting $[I_2]$ into (8.24), and $[I_{1gv}]$ can be found by substituting $[I_{1h}]$ into (8.9).

8.3.5   Conductor loss

Once the currents J_2 on surface C_2 are obtained, the surface resistance on C_2, due to the nonlinear HTSC material, is

$$R_s = R_{s0} + R_{s2}|J_2|^2 \tag{8.29}$$

where R_{s0} and R_{s2} are constants and determined from measurements. The surface reactance is

$$X_s = \omega\mu\lambda_L(T) \tag{8.30}$$

where $\lambda_L(T)$ is the penetration depth of HTSC material at temperature T. The surface impedance $Z_s = R_s + jX_s$. Hence, the surface impedance on C_2 is

$$Z_{s2} = R_{s0} + R_{s2}|J_2|^2 + j\omega\mu\lambda_L(T) \tag{8.31}$$

The loss is computed using surface resistance notion. The surface resistance, which is the real part of the surface impedance, has different values over the HTSC and gold surfaces. According to the the transmission line theory, on the gold surface the surface impedance is:

$$Z_g = Z_{0g}\frac{Z_{s2} + Z_{0g}\tanh(\gamma t_g)}{Z_{0g} + Z_{s2}\tanh(\gamma t_g)} \tag{8.32}$$

Therefore, the surface resistance, R_g, is given by the real part of Z_g. On the HTSC surface the surface resistance is: $R_H = R_{s0} + R_{s2}|J_1|^2$. Now we can define a single *effective* surface resistance as follows:

$$R_{eff}(P) = \frac{1}{|\int J_{1z}dx|^2}\left(\int_{C_{1g}} R_g|J_{1zg}|^2 dx + \int_{C_{1H}} R_H|J_{1zH}|^2 dx\right) \tag{8.33}$$

where J_{1z} is the longitudinal current density on surface C_1, J_{1zg} and J_{1zH} are the longitudinal current densities on the gold and HTSC portion of surface C_1, respectively, and C_{1g} is the gold portion of C_1, and C_{1H} is the HTSC portion of C_1.

8.4 Formulation based on the power series method

The derivation of the formulation based on the power series method is the same as the formulation based on the MoM-HB combination method up to Section 8.3.3. Since the rest formulation is similar to that in the power series method, it is not necessary to do the formulation based on the power series method here again. The following is the brief explanation how to do the formulattion for the gilded microstrip line design based on the concept of the power series method.

First, we find the relation between $[V_2]$ and $[I_2]$. Then, we substitute it into (8.25) so as to combine the term in the right-hand side with the term in the left-hand side. By solving the matrix equation we can find the current distribution at the fundamental frequency.

Next, we find the excitation voltages at higher order harmonic frequency from that fundamental current.

Finally, we can obtain the current distributions at higher order harmonics by applying the higher order voltage excitation.

8.5 Numerical results

A typical 50 Ω HTSC microstrip line with gilded edges on the top surface of HTSC strip is investigated [52]. The line has a width of $w = 0.17$ mm, a thickness of $t = 0.6$ μm, and a length of $L = 6$ mm. The substrate thickness $h = 0.508$ mm with $\epsilon_r = 24$. The linear and nonlinear coefficients for the HTSC material are the same as before and copied here: $R_{s0} = 1.4868 \times 10^{-5} \Omega$, $R_{s2} = 4.8270 \times 10^{-9} \Omega/Oe^2$, The penetration depth of HTSC material is $\lambda_L(T) = 0.323$ μm when $T = 77$ K.

The width of the two gold strips is $w_g = 25$ μm. The output power as a function of the input powers at the third harmonic frequency are computed at the frequency of 4 GHz for different thickness of gold strips, t_g. The results for $t_g = 0.3$ μm and $t_g = 2$ μm and for the HTSC strip without gilded edges are given in Figure 8.3. It is observed that, at the same input power level, the HTSC strip with gilded edges generates a third harmonic power of at least 6 dB lower than that without gilded edges. The results obtained by using the formulation based on the power series method are also presented in Figure 8.3 for comparison. It is seen that they are in good agreement.
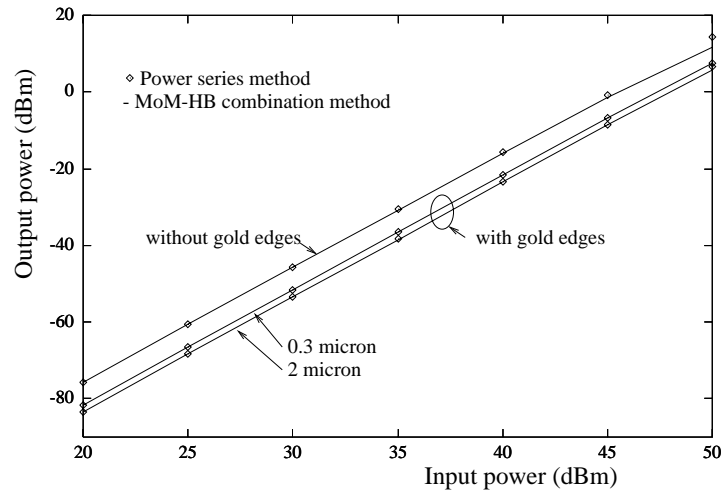
Figure 8.3: Output power vs. input power at the third harmonic frequency

The conductor losses as a function of input powers are shown in Figure 8.4, in which the result for a pure gold strip is also given. It is always the case that the pure gold strip has the largest attenuation. In spite of the increase in the conductor loss for the HTSC strip with gold strips, the attenuation constant for thicker gold strips (when $t_g = 2$ μm) is still very small at lower power levels, as compared with

a pure gold microstrip line, nearly one order of magnitude less than that of a pure gold strip.
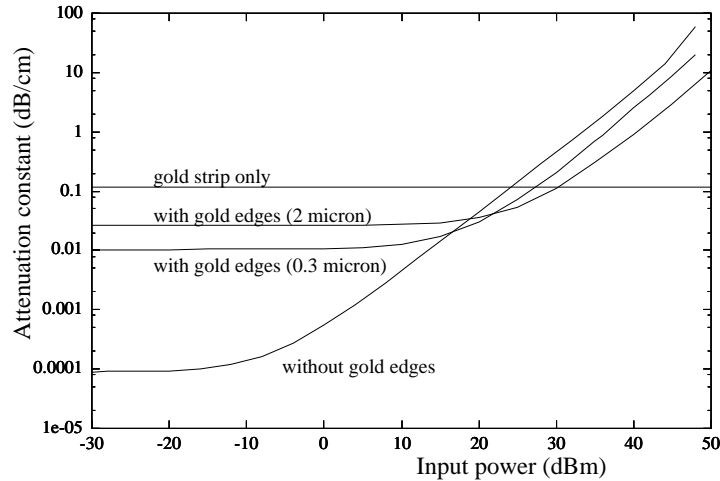
Figure 8.4: Attenuation constant of the gilded-edged HTSC microstrip line as a function of the input power

8.6   Conclusions

In this chapter the issue of improving power handling capability of the HTSC thin film microwave circuits has been dealt with. The HTSC microstrip line structures with gilded edges have been proposed for improving the power handling capability based on a specified limit of harmonic generation. One way to do gilding is to lay two narrow gold strips on the edges of the top surface of the HTSC strip in a microstrip line. The other way is to gild the HTSC strip from bottom to top by its two sides. The idea is to let the very high current densities near the edges flow through the gold instead of the HTSC.

A general analysis approach, which integrates the multi-port network theory into the two proposed nonlinear analysis methods, has been derived and applied to the analysis. The results for the HTSC strip with gold strips of different thickness and without gilded edges have been obtained. At the same input power level, the HTSC strip with gilded edges generates a third harmonic power of at least 6 dB lower than that without gilded edges. The results obtained from the formulation based on both the power series method and the MoM-HB combination formulation are in excellent agreement. The conductor losses as a function of input powers have been obtained and compared with the result for a pure gold strip. The pure gold strip has the largest attenuation. In spite of the increase in the conductor loss for the HTSC strip with gold strips, the attenuation constant for thicker gold strips is still very small at lower power levels, as compared with a pure gold microstrip line, nearly one order of magnitude less than that of a pure gold strip.

Chapter 9

Conclusions

9.1   Summary

The purposes of this thesis were to investigate the nonlinear effects of HTSC thin film microstrip circuits and improve the power handling capability of the circuits. Two nonlinear analysis methods were proposed in order to study the nonlinearity of HTSC material. A novel circuit design was proposed to improve the power handling capability of HTSC thin film microwave circuits.

The MoM-HB combination method was based on the combination formulation of the moment method(MoM) and the harmonic balance(HB) technique. It consisted of linear and nonlinear solvers. The linear solver carried out linear analysis in the frequency-domain. The mixed potential integral equation(MPIE) involving the spatial forms of the vector and scalar potential Green's function was developed for an impedance surface. Then the moment method was employed to solve the MPIE. The complex image technique was applied to find the Green's function in a closed-form expression, which has been proven to be computationally very efficient. Thus

138

the field interaction and fringing field outside the HTSC material were taken into consideration.

The nonlinear solver performed nonlinear analysis by using the harmonic balance technique. Due to the nonlinear surface impedance of HTSC material, the matrix equation obtained from the moment method was treated as the so-called harmonic balance equation. The impedance matrix characterizing the field outside the HTSC material was evaluated at each harmonic frequency. The nonlinear $v - i$ characteristic of HTSC material was modeled by a power series in the time-domain and Fourier-transformed into the frequency-domain to fit into the harmonic balance equation. Then an iterative procedure was developed to solve the harmonic balance equation for the current distributions at different frequency components. The MoM-HB combination method was verified by applying it to a HTSC stripline filter for two-tone intermodulation and comparing the obtained results with the published measurement results.

In the power series method the impedance matrix in the moment method formulation was modified by adding the surface impedance to the self terms. The excitation voltages at higher order frequencies were derived from the current at the fundamental frequency according to the nonlinear characteristic of HTSC material. The higher order harmonic voltages were treated as the excitation at the corresponding frequency. The current distributions at higher order frequencies were then evaluated by applying the moment method again. For the non-uniform current distribution along the transverse direction, the average current was determined by evaluating the integral for the current distribution over the width.

Those two proposed methods were used to investigate the nonlinear half-wavelength strip dipole antenna circuits, where the conducting material is typical HTSC material or weakly or strongly nonlinear materials. A thorough comparison of the

results obtained from the two methods was made to show the agreement between them. The two methods were in excellent agreement for weak nonlinearities, and the agreement for slightly strong nonlinearities was still good. Based on the results obtained, the HTSC material was considered as weakly nonlinear material. Even order harmonics and odd order harmonics higher than the fifth harmonic could be neglected for HTSC nonlinearity.

The MoM-HB combination method takes the advantages of both the moment method and harmonic balance techniques, therefore, it was fast, accurate, and suitable for both weak and strong nonlinearities. This method converged very fast. It could be used to find the fundamental current redistribution, conductor loss, and the scattering parameters at the fundamental frequency.

The power series method was simple for finding the output power at higher order frequency. According to the results obtained it was suitable for weak nonlinearities. Moreover, the power series method was faster and needed less computer memory than the MoM-HB combination method, since the matrix equation was solved separately at each frequency and no iteration was involved.

In comparison with the differential equation approach, the proposed methods were basically the integral equation approach. Therefore, they were substantially faster than a differential equation FDTD-based approach. These two proposed methods were efficient, accurate, and suitable for distributed-type HTSC nonlinearity. Moreover, they could be easily incorporated into commercial EM CAD software to expand their capabilities.

The two proposed methods are suitable for the nonlinear problem in which the nonlinearity can be modeled by a surface impedance. As compared to the time-domain method, they have a couple of shortcomings. First, since in the two

proposed methods the $v - i$ characteristic of the HTSC material is modeled by using a power series, it is impossible to reflect the time history of voltage and current in the HTSC material. Second, since the two proposed methods are basically integral equation method which is best for sinusoidal or quasi-sinusoidal signal, it is very hard to deal with the pulse signal. In that case the time-domain method must be used.

HTSC microstrip lines were investigated for the nonlinear effects of HTSC materials on the current density distribution over the cross section of the microstrip line and the HTSC conductor loss as a function of the applied power. The thickness of the HTSC conductor was taken into account, and the effective surface impedances were also considered. Besides, much finer grids were put over the regions near the edges. It was concluded that an interconnecting HTSC microstrip line behaves like an attenuator at high power.

HTSC microstrip patch filters were studied, when the interconnecting line is constructed from HTSC and non-HTSC (gold) materials. It was found that the loss of the HTSC interconnecting line could dominate the behaviors of the filter at high power, if the width ratio of the patch resonator to the interconnecting line was larger than the loaded Q of the resonator. Therefore, the HTSC patch filter circuits must be designed carefully in order to take the advantage of the benefit promised by HTSC materials.

The issue of improving power handling capability of the HTSC thin film microwave circuits was dealt with. The HTSC microstrip line structures with gilded edges were proposed for improving the power handling capability based on a specified limit of harmonic generation and conductor loss. A general analysis approach was developed by integrating the multi-port network theory into the two proposed nonlinear analysis methods, so that the approach was suitable for any thickness

of gilding layer. The harmonic generation and conductor loss were calculated as a function of the thickness of the gilding layer. It was found that a HTSC microstrip line with gilded edges generated less harmonic power but had higher conductor loss than a pure HTSC microstrip line did. However the loss was still much less than that of a pure gold microstrip line. Thus, the power handling capability was improved.

9.2   Contributions of this thesis

- Developed the MoM-HB combination method for efficient nonlinear analysis for both weak and strong nonlinearities in the frequency-domain by taking the field interaction and fringing field into consideration.

- Developed the power series method for fast nonlinear analysis for weak nonlinearity in the frequency-domain. The field interaction and fringing field are also taken into consideration.

- Analyzed the nonlinear behaviors of HTSC microstrip lines in the frequency-domain.

- Analyzed the nonlinear behaviors of HTSC microstrip patch filters with HTSC interconnecting lines and without HTSC interconnecting lines.

- Proposed gilded HTSC microstrip lines to improve the power handling capability of HTSC microstrip circuits.

- Developed a general analysis method by integrating the multi-port network theory into the two aforementioned proposed methods for analysis of any thickness of gilding layer in a gilded HTSC microstrip line.

9.3 Future research

In this thesis HTSC nonlinearity is modeled by using a power series, which is obtained by curve-fitting to the measured results. We may improve the modeling of HTSC nonlinearity by means of a more complicated and accurate function. Therefore, the methods proposed in this thesis may be improved by including that model for HTSC nonlinearity into them.

The following research topics can be carried on by applying the methods developed in this thesis.

1. Calculation of the mutual coupling between adjacent HTSC microstrip lines determine the crosstalk at high power. An important application for HTSC transmission lines is interconnection for avoiding the dissipative loss in the traditional planar transmission line.

2. Analysis of HTSC two dimensional dual-mode microstrip patch filters with gilded edges for further improvement of power handling capability. The two dimensional dual-mode filter not only handles more power than the one-dimensional filter, but also it saves the substrate space by a factor of almost two compared to the single-mode version because each square represents two modes. The power handling capability can be further improved by using gilded-edged microstrip patch resonators.

3. Analysis of HTSC multi-pole filter circuits. Using HTSC Multi-pole filters can achieve large off-band rejection and very narrow bandwidth without sacrificing in-band insertion loss.

Bibliography

[1] Z.Y. Shen, High-Temperature Superconducting Microwave Circuits, Boston: Artech House, 1994, pp. 9-99

[2] J.M. Madden, Superconductors for integrated circuits, Applied Microwave, 1993, pp59-62, 66-68

[3] C. Wilker, Z.Y. Shen, P. Pang, D.W. Face, 5GHz High Temperature Superconductor Resonators with High Q and Low Power Dependence up to 90K, *IEEE Trans., MTT*, Vol. 39, No. 9, Sept. 1991, pp. 1462-1466

[4] J.A. Curtis, S.J. Fiedziuszko, Dual Mode Microstrip Filters, *Applied Microwave*, Fall 1991, pp. 86-93

[5] R.R. Mansour, Design of superconductive multiplexers using single-mode and dual-mode filters, *IEEE Trans., MTT*, Vol. 42, No. 7, July. 1994, pp.1411-1418

[6] J. Denis, R. Robert, Opportunities for Superconductivity in Future Space Exploration Programs: A Hydrogen Economy for the 21st Century, *Applied Superconductivity*, Vol. 1, Nos 7-9, 1993, pp. 1231-1249

[7] Naval Research Laboratory, The High Temperature Superconductivity Space Experiment (HTSSE), *Applied Superconductivity*, Vol. 1, Nos 7-9, 1993, pp. 1313-1331

[8] R.M. Gagliardi, Satellite Communications, New York: Van Nostrand Reinhold, 1991, pp. 90-153

[9] T.P.Sheahen, Introduction to high temperature superconductivity, 1994, pp. 243-373

[10] K.K. Mei, G.C. Liang, Electromagnetics of Superconductors, *IEEE trans., MTT*, vol. 39, No. 9, Sept. 1991, pp. 1545-1552

[11] J.H. Haywood, Analysis of Nonlinear Microwave Circuits Using Frequency Domain Harmonic Balance Technique, MASc Thesis, University of Waterloo, 1988

[12] T.V. Duzer, C.W. Turner, Principles of Superconductive Devices and Circuits, Elsevier North Holland, Inc, New York, 1981, pp. 92-138

[13] T.K. Sarkar, D.D. Weiner, Scattering Analysis of Nonlinearity Loaded Antennas, *IEEE Trans., AP* Vol. 24, No. 2, March 1976, pp. 125-131

[14] D.E. Oates, A.C. Anderson, D.M. Sheen, and A.M. Ali, Stripline Resonator Measurements of Z_s Versus H_{rf} in $YBa_2Cu_3O_{7-x}$ Thin Films, *IEEE Trans., MTT*, vol. 39, 1991, pp.1522-1529

[15] D.E. Oates, P.P. Nguyen, G. Dresselhaus, M.S. Dresselhaus, C.W. Lam, S.M. Ali, Measurements and Modeling of Linear and Nonlinear Effects in Striplines, *Journal of Superconductivity*, Vol. 5, No.4, 1992, pp. 361-369

[16] J.H. Oates, R.T. Shin, D.E. Oates, M.J. Tsuk, P.P. Nguyer, A Nonlinear Transmission Line Model for Superconducting Stripline Resonators, *IEEE Trans., Applied Superconductivity*, Vol. 3, No. 1, March 1993, pp. 17-22

[17] D.E. Oates, A.C. Anderson, P.M. Mankiewich, Measurement of the Surface Resistance of $YBa_2Cu_3O_{7-x}$ Thin Films Using Stripline Resonators, *Journal of Superconductivity*, Vol. 3, No. 3, 1990, pp. 251-259

[18] C. Wilker, Z.Y. Shen, P. Pang, W.L. Holstein, D.W. Face, Nonlinear Effects in High Temperature Superconductors: 3rd Order Intercept form Harmonic Generation, *IEEE, Trans., Appl. Superc.*, Vol. 5, No. 2, June 1995, pp. 1665-1670

[19] S.A. Maas, Nonlinear microwave circuits, Artech House, Inc, 1988

[20] T.K. Liu, F.M. Tesche, Analysis of Antennas and Scatters with Nonlinear Loads, *IEEE Trans., AP* Vol. 24, No. 2, March 1976, pp. 131-139

[21] O. Vendik, I. Vendik, and T. Samoilova, Nonlinearity of superconducting transmission line and microstrip resonator, *IEEE Trans., MTT*, vol. 45, 1997, pp.173-178

[22] C.W. Lam, D.M. Sheen, S.M. Ali, and D.E. Oates, Modeling the nonlinearity of Superconducting Strip Tramsmission Lines *IEEE Trans. on Applied Superconductivity*, vol. 2, No. 2, june, 1992, pp.58-66

[23] A. Mohamed and S. El-Ghazaly, Nonlinear analysis of microwave superconductor devices using full-wave electromagnetic model, *IEEE Trans., MTT*, vol. 43, No. 11, Nov. 1995, pp.2590-2599

[24] Y.L. Chow, J.J. Yang, D.J. Fang, G.E. Howard, A Closed Form Spatial Green's Function for the Thick Microstrip Substrate, *IEEE Trans., MTT*, Vol. 39, March 1991, pp. 588-592

[25] Y.L. Chow, A. Torabian-Esfahani, N. Hojjat, Simulated Images for Multilayer Media, Complex Images without Prony's Method, *IEEE-APS* International Symposium, California, 1995, pp. 818-821

[26] R.E. Harrington, Field computation by moment method, IEEE Press, 1968, pp. 62-81

[27] R.E. Collin, Foundations for Microwave Engineering, Second edition, McGraw-Hill, Inc., 1992, pp. 55

[28] A.W. Glisson and D.R. Wilton, Simple and Efficient Numerical Methods for Problems of Electromagnetic Radiation and Scattering from Surfaces, *IEEE Trans. on MTT*, Vol. 28, 1980, pp.593-603

[29] D.G. Fang, J.J. Yang, and Y.L. Delisle, Discrete Image Theory for Horizontal Electric Dipoles in a Multilayered Medium, *IEE Proceedings*, Vol. 135, Pt. H, 1988, pp.297-303

[30] A.A. Omar, An Accurate Solution of 3-D Coplanar Waveguide Circuits, Ph.D Thesis, University of Waterloo, 1993

[31] R. Faraji-Dana, Unified Green's Function Technique for the Analysis of Packaged MICs with Applications to Optical Rib Waveguide and Superconducitng Devices, Ph.D Thesis, University of Waterloo, 1993

[32] R.M. Shubair, Efficient Analysis of Vertical and Horizontal Electric Dipoles in Multilayered Dielectric Media, Ph.D Thesis, University of Waterloo, 1993

[33] Y.L. Chow, An Approximation Dynamic Spatial Green's Function in Three Dimensions for Finite Length Microstrip Lines, *IEEE Trans., MTT*, Vol. 28, 1980, pp.393-397

[34] G.H. Howard, J.J. Yang, Y.L. Chow, A Multipipe Model of General Strip Transmission Lines for Rapid Convergence of Integral Equation Singularities, *IEEE Trans., MTT*, Vol. 40, No. 4. April 1992, pp. 628-636

[35] S. Safavi-Naeini, R. Faraji-Dana, Y.L. Chow, Studies of Edge Current Densities in Regular and Superconducting Microstrip Lines of Finite Thickness, *IEE Proc. H*, Oct 1993, Vol. 140, No. 5, pp. 361-366

[36] R. Raraji-Dana, Y.L. Chow, AC Resistance of Two Coupled Strip Conductors, *IEE Proc.-Microw. Antenna Propag.*, Vol. 138, No. 1, Feb. 1991, pp. 37-45

[37] R. Faraji-Dana, Y.L. Chow, Edge Condition of the Field and AC Resistance of a Rectangular Strip Conductor, *IEE Proc.-Microw. Antenna Propag.*, Vol. 137, No. 2, April 1990, pp. 133-140

[38] S. Safavi-Naeini, H.Z. Tang, and Y.L. Chow, A fast nonlinear method for the harmonic effects analysis of a HTS stripline structure, *IEEE AP Society International Symposium*, 1997, pp.332-336

[39] H.Z. Tang, S. Safavi-Naeini, and Y.L. Chow, Study of effects of HTSC nonlinearity on current distribution over a microstrip line, *IEEE AP Society International Symposium*, 1998, pp.1376-1379

[40] H.Z. Tang, S. Safavi-Naeini, and Y.L. Chow, Investigation of Nonlinearity of a HTSC Microstrip Line at High Power *IEEE CCECE*, 1998, pp.894-897

[41] D.M. Sheen, S.M. Ali, D.E. Oates, R.S. Withers, J.A. Kong, Current distribution, resistance and inductance for superconducting strip transmission lines, *IEEE Trans., AS-1*, 1991, (2), pp.108-115

[42] Y.L. Chow and H.Z. Tang, A method for analyzing harmonics from distributed current on superconducting circuits due to high power nonlinearity, *2nd Canadian Applied Superconductivity Workshop*, 1996

[43] Pierre Hartemann, Effective and Intrisic Surface Impedances of High-T_c Superconducting Thin Films, *IEEE Trans., Applied Superconductivity*, Vol 2, No. 4, Dec. 1992

[44] R. Faraji-Dana, Y.L. Chow, The Current Distribution and AC Resistance of a Microstrip Structure, *IEEE Trans., MTT*, Vol. 38, No. 9, Sept. 1990, pp.1268-1277

[45] H.Z. Tang, S. Safavi-Naeini, and Y.L. Chow, Nonlinear Effects of HTSC Microstrip Corner-Cut Patch Filter with and without HTSC Feed Line, *IEEE AP Society International Symposium*, 1999, pp.210-213

[46] R.R. Mansour, B. Jolley, S. Ye, F.S. Thomson, and V. Dokas, On the Power Handling Capability of High Temperature Superconductive Filters, *IEEE Trans., MTT*, Vol. 44, No. 7, July. 1996, pp.1322-1338

[47] R. Faraji-Dana, Y.L. Chow, S. Safavi-Naeini, Power Handling Capability of a HTS Stripline Structure Using an Efficient Interior-Exterior Green's Function Method, *IEE Proc.-Microw. Antenna Propag.*, Vol. 142, No. 6, December 1995, pp. 472-476

[48] Z.Y. Shen, C. Wilker, Raising the Power Handling Capacity of HTS Circuits, *Microwaves & RF*, April 1994, pp. 129-138

[49] G.C. Liang, D. Zhang, C.F. Shih, High power HTS microstrip filters for wireless communication, *IEEE trans., MTT*, vol. 43, No. 12, Dec. 1991, pp. 3020-3028

[50] S. Ye, and R.R. Mansour, A Novel Split-Resonator High Power HTSC Planar Filter, *IEEE MTT-S Digest*, 1997, pp.299-302

[51] Z.Y. Shen et al, High Power HTS Planar Filters with Novel Back-side Coupling, *IEEE Trans., MTT*, vol. 44, June 1997, pp.984-986

[52] H.Z. Tang, S. Safavi-Naeini, and Y.L. Chow, Power Handling Capability of a HTSC microstrip line structure with gilded edges, *IEEE ANTEM*, 1998, pp.467-470

Appendix A

Curve fitting by using least square scheme

Problem definition

Given a group of data

$$x(i), y(i), \qquad i = 1, \cdots, N \tag{A.1}$$

to fit the data into a function:

$$y = a_0 + a_2 x^2 \tag{A.2}$$

The problem is to find a_0 and a_2 to make or satisfy

$$error = \sum_{i=1}^{N} [y_i - y(i)]^2 = min \tag{A.3}$$

where

$$y_i = a_0 + a_2 [x(i)]^2 \tag{A.4}$$

Least square scheme

Putting the data in (A.1) into (A.2) results in n equations. Then the resulted equations are expressed in a form of matrix equation as follows:

$$A \begin{bmatrix} a_0 \\ a_2 \end{bmatrix} = b \tag{A.5}$$

where

$$A = \begin{bmatrix} 1 & [x(1)]^2 \\ 1 & [x(2)]^2 \\ \vdots & \vdots \\ 1 & [x(N)]^2 \end{bmatrix} \tag{A.6}$$

$$b = \begin{bmatrix} y(1) \\ y(2) \\ \vdots \\ y(N) \end{bmatrix} \tag{A.7}$$

Then

$$\begin{bmatrix} a_0 \\ a_2 \end{bmatrix} = (A^T A)^{-1} A^T b \tag{A.8}$$

Appendix B

Validity of the approximation of Ψ integral

The validity of the approximation in (3.34) can be easily shown by considering a single term in the exponential sum of (3.33):

$$\Psi(m, n) = \frac{1}{\Delta l_m \Delta l_n} \int_s \int_{s'} g_m(r) g_n(r') \left[a_i \frac{e^{-jkR_i}}{4\pi R_i} \right] ds' ds \qquad \text{(B.1)}$$

Multiplying the exponential term inside the square brackets by $e^{-jkR_{i,eff}}$ yields

$$\Psi(m, n) = \frac{a_i}{\Delta l_m \Delta l_n} \frac{e^{-jkR_{i,eff}}}{4\pi} \int_s \int_{s'} g_m(r) g_n(r') \left[\frac{e^{-jk(R_i - R_{i,eff})}}{R_i} \right] ds' ds \qquad \text{(B.2)}$$

Under the assumption $|k(R_i - R_{i,eff})| \ll 1$, the exponential term can be expanded in terms of a Maclurian series, that is,

$$e^{-jk(R_i - R_{i,eff})} \approx 1 - jk(R_i - R_{i,eff}) = (1 + jkR_{i,eff}) - jkR_i \qquad \text{(B.3)}$$

Then

$$\Psi(m,n) = a_i \frac{e^{-jkR_{i,eff}}}{4\pi} \left[\frac{1 + jkR_{i,eff}}{\Delta l_m \Delta l_n} \int_s \int_{s'} \frac{g_m(r)g_n(r')}{R_i} ds'ds - jk \int_s \int_{s'} \frac{g_m(r)g_n(r')}{\Delta l_m \Delta l_n} ds'ds \right]$$

(B.4)

By substituting the effective distance $R_{i,eff}$ defined in (3.35), i.e.,

$$\frac{1}{R_{i,eff}} = \frac{1}{\Delta l_m \Delta l_n} \int_s \int_{s'} g_m(r)g_n(r') \frac{1}{R_i} ds'ds$$

(B.5)

into (B.4) and noting that the second integral is equal to unity, we obtain

$$\Psi(m,n) = a_i \frac{e^{-jkR_{i,eff}}}{4\pi} \left(\frac{1 + jkR_{i,eff}}{R_{i,eff}} - jk \right)$$

(B.6)

Therefore, Ψ becomes

$$\Psi(m,n) = a_i \frac{e^{-jkR_{i,eff}}}{4\pi R_{i,eff}}$$

(B.7)